UNIVERSITY OF CALIFORNIA,
IRVINE

Microfluidic Tissue Processing Platform for Single Cell Analysis and Therapeutic Applications

DISSERTATION

submitted in partial satisfaction of the requirements
for the degree of

DOCTOR OF PHILOSOPHY

in Biomedical Engineering

by

Jeremy Andrew Lombardo

Dissertation Committee:
Associate Professor Jered B. Haun, Chair
Professor Abraham Lee
Professor Alan D. Widgerow

2020

DEDICATION

To my friends and family

TABLE OF CONTENTS

LIST OF FIGURES

LIST OF TABLES

ACKNOWLEDGEMENTS

I would like to express the deepest appreciation to my advisor and committee chair, Dr. Jered B. Haun, for his continual guidance and mentorship. Thank you for your enthusiasm, encouragement, and patience through these last four years.

I would like to thank my committee, Dr. Abraham Lee and Dr. Alan D. Widgerow, for their expertise and insights on my projects.

I would also like to thank my lab mates, past and present, who helped make these last four years so memorable. A special thanks to: Xiaolong Qiu and Maka Pennell for introducing me to the world of microfluidic tissue processing and for instilling in me the virtues of tangential filtration, and Vanessa Herrera, Maha Rahim, and Hinesh Patel for countless Monopoly Deal games, lab happy hours, and their constant support. I would also like to thank my undergraduate students: Danny Duong, Anita Ng, Jessica Ting, Dalia Hammouri, Will Juan, and Hung Hoang, for their constant willingness to help, even with the less glamourous parts of science.

Finally, I would like to thank the Royal Society of Chemistry for permission to include Chapter 2, which was originally published in *Lab on a Chip*.

VITA

Jeremy Andrew Lombardo

Education

2020	Ph.D. in Biomedical Engineering, University of California, Irvine
2019	M.S. in Biomedical Engineering, University of California, Irvine
2016	B.S. in Bioengineering, University of Missouri

ABSTRACT OF THE DISSERTATION

Microfluidic Tissue Processing Platform for Single Cell Analysis and Therapeutic Applications

by

Jeremy Andrew Lombardo

Doctor of Philosophy in Biomedical Engineering

University of California, Irvine, 2020

Associate Professor Jered B. Haun, Chair

Tissues are highly complex ecosystems, composed of heterogenous cell populations that vary in gene expression and function due to epigenetic and genetic distinctions, stochastic events, and microenvironmental factors. In the context of cancer, characterizing intratumor heterogeneity has been crucial in understanding cancer progression, metastasis, and the development of drug resistance. In order to capture this significant heterogeneity, high-throughput single cell analysis methods like flow cytometry, mass cytometry, and single cell RNA sequencing must be employed. However, these analysis methods require that tissues first be dissociated into cellular suspensions, which currently represents a major bottleneck hindering these efforts. Conventional protocols for dissociating tissues are inefficient and antiquated, relying on many manual intensive, time-consuming and highly user-variable steps for digesting, disaggregating, and filtering tissue specimens. In areas of regenerative medicine, the reliance on proteolytic enzymes to liberate stem/progenitor cell populations from tissue results in a cellular therapeutic that no longer meets the Food and Drug Administration's guidelines for minimal manipulation. These therapeutics thus face increased regulatory barriers hindering their application in clinical settings. However, advances in microfabricated technologies hold exciting potential in their ability to execute

many standard laboratory procedures, including tissue dissociation, on-chip by offering high-throughput and precise sample manipulation. The goal of this work is to develop and integrate a suite of microfluidic device technologies to dissociate tissues at the point of care. First, we present a simple and inexpensive microfluidic device that simultaneously filters large tissue fragments and dissociates smaller aggregates into single cells, thereby improving single cell yield and purity. Next, we integrate this microfluidic filter device with upstream tissue digestion and aggregate dissociation technologies. The resulting microfluidic platform significantly improves the breakdown of diverse minced tissue specimens, including tumor samples, into high quality cell suspensions that are ready for downstream single cell analysis. We then optimize a microfluidic digestion protocol for primary immune cell isolation from spleen specimens, exploring both enzymatic and nonenzymatic methods. Lastly, we adapt our microfluidic tissue processing technologies to standardize and improve mechanical processing of human lipoaspirate for autologous therapeutics. In future work, we envision incorporating cell sorting and analysis capabilities on-chip to achieve point-of-care single cell diagnostic or therapeutic platforms.

CHAPTER 1: Introduction

1.1 Cellular Heterogeneity and Single Cell Analysis

Cellular heterogeneity refers to the cell-to-cell variation present within all populations of cells. Cell populations may vary in gene expression and function due to either genetic or epigenetic distinctions, the stochastic nature of gene expression, and microenvironmental factors. In complex, heterogenous biological systems, average measurements of bulk populations can mask key differences between subpopulations that may have otherwise explained biological mechanisms. This becomes especially evident when rare cell populations are present.[1] In cancer, solid tumors can exhibit high degrees of intratumor heterogeneity, which has been implicated in cancer progression, metastasis, and the development of drug resistance.[2,3] Recent cell atlasing efforts, like the Human Cell Atlas Initiative, have also begun cataloguing cellular heterogeneity in tissues and organs in order to assemble comprehensive cell reference maps. These maps then serve as a basis for further research and for guiding disease diagnosis and treatment.[4–6] As a result, over the past several years, tissues are increasingly being analyzed at the single cell level.

Cell-based analysis platforms such as flow cytometry, mass cytometry, and single cell sequencing are ideally positioned to assess cellular heterogeneity.[1,7–9] Flow cytometry and mass cytometry both characterize cells in a high throughput manner using protein-specific antibodies and dyes for up to ~50 parameters per cell, based on known surface or intracellular markers present on cell types of interest.[10–12] Next generation sequencing and recent advances in single cell omics technologies have enabled the study of the genome, transcriptome, epigenome, and proteome at the level of individual cells. Single cell RNA sequencing (scRNA-seq) provides a particularly powerful method for unbiased grouping of

cell types and subpopulations, without prior knowledge of marker proteins or genes of interest, and has led to discoveries of new cell types, cellular states, and cell-type specific markers.[13,14] These technologies, however, all require single cell suspensions to analyze, and are thus hindered by the difficulty of dissociating tissues to the single cell level.

1.2. Tissue Dissociation for Single Cell Analysis

In order to assess cellular heterogeneity and conduct analyses at the single cell level, tissues often must first be dissociated into a single cell suspension. The dissociation of tissues into single cells currently represents a major barrier hindering broad application of cell-based analytic approaches. Tissues can vary greatly in terms of strength of cell adhesion, extracellular matrix composition, and cellularity. Diseased tissues can also have altered dissociation kinetics compared to their healthy counterparts.[7] As such, different tissues and disease states often require optimized dissociation protocols for their specific tissue type/state.[15]

Current dissociation methods often involve scalpel mincing, enzymatic digestion with proteolytic enzymes such as collagenase or trypsin, and mechanical agitation. Overall, these methods tend to be time-consuming and labor intensive, as they require many manual processing steps, each with their own unique drawbacks. Scalpel mincing is prone to inter-operator variability, which can affect single cell yields and suspension quality. Lengthy enzymatic digestions can lead to cleavage of surface markers of interest and may also adversely impact cell viability.[16] These enzymatic digestions are often carried out at 37°C, the optimal temperature for many commonly used proteolytic enzymes, which can activate heat shock pathways in cells, altering their transcriptomic profiles.[17] Mechanical agitation methods, such as shaking or trituration, are often ineffective at dissociating cellular

aggregates into single cells, so cell strainers are often needed to remove residual aggregates before moving on with single cell analyses. The aggregates retained on these cell strainers may represent unique, more difficult to dissociate cell populations that are ultimately left out of downstream analysis. As such, inefficient dissociation could lead to biased populations of cells, favoring those that are easiest to dissociate, and may not faithfully represent the original cellular heterogeneity present in the intact tissue.

Currently, there are few commercially available tissue dissociation platforms. The GentleMACs system by Miltenyi is one frequently referenced in literature. It consists of a disposable conical that is filled with minced tissue and enzymatic solution, heated, and blended using a rotating screw to generate shear forces to break apart tissue. Incell Prep by IncellDx is a system that uses rotating blades to mechanically break apart small pieces of tissue without the use of enzymes. However, both systems are costly (~$1000-$5000), only allow for semi-automated tissue dissociation in poorly defined shear environments, and still require an additional cell straining step before downstream single cell analyses. As a result, there remains a critical need for technologies that can further standardize and automate the complete dissociation of tissues into single cell suspensions.

1.3. Adipose Tissue in Regenerative Medicine

Interest in adipose tissue as a potent, easily accessible source of regenerative cells has rapidly increased since Zuk *et al*. first characterized adipose derived stem cells (ADSCs) in 2001.[18] Recently, attention has shifted from ADSCs to the stromal vascular fraction (SVF), a heterogeneous mixture of cells from which ADSCs are derived, due to their often comparable regenerative capabilities and the lack of need for enzymatic digestion or time-consuming cell culture. The SVF, composed of a mixture including mesenchymal stem cells,

endothelial progenitor cells, macrophages, pericytes and preadipocytes, has been shown to improve wound healing in burns,[19] aberrant scar formation, and wounds complicated by ischemia such as in diabetes.[20,21] It has also demonstrated therapeutic potential in models of radiation, multiple sclerosis, Crohn's disease.[22,23] These regenerative properties are often attributed to their secretion of multiple cytokines and growth factors that are critical in wound healing,[24,25] improved vascularization,[26] as well as cell differentiation and extracellular matrix production.[23]

Methods for processing adipose tissue to release the SVF are numerous and varied. Mechanical digestion methods are increasingly desired for clinical application, as enzymatic digestion does not meet the Food and Drug Administration (FDA) guidelines for "minimal manipulation," and thus enzymatically digested adipose tissue is classified as a drug.[27] This classification becomes prohibitive for physicians, as they would be required to submit an Investigational New Drug application to the FDA and have an approved Institutional Review Board in order to use enzymatically isolated SVF cells.[28] As such, mechanical methods to liberate the SVF from lipoaspirate for regenerative therapeutics without the use of enzymes are exceedingly needed.

A common method of nonenzymatic lipoaspirate processing techniques include intersyringe shuffling, which involves manually passing lipoaspirate back and forth between syringes connected by a luer-to-luer connector. An extreme form of intersyringe shuffling, known as nanofat grafting, utilizes high flow rates while processing, and has been shown to be effective in correcting superficial rhytides, scars, discoloration, and improving fat graft survival.[29,30] Although the mechanism behind this benefit currently remains unknown, we have previously shown that nanofat contains increased fractions of stem and progenitor cell

populations compared to unprocessed lipoaspirate.[31] Thus, this benefit may derive from an increased regenerative capacity provided by higher proportions of these cells. When applied as a therapeutic, nanofat is typically injected intradermally through a small-bore needle, so an additional manual filtering step is also required in order to prevent clogging of the injection needle. The multiple, manual processing steps involved in intersyringe shuffling methods are inherently variable, lacking consistent flowrates and shear forces for tissue dissociation, which results in poor standardization and repeatability.

1.4. Microfluidic Technologies

Microfluidic technologies provide many advantages in their ability to carry out numerous standard laboratory procedures in a lab-on-a-chip (LOC) device and in an automated fashion. Microfluidic devices nearly always operate in the regime of laminar flow, which confers highly consist and predictable fluid dynamics. They also allow for precise metering of small fluid volumes, which helps minimize reagent costs, and can be easily integrated with other microfluidic processes.[32] The small footprint and portability of many LOC devices also make them attractive for operation at the point-of-care.

While microfluidic devices have been used extensively in cell sorting and purification,[33] there have been limited efforts to develop platforms for tissue dissociation applications. To date, other groups have developed microfluidic devices to facilitate on-chip digestion[34] and cellular disaggregation using either sharp edges or post arrays.[35,36] Hattersley *et al.* developed an on-chip digestion device, but it produces low cell yields even with prolonged digestions and was only shown effective in digesting softer liver tissues.[34] The Biogrid[35] and μ-Cell Dissociation Chip[36] are two microfluidic devices that were developed to mechanically dissociate neurospheres. The Biogrid device mechanically cuts

neurospheres by repeatedly passing them through an array of micron-scale silicon knife edges. While this device was effective at dissociating neurospheres into smaller aggregates, this dissociation did not reach the single cell level, and this device also requires costly microfabrication. The μ-Cell Dissociation Chip similarly used a micro-pillar array for neurosphere dissociation, but was focused on generating single cells. This device, however, suffered from serious clogging issues. In addition, all of the previously described devices have only successfully demonstrated dissociation with very specific tissue or cell aggregate types, raising questions about wider applicability and utility. Previously, our group developed microfluidic devices for rapid digestion of cm length x mm diameter strips of tissue [37] and for dissociating cellular aggregates into single cell suspensions.[38,39] While these devices have improved processing speed and single cell yields while reducing the reliance on proteolytic enzymes, significant challenges remain. The tissue chamber dimensions of the digestion device limits utility to core needle biopsies, and this device also requires manual sample loading prior to device assembly. As a result, device operation remains labor intensive. Tissue disaggregation also remains incomplete, as small aggregates invariably remain after device processing that require enhanced dissociation power to further reduce to single cells.

1.5. Structure of Dissertation

The remainder of this dissertation is structured as follows: In Chapter 2, we present a simple and inexpensive microfluidic device that simultaneously filters large tissue fragments and dissociates smaller aggregates into single cells, thereby improving single cell yield and purity. In Chapter 3, we incorporate this microfluidic filter device with upstream tissue digestion and aggregate dissociation technologies into a microfluidic platform that

significantly improves the breakdown of diverse minced tissue specimens into high quality cell suspensions, ready for downstream single cell analysis. Chapter 4 explores optimizing a microfluidic digestion protocol for primary immune cells from spleen specimens, examining both enzymatic and nonenzymatic methods. In Chapter 5, we adapt our microfluidic tissue processing technologies to standardize and improve mechanical processing of human lipoaspirate for autologous therapeutics. Chapter 6 concludes this dissertation, summarizing the work described in previous chapters and discusses future directions.

CHAPTER 2: Microfluidic Filter Device for Dissociating Digested Tissues and Cellular Aggregates into Single Cells

2.1 Introduction

Complex tissues are increasingly being analyzed at the single cell level in an effort to catalogue diversity and identify rare driver cells. This would provide a comprehensive cell census that could be used to better understand tissue or organ biology, as promoted by the Human Cell Atlas initiative,[4,6,14] as well as improve the diagnosis and treatment of major diseases including solid tumors.[5,40–45] Cell-based diagnostic methods such as flow cytometry, mass cytometry, and single cell RNA sequencing are ideally positioned to meet the above goals,[1,7–9] but a major limitation is the need to first break tissue down into a suspension of single cells.[7] Traditionally, tissue has been dissociated by mincing into small pieces with a scalpel, digesting with proteolytic enzymes, mechanically dissociating with a pipettor and/or vortexing, and filtering with a cell strainer to remove remaining aggregates. Microfluidic technologies have recently been developed to automate and improve tissue dissociation, including on-chip digestion[34,37] and disaggregation using sharp surface edges, post arrays, and branching channel networks that generate hydrodynamic fluid jets.[35,36,38,39] While these devices have improved processing speed and single cell yield, small aggregates invariably remain after processing. Eliminating these aggregates by enhancing dissociation power or providing an on-chip separation mechanism would improve the quality of single cell suspensions and enable immediate downstream analysis.

Large tissue fragments and cell aggregates are commonly removed from digested tissue samples using cell strainers that contain nylon mesh filters with pore sizes ranging from 35–80 μm. These pores are large enough to allow small aggregates and clusters to pass

through along with the single cells. While cell strainers with smaller pore sizes are available, they are typically not used due to concerns over the loss of single cells. Placing the filter membranes within a microfluidic device should alleviate this issue by minimizing hold-up volume and improving wash efficiency. Moreover, a microfluidic filter device that could be operated at high flow rate (>10 mL/min) could be directly integrated with previously developed hydrodynamic tissue digestion and aggregate dissociation technologies.[37–39] Vacuum-driven filtration systems containing track-etched membranes,[46–48] and microfluidic devices containing microfabricated membranes,[49–53] have been described. These works primarily focused on size-based separation of single cells, typically larger circulating tumor cells (CTCs) from smaller blood cells. Pore sizes ranged from 5-10 μm to capture CTCs, and flow rates ranged from mL/hr for whole blood to 10 mL/min for diluted blood. In addition to size, cell deformability was shown to affect filtration, as cells could extrude through smaller pores depending on their viscosity and the flow rate.[47] Regarding cell aggregates, a novel microfabricated pillar array was designed to capture intact CTC clusters,[54] which have been correlated with higher metastatic potential and worse prognosis relative to individual CTCs.[55,56] The CTC Cluster-Chip successfully trapped >90% of cancer cell line aggregates containing 5 or more cells when operated at 2.5 mL/h, but performance eroded quickly as aggregate size decreased and flow rate increased. This was superior to a track-etched membrane with 5 μm pores, presumably because cell clusters were able to squeeze through the pores. To date, the fate of single cells or cell clusters that pass through microporous membranes has not been investigated. Moreover, nylon membranes similar to those used in cell strainers have not been evaluated within a microfluidic device. These nylon membranes are commercially available as single layer woven meshes with excellent pore density and

uniformity down to 5 μm diameter.

In this work, we integrate nylon mesh membranes with pore sizes ranging from 5 to 50 μm into laser micro-machined, laminated plastic devices and investigate the filtration of tissue fragments, cell aggregates, and single cells. Devices are designed to operate under a traditional direct filtration mode, with sample passing through the membrane, or a tangential filtration mode that utilizes a cross-flow to prevent membrane clogging (Fig. 2.1). Using cancer cell lines, we first show that nylon membranes with 10 μm pores or smaller remove all aggregates containing four or more cells, even when operated at high flow rates (mL min^{-1}). However, some clusters of 2 to 3 cells still pass through pores that are as small as 5 μm. Interestingly, we observe that single cell numbers increase significantly after passing through pore sizes that are smaller than the cells, by as much as five-fold, but this is also correlated with cell damage. We also show that dissociation is only weakly dependent on flow rate through the membrane, but is significantly diminished by the presence of a cross-flow under tangential filtration mode. We then enhance single cell recovery and purity by coupling two filter devices in series, such that aggregates are progressively dissociated into smaller sizes. Results predominantly correlate with the pore size of the second membrane, which is smaller and invariably used in direct filtration mode. Next, we optimize performance using minced and digested murine kidney tissue samples, and demonstrate that the combination of 50 and 15 μm pore size membranes produces the most single cells. Finally, we integrate the 50 and 15 μm pore size membranes into a single microfluidic device and validate results using murine kidney, liver, and mammary tumor tissue samples. After mincing and digesting with collagenase, the dual membrane filter device increases single cell yield by at least 3-fold, and in some cases by more than 10-fold, while also maintaining cell

viability and reducing aggregates. Most strikingly, using the device after a brief 15 min digestion produces as many single cells as a 60 min digestion. Reducing processing time in this manner would help preserve cell viability, phenotype, and molecular signatures for subsequent molecular analysis. Our simple and inexpensive microfluidic filter device significantly improves the recovery of single cells from tissue, and we envision future integration with upstream tissue processing technologies, such as our hydro-mincing and branching channel array, to maximize dissociation speed and efficiency.

2.2 Results and Discussion

2.2.1 Device Design

We designed our microfluidic filter device to remove tissue fragments and cell aggregates produced by standard enzymatic digestion procedures or comparable microfluidic processing.[37] This would enhance single cell purity for downstream diagnostic applications, and any aggregates that were retained could be further processed to increase overall cell recovery. A schematic of the device is shown in Fig. 2.1A. Sample is introduced via the inlet and comes into contact with a microporous membrane. Sample that passes through the membrane will exit through the effluent outlet. A portion of the sample can also be directed along the surface of the membrane and exit through the cross-flow outlet. This arrangement was chosen to maximize device utility by enabling operation in either direct and tangential filtration modes. Under direct filtration, all sample would pass through the membrane to maximize sample recovery and processing speed. Under tangential flow, the cross-flow would sweep larger tissue fragments and cell aggregates away from the membrane surface to prevent clogging. However, not all of the sample would be filtered, requiring multiple passes to collect the full sample.

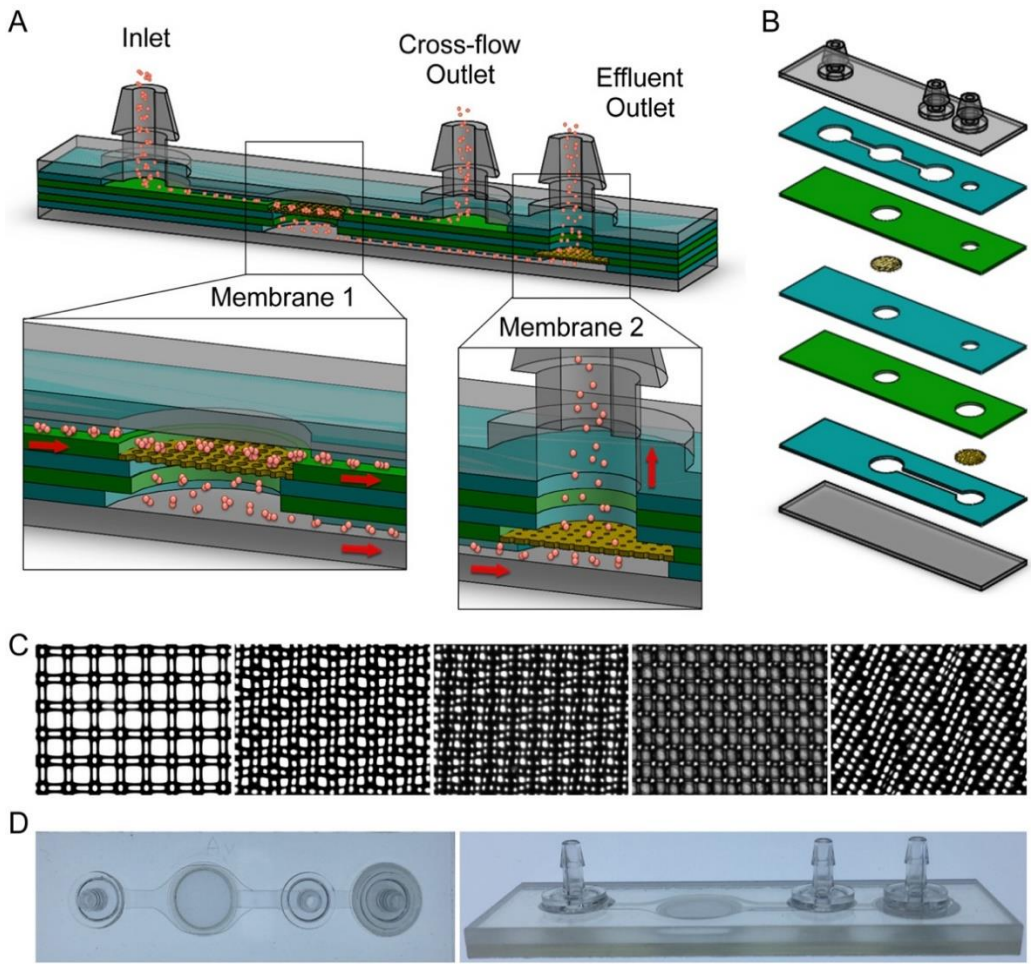

Figure 2.1: Microfluidic filter device for tissue specimens. (A) Schematic of the microfluidic filter device containing two microporous membranes. The first membrane is located in the center of the device, and is intended to restrict large tissue fragments and aggregates from passing through to the Effluent Outlet (Direct Filtration). If desired, some of the sample can be passed over the surface of the first membrane for collection from the Cross-flow Outlet (Tangential Filtration). The second membrane is immediately upstream of the Effluent Outlet, and is intended to restrict smaller aggregates from reaching the Effluent Outlet. (B) Exploded view showing seven PET layers, including three channel layers, two via layers, and two layers to seal the top and bottom of the device (C) Micrographs of nylon mesh membranes, showing lattice network with high pore density and uniformity. Pore sizes are (left to right) 50, 25, 15, 10, and 5 μm diameter. (D) Top and side view of fabricated microfluidic filter device containing two nylon mesh membranes.

Filter devices were fabricated using a commercial laminate approach, with channel features laser micro-machined into hard plastic (polyethylene terephthalate, PET). This provides a more robust end-product than alternative fabrication methods, such as photolithography and casting of polydimethyl siloxane (PDMS), and thus better supports the high flow rates and pressures that are desired for rapid tissue filtration. A total of seven PET layers were used, including two channel layers, three via layers, and two layers to seal the

device (Fig. 2.1B). Fluidic channels, vias, and openings for membranes and hose barb were etched into PET layers using a CO_2 laser. Nylon mesh membranes were purchased in 5, 10, 15, 25, and 50 μm pore sizes as large sheets and were cut to size using a CO_2 laser. Device layers, nylon mesh membranes, and hose barbs were then assembled, bonded using adhesive, and pressure laminated to form a single monolithic device. We included two locations for mounting thin, microporous membranes. The first location was in the center of the device, sandwiched between the middle channel and top via layers, and this membrane would be used for either tangential or direct filtration of large tissue fragments and cellular aggregates. We hypothesized that a second membrane with smaller pores could help maximize single cell purity. This membrane was placed immediately upstream of the effluent outlet, sandwiched between the bottom channel and second via layers, and would allow for direct filtration of smaller aggregates and clusters. Hose barbs were mounted in the top layer to serve as device inlets and outlets. After laser micro-machining, devices were assembled by stacking the various layers and membranes together, which were then firmly bonded using adhesive and pressure lamination. Channel height was ~300 μm, which included contributions from the plastic (250 μm) and adhesive (~50 μm).

For the microporous membranes, we chose to utilize single-layer, woven nylon meshes similar to those used in cell strainers. These are commercially available with pore sizes down to 5 μm from numerous vendors as inexpensive, ready-to-use sheets that can be cut to size. The nylon threads create a lattice network with high pore density and uniformity, which should limit back-pressure and allow for high flow rates through the membrane. Micrographs of the nylon mesh membranes used in this study are shown in Fig. 2.1C, and properties are listed in Table 2.1. Moreover, we hypothesized that the narrow cross-section

and rounded shape of the nylon threads will be ideal for dissociating aggregates into smaller

Table 2.1: Nylon mesh membrane properties

Pore diameter (μm)	Thread diameter (μm)	Porosity (%)
5	50	1
10	28	2
15	45	5
25	42	14
50	40	31

clusters or even single cells. This is similar in principle to the sharp silicon edges of the Biogrid device,[35] but now operating on a large scale and, importantly, avoiding costly microfabrication. We would expect a dissociation mechanism to be most prevalent when aggregates are only slightly larger than the pores. Aggregates that span many pores are more likely to be captured in a manner similar to traditional filtration. Track-etched membranes were considered, as they are also cheap, easy to use, and have been used extensively in single cell and aggregate filtration studies.[46–48,54] However, the largest pore size available is 30 μm, and the random localization of the pores can cause them to overlap, particularly at high porosity. Microfabricated membranes offer precise control over pore size, shape, and location and have been used for cell filtration and compartmentalization.[49–53,57] However, custom fabrication adds cost and complexity. Finally, pores within both track-etched and microfabricated membranes are defects within the material, making them less durable at high porosity. For nylon mesh membranes, tensile forces will be resisted by the threads and dissipated throughout the material, making them more robust and failure-resistant. Thus, we concluded that nylon mesh membranes provided the optimal combination of cost and

performance characteristics, while also providing potential for aggregate dissociation. A fabricated microfluidic filter device containing two nylon mesh membranes is shown in Fig. 2.1D.

2.2.2 Filtration of Cell Line Aggregates

We first investigated single cell recovery and viability for nylon mesh membranes with 5, 10, 15, 25, or 50 μm pore sizes. To eliminate confounding effects, we fabricated devices containing only the first membrane (see Membrane 1 in Fig. 2.1A). Experiments were performed using MCF-7 human breast cancer cells, which are strongly cohesive and provide large numbers of aggregates from standard tissue culture. We also note that MCF-7 cells are very large at ~20 μm diameter. Cell suspensions were passed through devices using a syringe pump, and initial tests were performed using direct filtration at 12.5 mL/min. Device effluents were recovered and imaged under phase contract microscopy to identify single cells, clusters of 2 to 3 cells, small aggregates of 4 to 10 cells, and large aggregates of >10 cells. Recovery results for each population are plotted in Fig. 2.2A. Large and small aggregates constituted 10% and 15% of the control population, respectively. These percentages decreased after filtration, in concordance with pore size, down to <0.5% for the 5 and 10 μm pores. Single cells were initially present at less than 30%, and progressively rose as pore size decreased, reaching a maximum of 85%. Clusters remained around 40-45% for all but the 5 and 10 μm pore sizes, but even then were still present at a substantial level. We also quantified single cell numbers using a cell counter, and results are plotted in Fig. 2.2B after normalization by the control. For the 50 μm pore size, ~15% of single cells were lost, most likely due to holdup or non-specific adhesion within the device. For all other pore sizes, more single cells were recovered after filtration, suggesting that a percentage of the

aggregate and/or cluster populations were dissociated into single cells. Dissociation became more pronounced as pore size decreased, with single cells increasing by more than 5-fold for the 5 μm pore size. However, extruding cells through smaller pores compromised viability, as determined by flow cytometry using a propidium iodide exclusion assay (Fig. 2.2C). Specifically, losses in viability scaled inversely with single cell recovery. As a result, the number of viable single cells that were recovered remained constant, around 40% higher than the control, for the 5, 10, and 15 μm pore sizes (Fig. 2.3A).

We next examined the effect of flow rate while still utilizing the direct filtration mode. We found that decreasing flow rate as low as 0.25 mL/min resulted in general trends toward lower single cell numbers and higher viability, but these changes were not significant (Fig. 2.2D-E). Aggregate, cluster, and single cell percentages were also similar for each flow rate

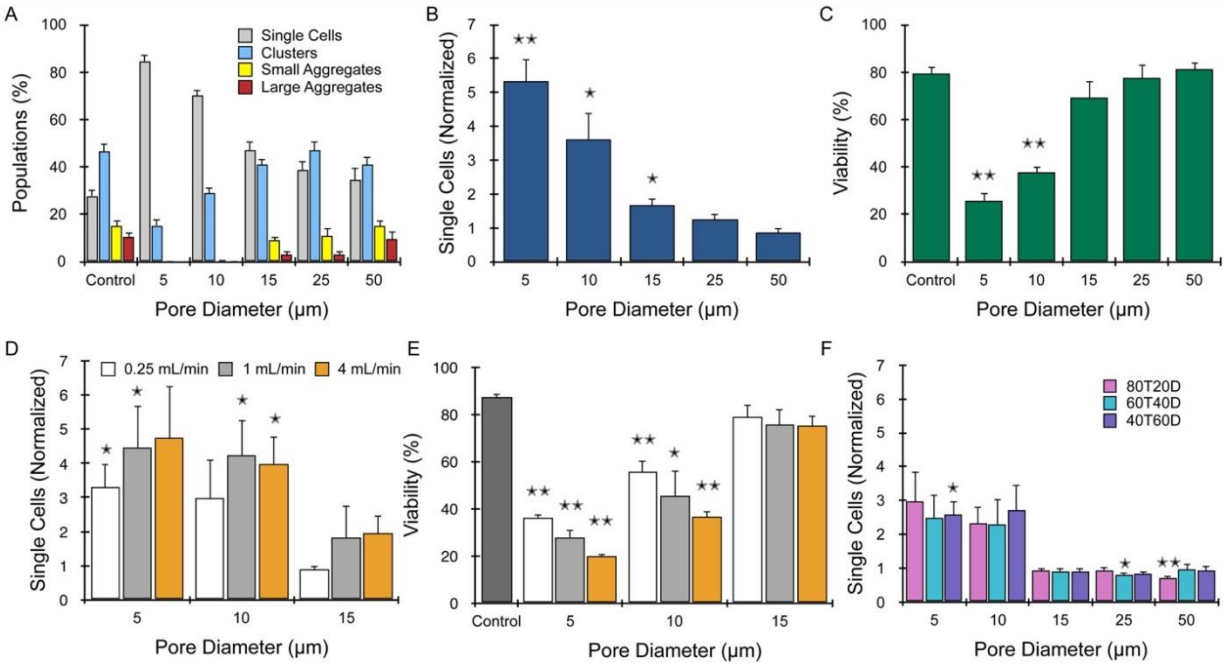

Figure 2.2: Single filter device experiments using MCF-7 cells. (A) Live single cell numbers for experiments performed under direct filtration mode and 12.5 mL/min flow rate. Values were ~40% higher than the control for each of the 5, 10, and 15 μm pore sizes. (B) Cell populations obtained for direct filtration experiments at 0.25, 1, and 4 mL/min flow rates. (C-E) Cell populations obtained for tangential filtration experiments using 12.5 mL/min total flow rate and cross-flow ratios of (C) 80%, (D) 60%, and (E) 40%. Error bars represent standard errors from at least three independent experiments. * indicates $p < 0.05$ and ** indicates $p < 0.01$ relative to the control.

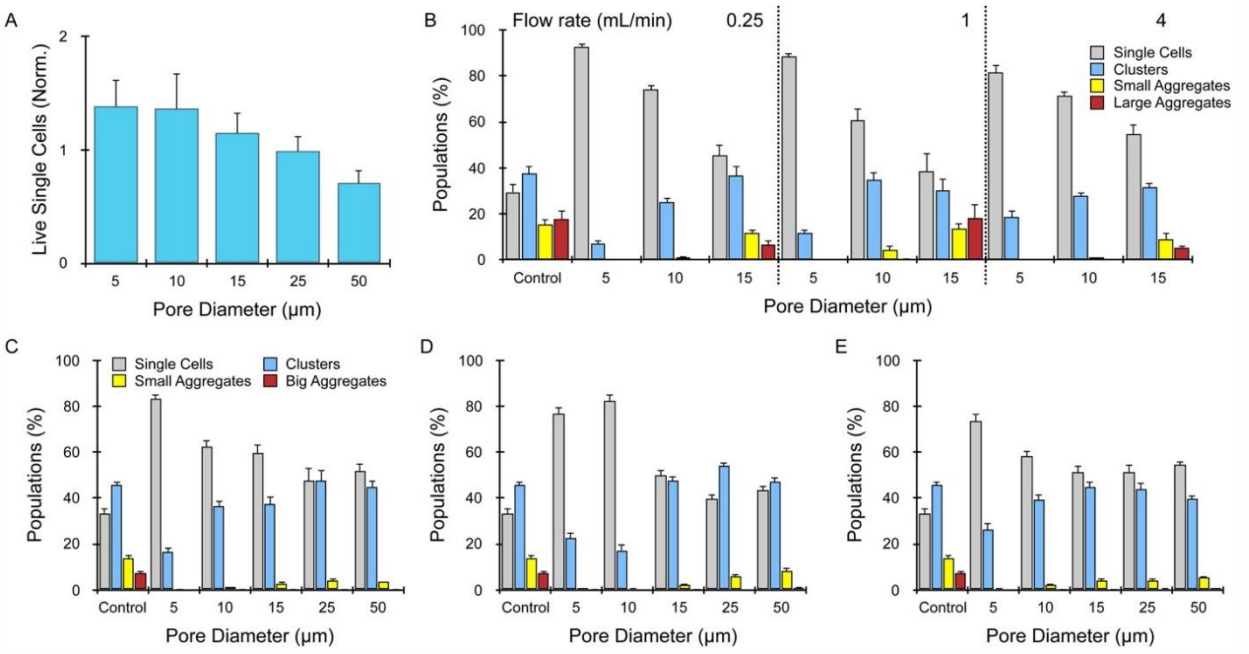

Figure 2.3: Characterization of single membrane filter devices using MCF-7 cells. (A) Single cells, clusters, and aggregates were quantified from micrographs and plotted as percent of total population before (control) and after passing through filter devices containing one membrane with the indicated pore size. Devices were operated in direct filtration mode using a flow rate of 12.5 mL/min. Aggregates and clusters were removed with increasing efficiency as pore size decreased, with single cells starting at less than 30% and reaching a maximum of 85%. (B) Single cell numbers were quantified using a cell counter and normalized by the control. Significantly more single cells were recovered following filtration through the 5, 10, and 15 μm pore sizes, indicating dissociation of aggregates into single cells. (C) Viability was determined by propidium iodide exclusion assay, and decreased with pore size. (D,E) Direct flow experience at lower flow rates, which generally resulted in (D) less single cell number and (E) higher viability, although changes were modest. (F) Tangential filtration experiments using different cross-flow ratios (40 to 80%), which resulted in substantially lower single cell numbers than direct flow experiments at 12.5 mL/min. Error bars represent standard errors from at least three independent experiments. * indicates $p < 0.05$ and ** indicates $p < 0.01$ relative to the control.

(Fig. 2.3B). Finally, we investigated tangential filtration mode by diverting the sample between the cross-flow and effluent outlets using two syringe pumps that were operated in withdrawal mode. The total flow rate was held constant at 12.5 mL/min, similar to direct filtration experiments, while the cross-flow was varied from 40 to 80%. Afterwards, sample collected from the cross-flow outlet was passed through the membrane in direct filtration mode at 12.5 mL/min, and both effluents were combined prior to analysis. We found that single cell numbers were similar at all cross-flow ratios (Fig. 2.2F), which were significantly lower than direct filtration experiments at 12.5 mL/min (compare to Fig. 2.2B). In fact, single

cell numbers under tangential filtration were similar to direct filtration at 0.25 mL/min, even though all tangential experiments were performed utilized higher membrane flow-through rates (>2.5 mL/min). We did find that tangential filtration removed large aggregates more effectively at the 50 μm pore size (Fig. 2.3C-E). Taken together, we conclude that under pressure driven flow, aggregate and cluster dissociation depended primarily on membrane pore size and whether a cross-flow was present, and less so on the flow rate through the membrane.

2.2.3 Improving Aggregate Dissociation using Two Membranes in Series

Based on these results, we postulated that aggregate dissociation could be enhanced by passing samples through two nylon membranes in series. In this scenario, the first membrane would reduce aggregate size such that the second membrane could better liberate single cells. Therefore, we coupled two single-membrane filter devices in series using tubing and performed direct filtration experiments at 12.5 mL/min. Since we were primarily interested in dissociation, we initially tested the smaller pore size membranes in various combinations. We found that passing MCF-7 suspensions through two filter devices eliminated nearly all aggregates (Fig. 2.4A), even for the 15 μm pore size. Clusters were also reduced relative to the single filter experiments (compare to Fig. 2.2A), reaching a low of 9% for the 5-5 membrane combination. Single cell number and viability results are presented in Fig. 2.4B and C, respectively. Single cell yield did not change for the 5-5 and 10-5 membrane combinations relative to the single filter case (compare to Fig. 2.2B), as samples were already well-dissociated. However, the 15-5 membrane combination produced fewer single cells, suggesting that the 15 μm membrane captured aggregates that the 5 μm membrane would have been able to dissociate into single cells. For the 10 μm membrane, single cell numbers

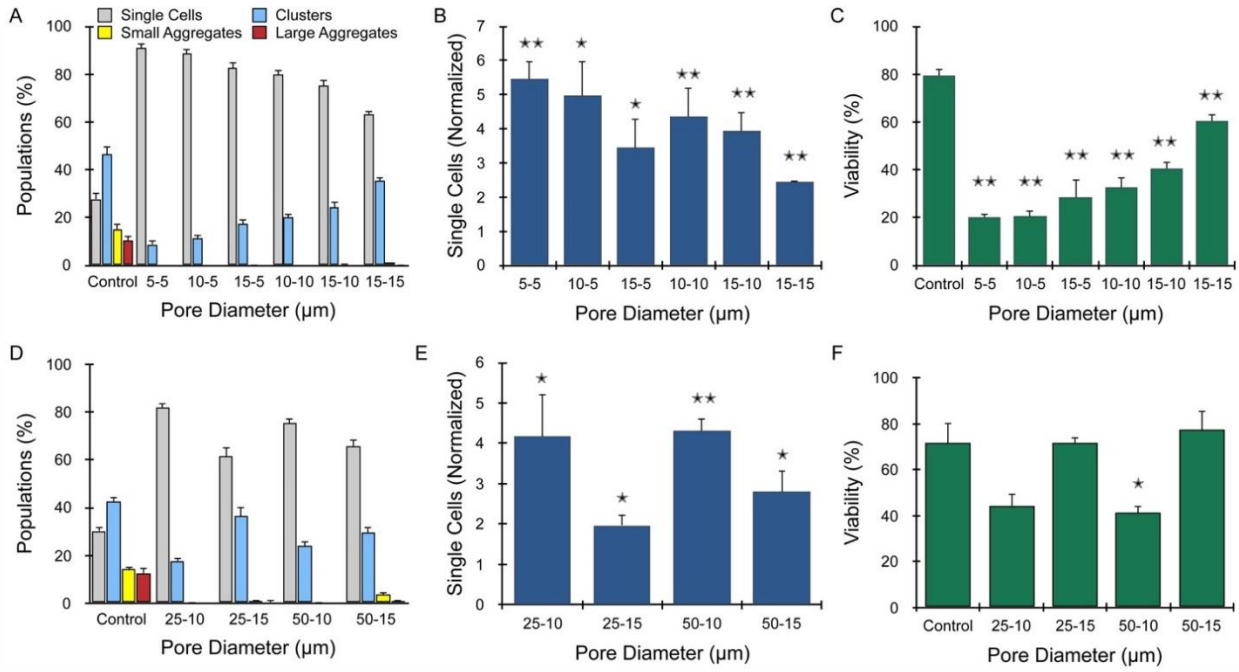

Figure 2.4: Combining two filter devices in series. (A-C) Various combinations of the 5, 10, and 15 μm membrane filter devices were connected by tubing and operated under direct filtration mode at 12.5 mL/min flow rate. (A) Large and small aggregate populations were eliminated from all filter device combinations. (B) Single cell recovery and (C) viability were generally similar to the single filter, direct filtration experiments for the 5 and 10 μm membranes. The 15-15 membrane device combination did have higher single cell numbers than the 15 μm pore membrane alone. (D-F) Tangential filtration experiments using the 25 or 50 μm membranes followed by the 10 or 15 μm membranes with 60% cross-flow and 12.5 mL/min total flow rate. Results for (D) single cell, cluster, and aggregate populations, (E) single cell recovery, and (F) viability were all dictated primarily by the pore size of the second membrane. Error bars represent standard errors from at least three independent experiments. * indicates $p < 0.05$ and ** indicates $p < 0.01$ relative to the control.

were similar between single and double filter device experiments. The only case in which the use of two membranes was beneficial was for the 15-15 membrane combination, which increased single cell numbers increased from 50% to 150% higher than the control. We found that cell viability was predominantly determined by the pore size of the second, smaller membrane, and that values were similar to the single filter device experiments (compare to Fig. 2.2C). While we again observed that viability was generally correlated with single cell numbers, live single cell numbers were lowest for conditions that employed the 5 μm membrane (Fig. 2.5A). Thus, we deemed the 5 μm pores too small, at least for these ~20 μm MCF-7 cells. For the 10-10, 15-10, and 15-15 membrane combinations, live single cell

recovery was ~60% higher than the control. For context, this level of dissociation is comparable to the best version of our branching channel dissociation device for the same MCF-7 cell model.[39]

Next, we investigated using the 10 and 15 μm membranes in combination with the larger 25 and 50 μm membranes. Two filter devices were coupled in series as previously described, but now experiments were performed under tangential filtration. As with single filter device experiments, total flow rate was held constant at 12.5 mL/min and sample collected from the cross-flow outlet was passed through both devices under direct filtration mode. Using 60% cross-flow, we found that single cell, cluster, and aggregate populations were similar to the direct flow experiments utilizing the same 10 and 15 μm membranes (Fig. 2.4D). However, a small number of aggregates were recovered from the 50-15 membrane combination. Single cell recovery and viability results were also generally determined by the second, smaller membrane (Fig. 2.4E and F). As such, single cell numbers for the 10 μm pore size were similar to direct flow experiments using either one or two filter devices. For the 15 μm pore size, single cell numbers were similar to the 15-15 membrane combination under direct filtration, but now viability was significantly higher and equal to the control. It is unclear whether this change was related to using larger pore sizes in the upstream filter device, tangential filtration mode, or a combination of both. In total, live single cell numbers were ~2-fold greater than the control for all but the 25-15 combination Fig. 2.5B). We note that nearly identical results were obtained for tangential filtration experiments performed using 80% cross-flow (Fig. 2.5C-F). Based on the combined results obtained with the MCF-7 cell aggregate model, we conclude that the second membrane predominantly dictated single cell recovery and viability because of its smaller pore size and consistent utilization of the

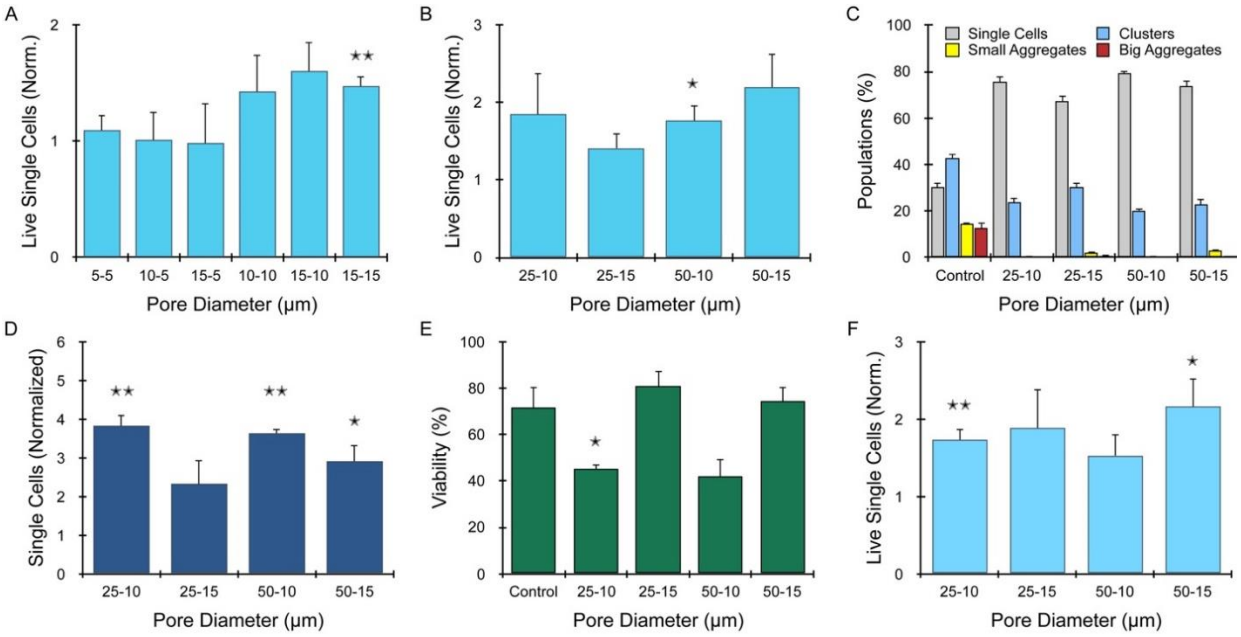

Figure 2.5: Double filter device experiments using MCF-7 cells. (A) Live single cell number for double filter device experiments performed under direct filtration mode and 12.5 mL/min flow rate. Values were lowest for membrane all combinations that included the 5 μm pore size. (B) Live single cell numbers for double filter device experiments performed under tangential filtration mode, 12.5 mL/min total flow rate, and 60% cross-flow ratio. Values were close to 2-fold greater than control in all cases. (C-F) Double filter device experiments performed under tangential filtration mode, 12.5 mL/min total flow rate, and 80% cross-flow ratio. Results for (C) cell populations, (D) single cell recovery, (E) viability, and (F) live single cell recovery were similar to 60% cross-flow ratio experiments. Error bars represent standard errors from at least three independent experiments. * indicates $p < 0.05$ and ** indicates $p < 0.01$ relative to the control.

direct filtration mode. Placing a second membrane upstream could improve results in some cases, particularly for the 15 μm membrane, but the pore size and operational mode of the first membrane was less important.

2.2.4 Optimization using Murine Kidney Tissue

Since our ultimate goal is to use the filter devices with complex tissues, we next evaluated performance using murine kidney tissue samples. We continued to use two filter devices in series, specifically the larger 25 or 50 μm pore sizes followed by smaller 10 or 15 μm pore sizes. The first filtration was performed under direct or tangential (60% cross-flow) mode, and a total flow rate of 12.5 mL/min. Fresh kidneys were harvested, sliced into histologically similar sections with a scalpel, minced into ~1 mm^3 pieces, and weighed.

Samples were then digested with collagenase and mechanically treated by vortexing and pipetting, per routine protocol. We initially evaluated device performance using tissue samples that were only briefly digested with collagenase, as this would prove the most stringent test of membrane clogging and dissociation power. After digestion for 15 min, device treatment increased single cell numbers by at least 2-fold for all membrane combinations and filtration modes (Fig. 2.6A). Maximal results were ~4-fold higher than

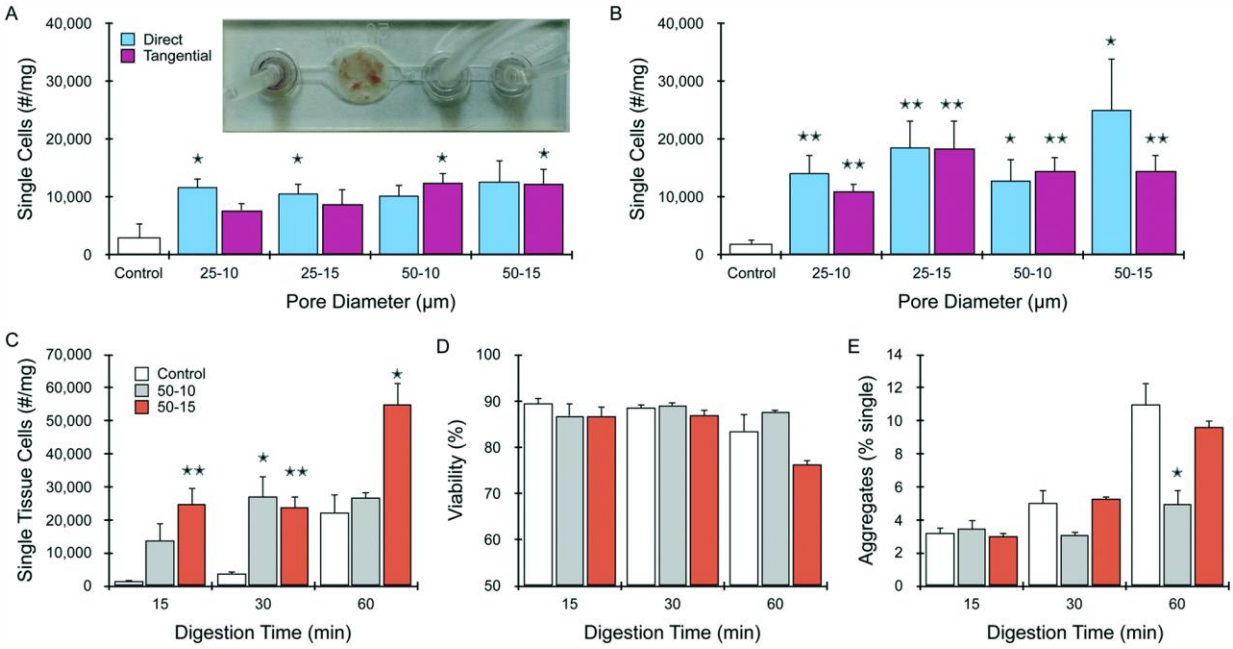

Figure 2.6: Optimization of membranes and operational mode using murine kidney tissue. Freshly harvested kidney tissue was minced and digested with collagenase before passing through the two filter devices that were coupled in series. (A and B) Evaluation of the 25 or 50 μm membranes combined with the 10 or 15 μm membranes, performed under direct or tangential (60% cross-flow) filtration modes. Single cell count was determined using a cell counter. (A) After 15 min digestion, device treatment increased single cell recovery by 2- to 4-fold for all membrane combinations and filtration modes. Inset shows tissue captured on a 50 μm pore size membrane. (B) Device treatment increased single cell recovery by more than 5-fold for all cases after 30 min digestion. Results were generally based on the second membrane pore size, and did not vary significantly with the first membrane pore size or filtration mode. (C–E) Investigation of the 50–10 and 50–15 combinations using flow cytometry. (C) Single tissue cells numbers recovered from the 50–15 and 50–10 membrane combination exceeded controls by 5- to 10-fold at the 15 and 30 min digestion times. After 60 min digestion, the 50–15 μm combination enhanced single tissue cell recovery by 2.5-fold. (D) Viability was ~90% for all conditions at the 15 and 30 min digestion times, but decreased after 60 min digestion to ~80% for the control and 75% for the 50–15 μm filter combination. (E) Aggregate and cluster numbers were quantified using scattering information and are presented relative to single cells. Aggregates increased with digestion time for controls, remained the same using the 50–15 membrane combination, but decreased for the 50–10 membrane combination. Error bars represent standard errors from at least three independent experiments. * indicates $p < 0.05$ and ** indicates $p < 0.01$ relative to the control at the same digestion time.

control, which were obtained for both 25 μm pore size combinations under direct filtration and both 50 μm pore size combinations under tangential filtration. Increasing digestion time to 30 min enhanced single cell recovery for all device conditions, which were now at least 5-fold higher than the control (Fig. 2.6B). Results were generally greater for the 15 μm pore combinations regardless of the first membrane size or operational mode, which was consistent with our findings with the MCF-7 aggregate model. For both 15 and 30 min digestion times, we observed that large pieces of tissue were trapped by the first membrane (Fig. 2.6A), but membrane fouling was not an issue for either direct or tangential filtration modes, most likely because we were using relatively small tissue samples (<100 mg).

Based on these preliminary results, we chose to further evaluate cell suspensions using flow cytometry. Specifically, we used a panel of stains to assess cell viability and identify red blood cells and leukocytes, as previously described. We also chose to only use the 50 μm pore size in the first device due to higher porosity and the direct filtration mode since it was faster and easier to execute. The number of single tissue cells recovered per mg tissue is shown in Fig. 2.6C. Results at the 15 and 30 min digestion times were similar to the cell counter data in Figs. 2.6A and B, with both 50-10 and 50-15 membrane combinations producing 5- to 10-fold more single cells than the control. Digesting for 60 min resulted in a dramatic increase in single tissue cell numbers to ~20,000/mg. The 50-10 membrane combination was similar to the control, but the 50-15 membrane combination enhanced recovery by 2.5-fold. Notably, the 50-15 membrane combination also produced similar numbers of single tissue cells after digesting for 15 min as the control after digesting for 60 min. Cell viability was ~90% for all conditions at the 15 and 30 min digestion time points (Fig. 2.6D). However, 60 min digestion decreased viability to ~80% for the control and

~75% for the 50-15 μm filter combination. We also used scattering information to quantify the percentage of aggregates relative to single cells (Fig. 2.6E). We note that samples were passed through a 35 μm cell strainer prior to analysis to prevent clogging of the cytometer, and thus results likely only reflect cell clusters. Aggregate percentage increased progressively with digestion time for controls, from 3 to 11%, indicating that traditional dissociation methods are not effective at reducing tissue all the way down to single cells. Aggregate percentages remained unchanged for the 50-15 membrane combination, but the 50-10 membrane combination reduced aggregates by approximately half at the 30 and 60 min digestion time points. Red blood cell and leukocyte recoveries (Fig. 2.7A-B) closely mirrored the single tissue cell recovery results in Fig. 2.6C.

2.2.5 Filter Device Integration and Validation using Murine Organ and Tumor Tissues

Based on the superior performance of the 50-15 membrane combination in terms of single tissue cells recovered from kidney samples, we fabricated a single device containing both membranes, as shown in Fig. 2.1. The double membrane filter device was first validated using murine kidney samples that were digested for 60 min, and performance in terms of single tissue cell recovery and viability was comparable to the previous results obtained with two single filter devices coupled in series (Fig. 2.7C-D). We then tested freshly resected murine liver samples, which are generally easier to enzymatically digest, but hepatocytes are also well-known to be fragile.[58] After a brief 15 min digestion, approximately 2500 single tissue cells were obtained per mg liver tissue for the control, and this was enhanced 5-fold by filter device treatment (Fig. 2.8A). At 30 min, single tissue cells increased by 2-fold for the control, but device treatment remained static, resulting in a more modest 2-fold improvement. Both control and device conditions were both much higher after 60 min

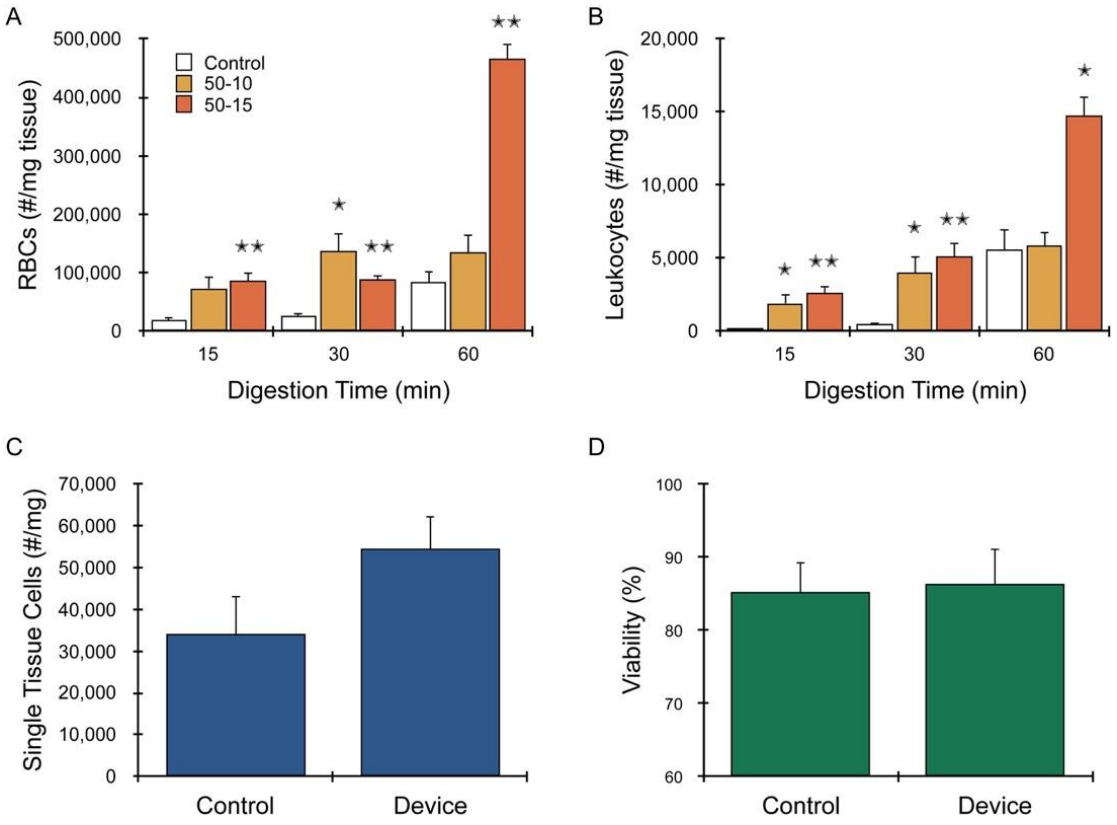

Figure 2.7: Filter device optimization using murine kidney tissue. (A,B) Experiments performed using two single membrane filter devices connected in series. Recoveries are shown for (A) red blood cells and (B) leukocytes, which both increased with both digestion time and device processing in a manner consistent with single tissue cell recovery results in Fig. 2.6C. (C,D) Experiments performed using the integrated dual membrane filter device with kidney tissue that was digested for 60 min. (C) Single tissue cell number increased by ~60% after device processing relative to the control. (D) Viability remained at >85%, similar to control. Error bars represent standard errors from at least three independent experiments. * indicates $p < 0.05$ and ** indicates $p < 0.01$ relative to the control at the same digestion time.

digestion, around 40,000 single tissue cells/mg, indicating that the liver tissue had been fully broken down by enzymatic digestion. Viability remained greater than 90% for all conditions (Fig. 2.8B), which was very encouraging considering the fragile nature of hepatocytes. Aggregates were present at ~1% for controls at all digestion times, and were generally reduced by device treatment although differences were not significant (Fig. 2.8C). As a final evaluation, we used mammary tumors that spontaneously arise in MMTV-PyMT transgenic mice. Tumors are generally considered among the most difficult epithelial tissues to dissociate due to their abnormal extracellular matrix composition.[59] For these tests, we

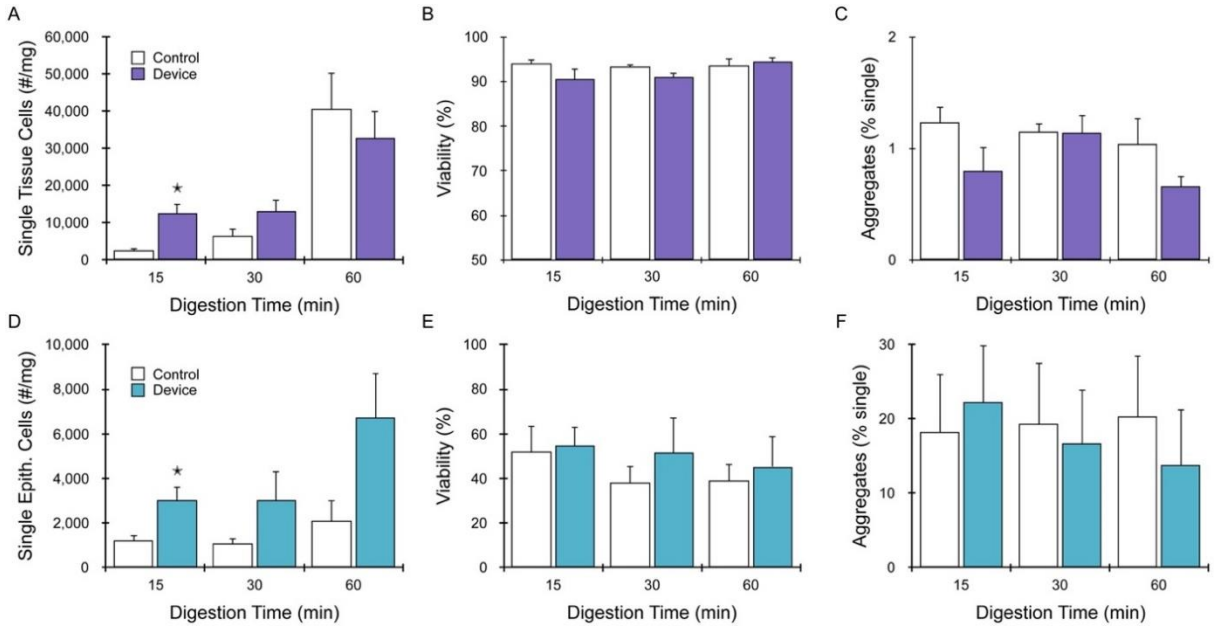

Figure 2.8: Validation of the integrated dual membrane filter device using murine liver and mammary tumor tissue samples. Freshly harvested murine liver and breast tumor tissue was minced and digested with collagenase before passing through the microfluidic filter device containing 50 and 15 μm membranes. (A-C) Liver samples. (A) Device treatment increased single liver tissue cells by 5-fold and 2-fold after 15 and 30 min digestion, respectively. The device did not increase single liver tissue cells further after 60 min, as enzymatic digestion had fully liberated cells. (B) Viability remained greater than 90% for controls and device conditions. (C) Aggregates were present at ~1% for controls at all digestion times, and were generally reduced by device treatment. (D-F) Mammary tumor tissue. (D) Device treatment increased single epithelial cells by 3-fold at all digestion times. (E) Cell viability was significantly lower for tumors at 40-50%, but did not vary significantly with digestion time or device treatment. (F) Aggregates constituted about 15-20% of cell suspensions for all conditions. Error bars represent standard errors from at least three independent experiments. * indicates $p < 0.05$ and ** indicates $p < 0.01$ relative to the control at the same digestion time.

modified the flow cytometry detection panel by adding an antibody specific for the general epithelial marker EpCAM. This enabled us to positively identify epithelial tissue cells, although this would include both normal or cancerous cells. Control conditions produced ~1000 single epithelial cells per mg tumor tissue at both the 15 and 30 min digestion time points, and this only increased to ~2000 cells/mg after 60 min digestion (Fig. 2.8D). Device treatment enhanced single cell recovery by approximately 3-fold at all time points. Epithelial cell viability was only ~40-50% for all conditions (Fig. 2.8E), potentially indicating that the tumor samples contained highly necrotic regions. A significant number of aggregates were present at all conditions, in the range of 15-20% of the total recovered population (Fig. 2.8F). This suggests that more dissociation power will be needed to effectively liberate all cells

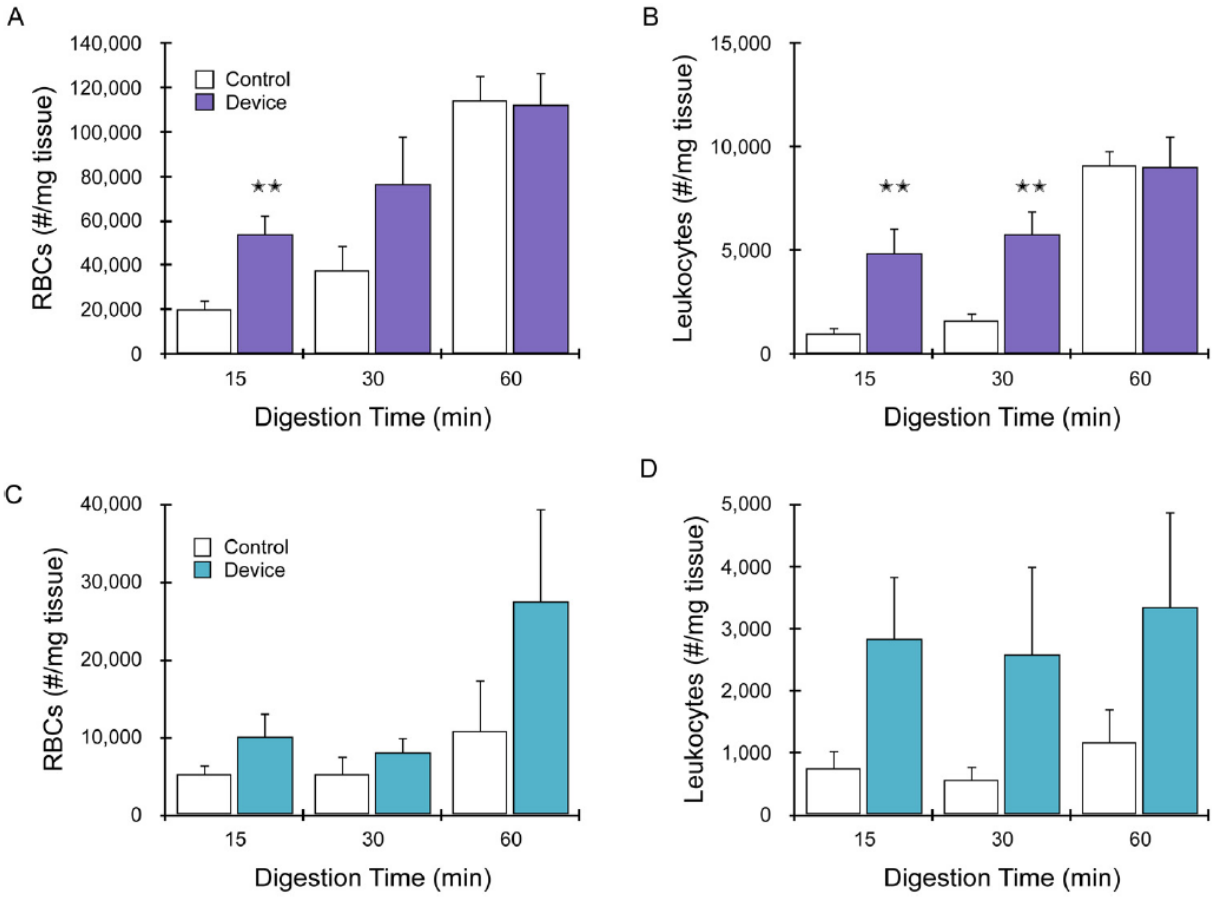

Figure 2.9: Red blood cell and leukocyte recoveries for murine liver and tumor tissue samples. Results are shown for (A,B) liver and (C,D) mammary tumor cell suspensions. Red blood cell and leukocyte cell counts increased with both digestion time and device processing in all cases. Recoveries increased with digestion time and device processing in a manner consistent with single tissue/epithelial cell results in Fig. 5. Error bars represent standard errors from at least three independent experiments. * indicates $p < 0.05$ and ** indicates $p < 0.01$ relative to the control at the same digestion time.

from tumors. For both liver and tumor samples, red blood cell and leukocyte recoveries followed similar trends as the single liver tissue cell and single epithelial cell data (Fig. 2.9A-D).

2.3 Materials and Methods

2.3.1 Device Fabrication

Microfluidic devices were fabricated by ALine, Inc. (Rancho Dominguez, CA). Briefly, fluidic channels, vias, and openings for membranes and hose barb were etched into polyethylene terephthalate (PET) layers using a CO2 laser. Nylon mesh membranes were

purchased from Amazon Small Parts (10, 15, 25, and 50 μm pore sizes; Seattle, WA) or EMD Millipore (5 μm; Burlington, MA) as large sheets and were cut to size using the CO2 laser. Device layers, nylon mesh membranes, and hose barbs were then assembled, bonded using adhesive, and pressure laminated to form a single monolithic device.

2.3.2 Cell Culture Aggregate Model and Murine Tissue Samples

MCF-7 human breast cancer cell line was purchased from ATCC (Manassas, VA). Cells were cultured at 37 °C and 5% CO2 in tissue culture flasks using DMEM media containing 10% FBS, non-essential amino acids, 1 mM sodium pyruvate, 2 mM L-glutamine, 100 μg mL−1 streptomycin, 100 U mL−1 penicillin, and 44 U L−1 Novolin R insulin (Thermo Fisher, Waltham, MA). Prior to experiments, confluent monolayers were briefly digested for 5 min with trypsin-EDTA, which released cells with a substantial number of aggregates. Cell suspensions were then centrifuged and resuspended in PBS containing 1% BSA (PBS+). Kidneys and liver were harvested from freshly sacrificed BALB/c or C57B/6 mice (Jackson Laboratory, Bar Harbor, ME) that were determined to be waste from a research study approved by the University of California, Irvine's Institutional Animal Care and Use Committee (courtesy of Dr. Angela G. Fleischman). Mammary tumors were harvested from freshly sacrificed MMTV-PyMT mice (Jackson Laboratory, Bar Harbor, ME). For kidneys, a scalpel was used to prepare ~1 cm long × ~1 mm diameter strips of tissue, each containing histologically similar portions of the medulla and cortex. Each tissue strip was then further minced with a scalpel to ~1 mm^3 pieces. Liver and mammary tumors were uniformly minced with a scalpel to ~1 mm^3 pieces. Minced tissue samples were then weighed, placed within microcentrifuge tubes along with 300 μL of 0.25% collagenase type I (Stemcell Technologies, Vancouver, BC), digested at 37 °C in a shaking incubator under gentle agitation for 15, 30, or

60 min, and mechanically disaggregated by repeated pipetting and vortexing. Finally, cell suspensions were treated with 100 units of DNase I (Roche, Indianapolis, IN) for 10 min at 37 °C and washed by centrifugation into PBS+.

2.3.3 Dissociation and Filtration Studies

Microfluidic filter devices were prepared by affixing 0.05′′ ID tubing (Saint-Gobain, Malvern, PA) to the device inlet and outlet hose barbs. Prior to experiments, devices were incubated with SuperBlock (PBS) blocking buffer (Thermo Fisher Scientific, Waltham, MA) at room temperature for 15 min to reduce non-specific binding of cells to the membranes and channel walls and washed with PBS+. MCF-7 cells or digested murine tissue samples were loaded into a syringe and passed through the device using a syringe pump (Harvard Apparatus, Holliston, MA) at total flow rates ranging from 0.25 to 12.5 mL min−1. For tangential filtration experiments, two syringe pumps were employed in withdrawal mode, one each connected to the cross-flow and effluent outlets. The withdrawal rates were adjusted to achieve a given cross-flow rate, while total flow rate was always maintained at 12.5 mL min−1. Following the initial pass, sample collected from the cross-flow outlet was passed directly through the membrane at 12.5 mL min−1 and collected from the effluent outlet. Following all experiments, devices were washed with 1 mL PBS+ to flush out any remaining cells, and all effluents were combined into a single sample. Cell counts were obtained using a Moxi Z automated cell counter and type S cassettes (Orflo, Hailey, ID).

2.3.4 Quantifying Cell Aggregates by Microscopy

Single cells and aggregates were assessed by microscopy using methods that we previously described.[39] Briefly, MCF-7 cell suspensions were imaged with a Hoffman phase contrast microscope and a 4× objective. Raw images were then converted to binary using

MATLAB, and ImageJ was used to identify, outline, and calculate the area of all contiguous cellular units. Each unit was then classified based on area as a single cell (20 to 80 pixels^2 or 75 to 300 μm^2), cluster (80 to 200 pixels^2 or 300 to 750 μm^2), small aggregate (200 to 300 pixels^2 or 750 to 1120 μm^2), or large aggregate (>300 pixels^2 or >1120 μm^2). Referencing back to the micrographs, this corresponded to ~2 to 3 cells for clusters, ~4–10 cells for small aggregates, and >10 cells for large aggregates.

2.3.5 Flow Cytometry

We closely followed the flow cytometry protocol that we previously developed for tissue suspensions.16 Briefly, cell suspensions were co-stained with 2.5 μg mL^{-1} anti-mouse CD45-PE monoclonal antibody (clone 30-F11, BioLegend, San Diego, CA) and 0.5X CellMask Green (Thermo Fisher, Waltham, MA) for 20 minutes at 37 °C. Samples were then washed twice using PBS+ by centrifugation, co-stained with 5 μg mL^{-1} 7-AAD (BD Biosciences, San Jose, CA) and 12.5 μM DRAQ5 (BioLegend) on ice for at least 15 minutes, and analyzed on an Accuri C6 flow cytometer (BD Biosciences). Flow cytometry data was compensated and analyzed using FlowJo software (FlowJo, Ashland, OR), and a sequential gating scheme was used to identify live and dead single tissue cells from leukocytes, red blood cells, non-cellular debris, and cellular aggregates.

2.4 Conclusion

In this work, we have presented a simple and inexpensive microfluidic filter device that can rapidly and effectively improve the quality of single cell suspensions obtained from digested tissue samples. This was accomplished using nylon mesh membranes with well-defined, micron-scale pores that simultaneously filtered larger tissue fragments and dissociated smaller aggregates into single cells. Specifically, we demonstrated that using two

nylon mesh membranes, first a larger pore size in the range of 25–50 μm followed by a smaller pore size in the range of 10–15 μm, resulted in dissociation of aggregates into progressively smaller sizes and ultimately enhanced single cell recovery. The dissociation effect was likely due to the combination of hydrodynamic shear forces and physical interaction with the nylon threads. While this was effective, we note that care must be given to prevent cell damage, particularly for complex tissues that may contain cells of different sizes. Using the final dual membrane microfluidic filter device with 50 and 15 μm pore sizes, the number of single cells recovered from minced and digested murine kidney, liver, and tumor tissue samples was enhanced by at least 3-fold, and in some cases by more than 10-fold. We also showed that a brief 15 min digestion and filter device treatment could produce comparable single cell numbers to a full 60 min digestion. Importantly, cell viability was maintained for all tissue types and operating conditions, even fragile liver cells. These results will be important for advancing single cell analysis and atlasing of complex tissues, as dissociation has been a major bottleneck hindering these efforts.[37] Improved mechanical dissociation efficiency would help by reducing manual labor and enzyme cost, ensuring that sufficient sample is recovered even from smaller clinical specimens, and preventing bias in the final suspension towards cells that are easiest to isolate. Alternatively, shorter digestion times would accelerate tissue processing work flows and could potentially better preserve the original phenotypic state from within the tissue. While we used nylon mesh membranes in this study, it is possible that track-etched or microfabricated membranes with the same pore sizes could provide similar results. Our design also included the option to perform the first filtration under tangential mode, although this was not found to be critical for generating single cells. We do note that it is possible that tangential filtration could become

more important if tissue size were scaled up beyond 100 mg. Additionally, cell aggregates could be passed through the filter device continuously to increase single cell recovery, similar to diafiltration.[60] In future work, we will continue to optimize the microfluidic filter device using different tissue types. We will also integrate the filter device with our hydro-mincing digestion device to enable automated processing of cm-scale tissue samples,[37] as well as our branching channel dissociation device to maximize single cell numbers and purity.[38,39] This integrated platform would be capable of processing full tissue samples all the way down to a highly pure suspension of single cells in a rapid and efficient manner. Furthermore, we will seek to integrate downstream technologies to enable on-chip sorting and analysis of single cells to create point-of-care diagnostic platforms for tissue samples.

CHAPTER 3: Microfluidic Tissue Processing Platform for Single Cell Analysis and Primary Cell Isolation.

3.1 Introduction

Tissues are highly complex ecosystems containing a diverse array of cell types. Even within a given cell subtype, significant variation in gene expression patterns can arise based on differences in activation state, genetic mutations, epigenetic distinctions, stochastic events, and microenvironmental factors.[13,61] As such, there is rapidly growing appreciation for the importance of cellular heterogeneity in understanding tissue and organ development, normal function, and disease pathogenesis.[62–68] In the context of cancer, intratumor heterogeneity has been shown to be a key indicator of disease progression, metastasis, and the development of drug resistance.[2,3,69,70] High-throughput single-cell analysis methods such as flow cytometry, mass cytometry, and single cell RNA sequencing (scRNA-seq) are increasingly being employed to capture this cellular heterogeneity,[1,71] and have already begun to transform our understanding of complex tissues by enabling identification of previously unknown cell types and states.[14,67,72,73] However, a critical barrier to these efforts is the need to first process tissues into a suspension of single cells. Current methods involve mincing, digestion, and disaggregation that are labor intensive, time-consuming, inefficient, and highly variable.[7,15] Thus, new tissue dissociation approaches and technologies are critically needed to ensure the reliability and wide-spread adoption of single cell analysis methods. This would be particularly important for translating single cell diagnostics to human tissue specimens in clinical settings. Moreover, improved tissue dissociation would make it faster and easier to extract cells for *ex vivo* drug screening, engineered tissue constructs, and cell-based therapies comprised of stem and/or progenitor populations.[74–77]

A particularly exciting application would be patient-derived organ-on-a-chip devices, which seek to recapitulate complex native tissues for personalized drug testing.[74,78–82]

Single cell RNA-sequencing (scRNA-seq) has recently emerged as a powerful and widely adaptable analysis technique that provides information about the full transcriptome of individual cells. This has enabled large scale cell atlases to generate comprehensive cell reference maps of known, and as yet unknown, cell subtypes and states for normal and diseased tissues.[4,6] For example, a recent atlas of normal murine kidney identified a new collecting duct cell suggestive of a transitional phenotypic state and indicative of a previously unexpected level of cellular plasticity.[63] Moreover, an atlas of primary human breast epithelium linked distinct epithelial cell populations to known breast cancer subtypes, suggesting that these subtypes may develop from different cells of origin.[62] For melanoma specimens, scRNA-seq was used to identify three transcriptionally distinct states, one of which was drug sensitive, and further demonstrated that drug resistance could be delayed using computationally optimized therapy schedules.[83] While scRNA-seq is clearly a powerful diagnostic modality, the need to break down tissues into single cells introduces challenges that can affect data quality and reliability. This includes the lack of protocol standardization, which can lead to substantial variation across different research groups and tissue types. Another significant concern is that incomplete break down could bias results towards cell types that are easier to liberate. A recent study utilizing single nuclei RNA sequencing (snRNA-seq) with murine kidney samples found that endothelial cells and mesangial cells were indeed underrepresented in scRNA-seq data.[84] Finally, lengthy enzymatic digestion times have been shown to alter transcriptomic signatures and generate stress responses that

interfere with cell classification.[17,85–88] Addressing these concerns would help propel the exciting field of scRNA-seq into the future for tissue atlasing and disease diagnostics.

Microfluidic technologies have advanced the fields of biology and medicine by miniaturizing devices to the scale of cellular samples and enabling precise sample manipulation.[89–93] Most of this work has focused on manipulating single cells, including on-chip cell purification, sorting, and analysis.[33,93–96] Only a small number of studies have addressed tissue processing, and even fewer have focused on breaking down tissues into smaller constituents.[34–36] We developed the first microfluidic device that specifically focused on breaking down cellular aggregates into single cells.[38,39] This dissociation device contained a network of branching channels that progressively decreased in size from millimeters down to ~100 μm and contained repeated expansions and constrictions to break down aggregates using shear forces. We then developed a device for on-chip tissue digestion using the combination of shear forces and proteolytic enzymes.[37] Finally, we developed a filter device containing nylon mesh membranes that removed large tissue fragments, while also further dissociating smaller cell aggregates and clusters.[37] These microfluidic digestion, dissociation, and filter devices each improved tissue processing by decreasing digestion time and/or increasing single cell recovery when operated independently. To date, however, we have not combined these technologies to maximize performance and execute a complete tissue processing workflow on-chip. Moreover, we have not yet validated microfluidically-processed cell suspensions using scRNA-seq.

Here, we present a microfluidic platform consisting of 3 different tissue-processing technologies that significantly improves the breakdown of diverse tissue types into single cell suspensions that are ready for downstream single cell analysis. First, we develop a novel

version of our digestion device that can be quickly loaded with minced tissue and operated without user assembly. We show that this minced digestion device efficiently reduces mm-scale pieces of murine kidney into cellular aggregates and even single cells. Next, we further process cell suspensions obtained via microfluidic digestion using downstream dissociation and filter technologies, which have now been integrated into a single unit. We find that the integrated downstream device can further enhance single cell yield for kidney, with the optimal results obtained from a single pass. Using our optimized protocol, we then investigate how different cell types dissociate as a function of processing time for murine kidney, tumor, liver, and heart tissues. For difficult to digest tissues such as kidney and tumor, microfluidic processing can reduce protocols from an hour to 15 min. Alternatively, at longer processing times the device platform produces >2-fold more epithelial cells and leukocytes, and >5-fold more endothelial cells. Total cell yields are similar whether sample is processing is performed for a defined time, or sample is removed at periodic intervals. Using single cell RNA sequencing with kidney and tumor, all expected populations are found in control and device conditions, with certain, more difficult to dissociate cell types like endothelial cells are preferentially liberated later in the digestion. In kidney, we also show that shortened interval operation minimizes cellular stress responses, while in tumor stress responses are more similar across digestion lengths and conditions. For easier to digest tissues such as liver and heart, processing time can be reduced to 5 min, and even as short as 1 minute. Interestingly, recovery of the sample at intervals produces substantially more hepatocytes and cardiomyocytes, most likely because these cell types are sensitive to shear forces. All results are achieved without compromising cell viability or requiring cell straining prior to single cell analyses. The system can significantly shorten processing time or enhance

single cell recovery, and in some cases accomplish both. Furthermore, the entire tissue processing workflow is performed in an automated and reliable fashion. Thus, our microfluidic platform holds exciting potential to advance diverse applications that require the liberation of single cells from tissues. In future work, we envision incorporating cell sorting and analysis capabilities on-chip to achieve fully point-of-care single cell diagnostic platforms.

3.2 Results and Discussion

3.2.1 Device Design and Fabrication

We previously developed a microfluidic digestion device that could be loaded with cm length x mm diameter strips of tissue, which were manually loaded prior to device assembly and fluid priming.[37] This process was labor intensive, and these chamber dimensions would only be ideal for core needle biopsy specimens. For this work, we designed a new digestion device that could be loaded with minced tissue in a single step, followed by immediate operation. Scalpel mincing of tissue into ~1 mm^3 pieces is ubiquitous, and therefore this format should be compatible with a wide array of tissue types and dissociation protocols. The full layout of the minced tissue digestion device is shown in Fig. 3.1A. The design includes three primary components: a luer port for loading minced tissue, a chamber that retains the tissue in place, and fluidic channels that administer both fluid shear forces and proteolytic enzymes. These features are arranged across six layers of hard plastic that include two fluidic layers, two via layers, a top end cap that contains the hose barbs and the tissue loading port, and a bottom end cap. The tissue chamber is in the upper fluidic layer, directly beneath the loading port and a circular via that is 2.5 mm in diameter. This arrangement enables minced tissue to be loaded quickly and easily into the chamber,

and the loading port can then be sealed using a plug or stopcock prior to device operation. A detailed schematic of the tissue chamber is shown in Fig. 3.1B. We employed a square geometry, with both length and width at 5 mm, to facilitate the loading process and evenly distribute tissue. This is in contrast to the high-aspect ratio (1 cm long x 1.5 mm wide) tissue chamber that we employed in previous work.[37] The chamber height is 1.5 mm, slightly larger than minced tissue pieces, in order to prevent clogging during sample loading and device operation. Fluidic channels are placed upstream and downstream of the tissue chamber, and in both cases we employed four channels that are 250 μm wide. The symmetric channel design is another departure from the original device, which included narrower (200 μm) "hydromincing" channels upstream and wider (500 μm) "sieve gate" channels downstream. This change was made because scalpel-minced tissue requires greater emphasis on prevention of device clogging. Specifically, we set the new channel width to be slightly less than the height of the lower channel layer, which is ~300 μm. We also extended channel length to 4 mm to prevent larger tissue pieces from squeezing through to the lower channel layer, but flared them to a larger width prior to connecting to the underlying via layer to make it easier to connect the features during assembly.

The dissociation and filter devices will further process tissue pieces and cell aggregates that are small enough to escape the tissue chamber of the digestion device. This includes disaggregation through the use of hydrodynamic shear forces within a branching channel array and physical interaction with nylon mesh filters.[97] For this work, we have integrated the dissociation and filter devices into a single unit in to minimize device holdup volume and simplify operation. The original designs for both devices were already

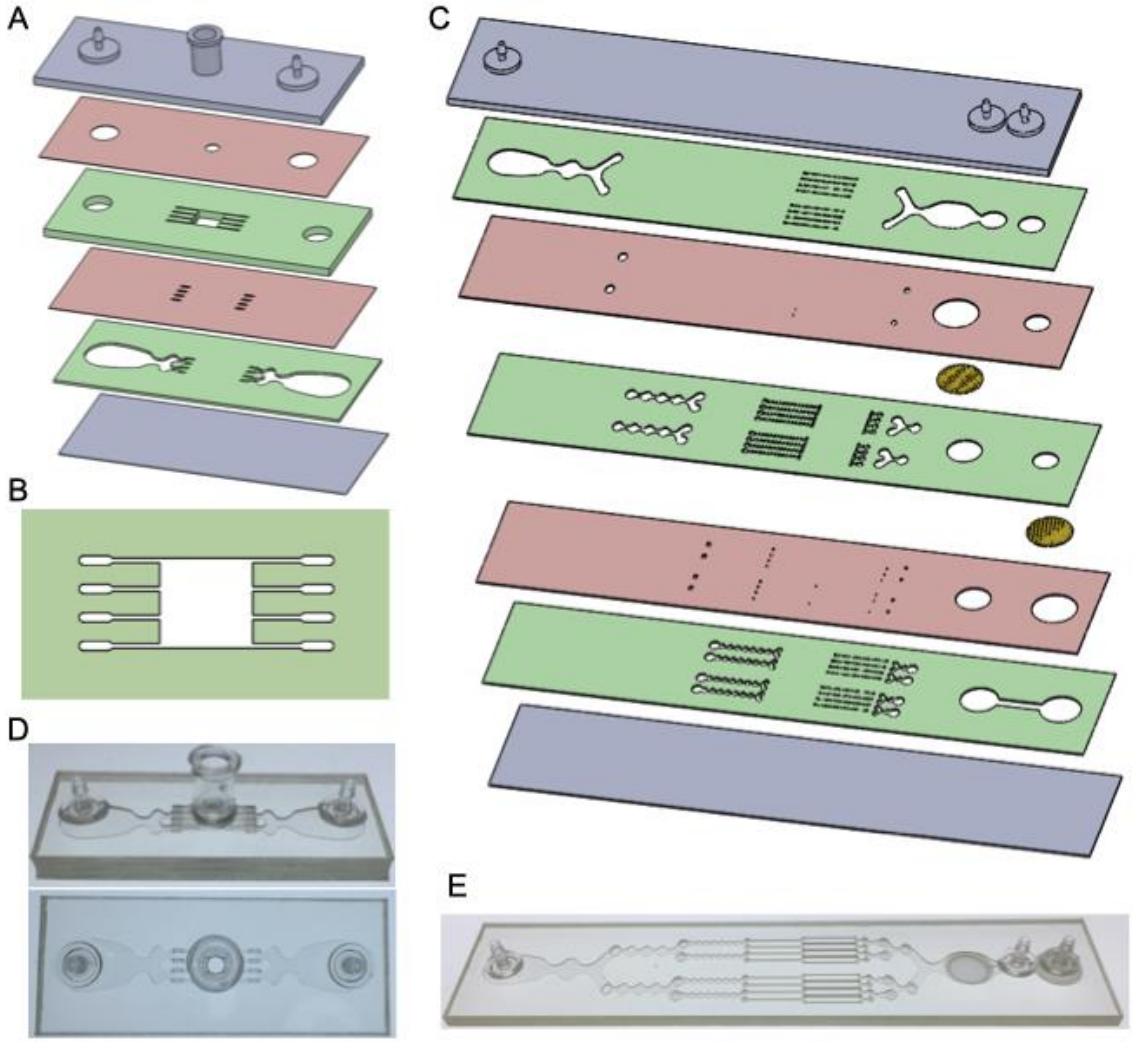

Figure 3.1: Microfluidic devices for tissue processing. A) Schematic of the minced tissue digestion device. Design includes six total layers, including two fluidic layers (green), 2 via layers (red), and top and bottom end caps (grey). Device consists of three primary components: a luer port for loading tissue, a tissue chamber, and fluidic channels. The luer port provides an access point to quickly and easily load minced tissue and can then be closed off using a plug or stopcock prior to device operation. Fluidic channels upstream and downstream of the tissue chamber deliver the circulating enzymatic solution tissue held in the chamber, while also retaining minced tissue pieces in the chamber. (B) Schematic of the integrated dissociation and filtration device. The dissociation and filtration devices are intended to further process tissue pieces and cell aggregates produced by the digestion device using hydrodynamic forces within a branching channel array and nylon mesh filters, respectively. The devices were integrated into a single unit in to minimize device holdup volume and simplify operation. (C) Side and top view of fabricated minced digestion device. (D) Side view of fabricated integrated dissociation and filtration device.

arranged across 7 layers, and thus it was straightforward to combine the layouts using a slightly larger footprint, as shown in (Fig. 3.1C).

The minced digestion and integrated dissociation/filter devices were fabricated using a commercial laminate process, with channel features laser micro-machined into hard plastic (PMMA or PET). This method method results in a robust end product that can withstand the high flow rates that are needed for dissociating tissues. After laser micro-machining, devices were assembled by aligning the various layers and bonding using pressure sensitive adhesive. Photographs of the fabricated devices are shown in Figs. 3.1D and E.

3.2.2 Platform Optimization using Murine Kidney

We first evaluated the new minced digestion device using adult murine kidney samples. The kidney is a complex organ composed of anatomically and functionally distinct structures that play essential roles in maintaining fluid and electrolyte homeostasis. Adult kidney tissue also has a dense matrix that is challenging to dissociate into single cells.[98] For this study, freshly dissected kidneys were minced using a scalpel down to ~1 mm^3 pieces and loaded into the minced digestion device through the luer port. The device was then primed with PBS buffer containing 0.25% type I collagenase, the luer input port was sealed using a stopcock, and a peristaltic pump was used to recirculate the enzymatic solution through the device. We tested flow rates of 10 mL/min from previous work with the dissociation and filter devices[38,97] and 20 mL/min from the original core biopsy digestion device.[37] After recirculating the collagenase fluid for either 15 or 60 min, sample was collected, washed, and genomic DNA (gDNA) was extracted using a QIAamp DNA kit in order to assess total cell recovery. A control was minced and processed directly with the kit, and thus this result represents the upper limit for gDNA. At 10 mL/min flow rate, gDNA recovery was ~15% and 60% of the control after 15 and 60 min, respectively (Fig. 3.2A).

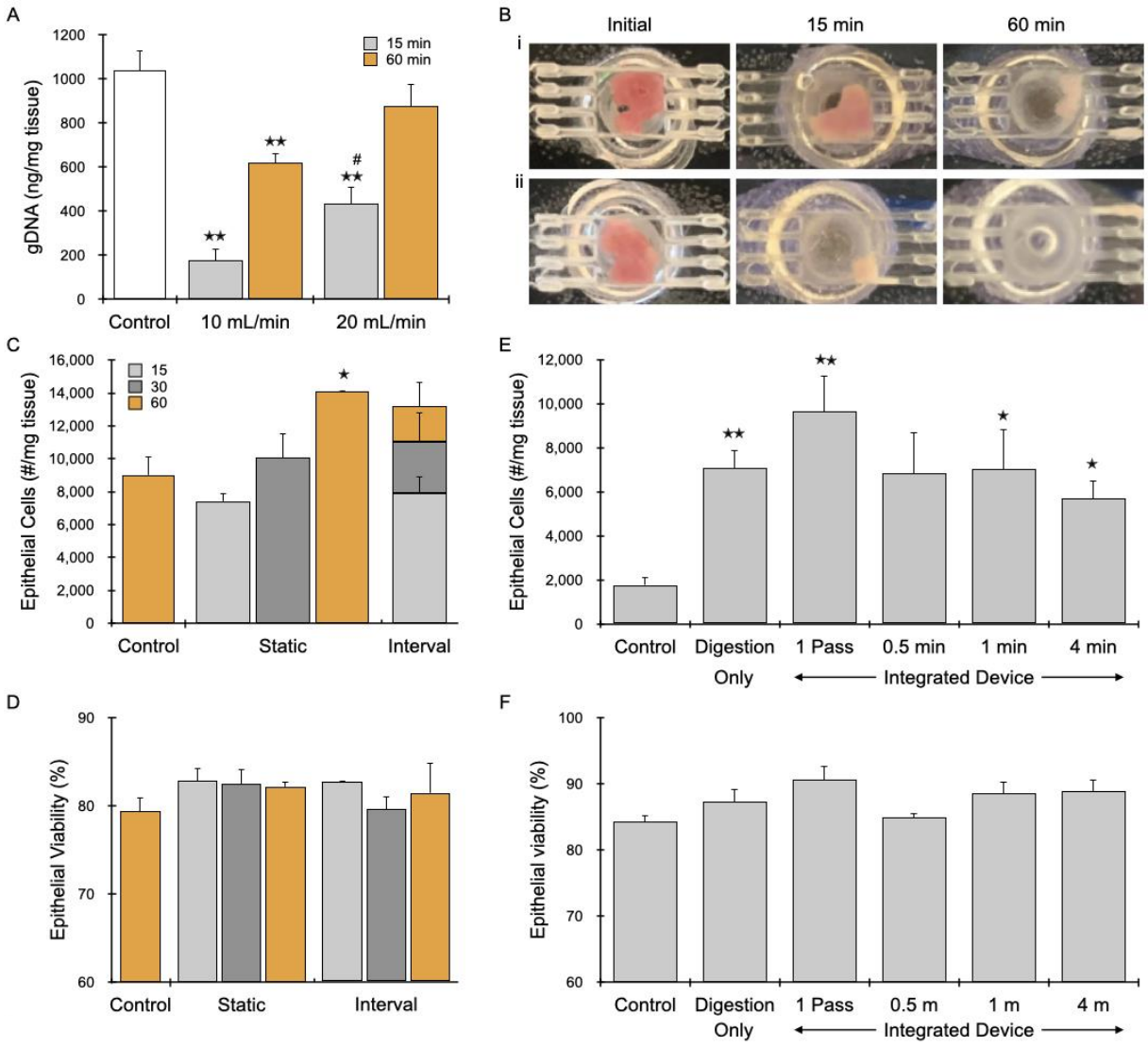

Figure 3.2: Optimization using murine kidney. (A) Genomic DNA (gDNA) quantified from cell suspensions obtained after minced digestion device treatment using 10 or 20 mL/min flow rate for 15 or 60 min of processing. Control represents total possible gDNA recovery. gDNA increased with both processing time and increased flow rate. 20 mL/min flow rate is superior for the digestion device, especially at shorter time points. (B) Pictures of tissue in minced digestion device chamber before and after 15 or 60 min of processing at 10 (i) or 20 (ii) mL/min flow rate. Significant amounts of tissue remain in the chamber after 15 min at 10 mL/min, corroborating observed low gDNA recovery. Less tissue was present after 60 min at 10 mL/min and 15 min at 20 mL/min. Tissue remains exclusively in channels/vias after 60 min at 20 mL/min. 20 mL/min flow rate was used for remainder of study. (C) Interval operation was introduced, where devices was operated for set time periods (15, 30, or 60 min), cell suspensions were eluted, additional collagenase was added, and operation continued. Control sample were digested in collagenase, agitated, and pipetted/vortexed per standard tissue dissociation protocols. Single epithelial cells increased with digestion time for static digestions. Cell yields after 15 min of device processing were comparable to the 60 min control. For interval operation, epithelial cell numbers closely matched the static cases. (D) Epithelial cell viability was ~80% for all control and device conditions. E) Samples were processed with integrated dissociation/filtration device at 10 mL/min for different amounts of time following 15 min of digestion device operation. One pass through the integrated device increased single epithelial cells by 40% compared to digestion alone, and yielded ~5.5-fold more single cells than a 15 min control. (F) Epithelial cell viability was comparable at ~85-90% for all conditions. Error bars represent standard errors from at least three independent experiments. * indicates $p < 0.05$ and ** indicates $p < 0.01$ relative to the control. # indicates $p < .05$ relative to the static digestion condition at the same digestion time.

Increasing flow rate to 20 mL/min improved these values to ~40% and 85%, respectively. Images of the tissue chamber were captured at the end of each experiment, and representative results are shown in Fig. 3.2B. We consistently observed tissue remaining in the chamber or adjacent channels at 10 mL/min flow rate, particularly after only 15 min of processing, corroborating low gDNA recovery results. After 60 min at 20 mL/min, we observed small amounts of tissue exclusively within channels/vias, which could account for the difference in gDNA recovery relative to the control. Another possibility is that cells were damaged or destroyed while recirculating through the system, which would have been washed away prior to gDNA isolation. To address the possibility of cell damage, we recirculated MCF-7 breast cancer cells through the system and assessed cell number and viability (Fig. 3.3). We indeed observed that cell recovery decreased by ~10% after recirculation through the digestion device for as little as 30 seconds at 20 mL/min flow rate. However, extending recirculation time to 10 min did not incur additional cell losses, and results were similar at lower flow rates and for recirculating through the peristaltic pump alone. Moreover, cell viability remained high for all conditions tested. Thus, we concluded that this decreased cell recovery was not caused by damage, but rather hold-up within the system or cell loss during transfer steps. Since cell loss was independent of flow rate, and 20 mL/min was more effective at clearing kidney from the tissue chamber and isolating gDNA, we selected this condition for the remainder of the study.

Next, we assessed single cells directly using flow cytometry. Cell suspensions were labeled using a panel of antibodies and fluorescent probes specific for EpCAM (epithelial cells), TER119 (red blood cells), CD45 (leukocytes), and 7-AAD (live/dead), as listed in Table 3.1. Operating the minced digestion device at 20 mL/min, we found that single

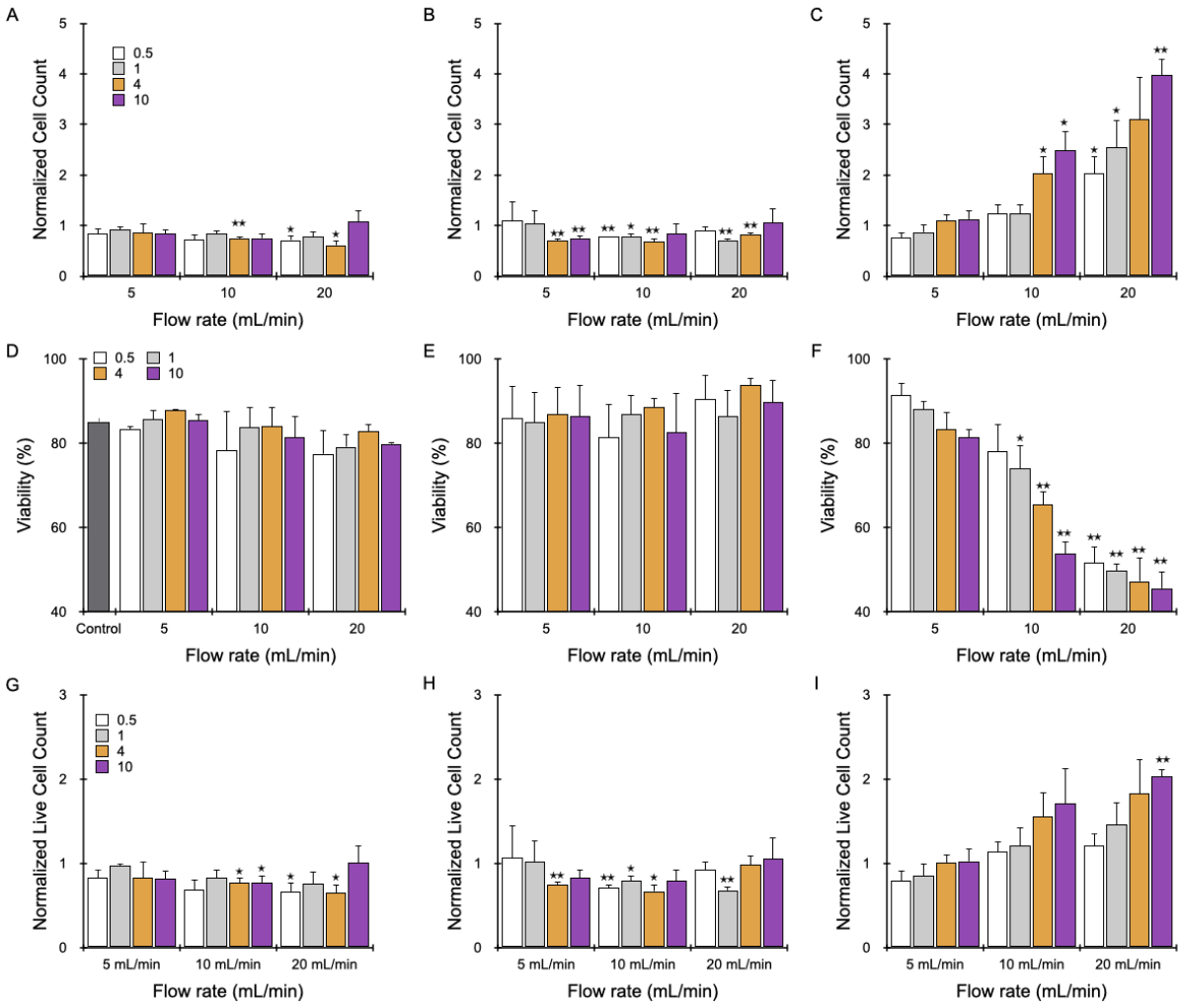

Figure 3.3: MCF-7 cell line optimization. (A-C) Normalized cell yields, (D-F) viability, and (G-I) normalized live cell yields were quantified after passing an MCF7 cell line model through the peristaltic pump tubing, with the minced digestion device, or with the dissociation portion of the integrated device in a recirculating peristaltic pump format. The condition without any devices was included to assess any effect of the peristaltic pumping mechanism, in terms of aggregate dissociation or viability, on the samples. Cell counts were normalized to the before count. For all flow rates and operation times, pump operation without (A) or with the digestion device (B) did not result in increased cell yields nor did it adversely impact cell viability (D&E). This suggests that the peristaltic pump and the digestion device do not cause sufficient shear forces to mechanically separate cellular aggregates and will not cause damage to cells and aggregates as they continue to recirculate through the pump and device system. (G&H) Normalized live cell yields for pump-only and digestion device conditions. Integrated dissociation/filtration device operation was tested in the recirculating peristaltic pump format, with flow circulated through the dissociation portion of the integrated device but not passed through the nylon filters of the filtration component for final sample collection, in order to avoid confounding results. (C) At 20 mL/min, the dissociation device resulted in 2 to 4-fold increases in single cells as processing time increased from 0.5 to 10 min, while at 10 mL/min flow rate, the dissociation device increased single cell yields by up to 2.5-fold for the 10 min condition. Operation at 5 mL/min did not affect single cell yields. (F) Viability at 20 mL/min was only ~50%, even for the shortest 0.5 min processing time compared to 85% for unprocessed controls. Viability at 10 mL/min also decreased with increasing processing time, although the shortest processing times remained comparable to controls. Operation at 5 mL/min did not impact cell viability. These results demonstrate that even short operating times at this high flow rate can adversely affect viability. 10 mL/min was chosen as the optimal operational flow rate for the integrated device moving forward, as short operation at this flow rate does not impact viability. (I) Normalized live cell yields for the integrated device are shown. Error bars represent standard errors from at least three independent experiments. * indicates $p < 0.05$ and ** indicates $p < 0.01$ relative to unprocessed control sample.

epithelial cell numbers increased with processing time, from 15 to 60 min, and produced up to ~14,000 cells/mg tissue (Fig. 3.2C). This represents a 1.5-fold increase when compared to the control, which was digested in collagenase for 60 min under constant agitation, followed by repeated pipetting and vortexing to replicate standard tissue dissociation protocols. Also of note, results after only 15 min of digestion device processing were statistically similar to the control that was digested for 60 min. We also investigated a new format, interval operation. This involved processing for a shorter initial time period, eluting the cell suspension, replacing collagenase, and continuing processing. For interval operation, we observed that epithelial cell numbers accumulated through each time point in a comparable manner to the static format. This demonstrates that cell samples can be recovered during the digestion process without compromising results. Epithelial cell viability was ~80% for all control and device conditions, confirming that device processing did not adversely affect liberated cells (Fig. 3.2D). Cell number and viability trends were similar for leukocytes (Fig. 3.4A and B).

Table 3.1: Flow cytometry probe panels

Assay	Probe	Fluorophore				Positive
		Kidney (Initial)	Kidney (Final)	Tumor	Liver	
EpCAM	Anti-EpCAM Ab (clone G8.8)-fluor	PE	PE	PE	N/A	Epithelial cells
TER-119	Anti-TER-119 Ab (clone TER-119)-fluor	AF647	AF647	AF647	AF647	Red blood cells
CD45	Anti-CD45 Ab (clone 30-F11)-fluor	AF488	BV510	BV510	BV510	Leukocytes
Viability	7-AAD	7-AAD	7-AAD	7-AAD	7-AAD	Dead cells
CD31	Anti-CD31 Ab (clone MEC13.3)-fluor	N/A	AF488	AF488	AF488	Endothelial cells
ASGPR1	Anti-ASGPR1 (clone 8D7)-fluor	N/A	N/A	N/A	PE	Hepatocytes

We then investigated whether the integrated dissociation/filtration device can further enhance single cell yield following digestion device processing. Ideally this would

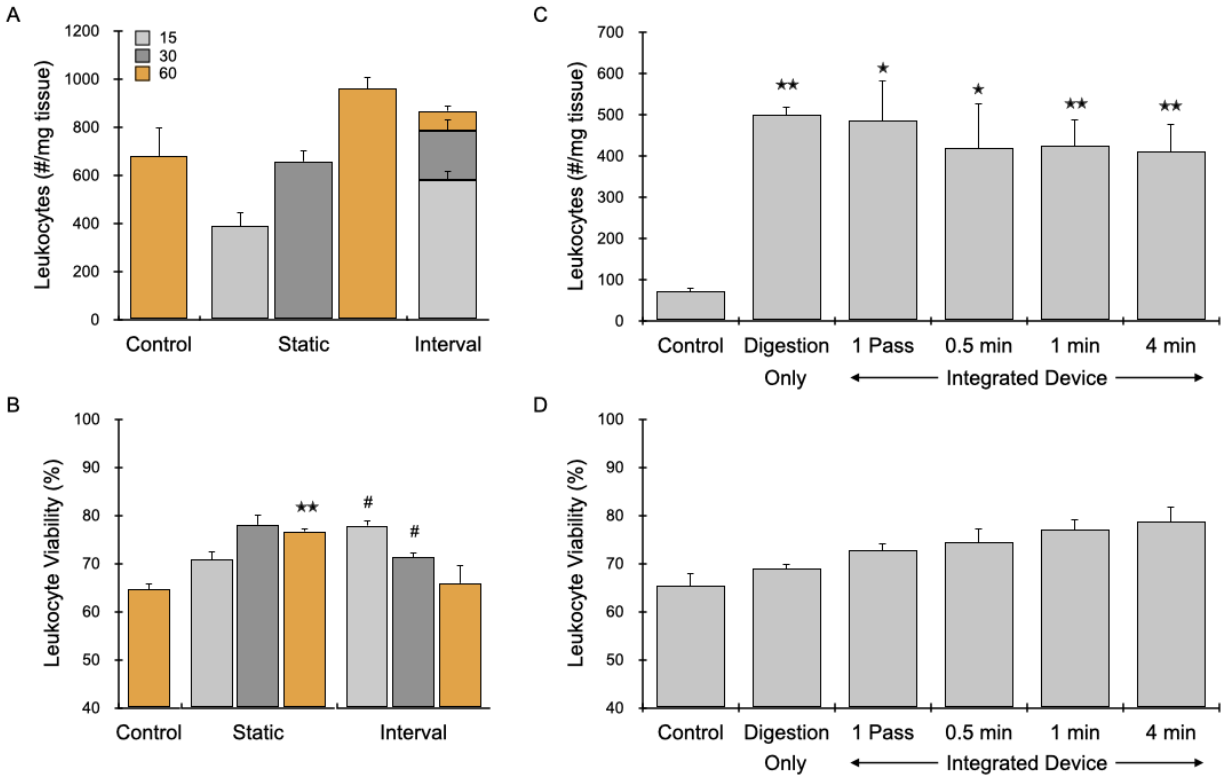

Figure 3.4: Leukocyte results from kidney optimization. (A) Leukocyte cell yields and (B) viability from digestion device optimization closely follow trends seen in epithelial cells (Fig 3.2C & 3.2D). (C) Leukocytes recoveries decreased modestly with additional recirculation processing after 1 pass. (D) Leukocyte viability was ~85-90% for all conditions. Error bars represent standard errors from at least three independent experiments. * indicates $p < 0.05$ and ** indicates $p < 0.01$ relative to the control. # indicates $p < .05$ relative to the static digestion condition at the same digestion time.

also be conducted at 20 mL/min using the recirculating format, but since neither have been tested before with this device we performed initial tests using the MCF-7 model (Fig. 3.3). We found that recirculation at 20 mL/min flow rate through the dissociation component, even for short periods of time, dramatically decreased viability. At 10 mL/min, single cell numbers increased by ~20% after 0.5 min, with no change in viability. This is similar to our previous work with MCF-7 cells being repeatedly pumped back and forth through the device.[39] Increasing recirculation time did enhance single cell numbers, but also decreased viability. Thus, we selected to test recirculation through the dissociation component at 10 mL/min for short durations using digested kidney samples. Experiments were performed by processing minced kidney with the digestion device for 15 min, connecting the outlet to the

inlet of the dissociation component, and processing further. As a final step, sample was passed through the series of nylon mesh filters in the filtration component, with pore sizes of 50 and 15 μm, and collected. Single epithelial cell recovery numbers are presented in Fig. 3.2E. The digestion device produced 4-fold more single cells than the control that was also digested for 15 min. A single pass through the integrated device increased single epithelial cells by ~40% compared to digestion alone, which was ~5.5-fold greater than the control. Recirculation through the branching channel array produced fewer cells than the single pass, even after short periods. Epithelial cell viability was at ~85-90% for all conditions (Fig. 3.2F). Similar results were observed for leukocytes (Fig. 3.4). Taken together, these data suggest that recirculation, even for only 30 seconds or ~10 device passes, may result in over-processing of kidney samples. We note that cell destruction may not be reflected in viability measurements because cells could be reduced to debris that is either removed by washing or excluded in the flow cytometry gating scheme. Based on these results, a single pass through the integrated dissociation/filtration device was chosen as optimal for kidney. It should also be noted that by utilizing the integrated device downstream of the minced digestion device, a cell straining step would no longer be required prior to downstream analysis.

3.2.3 Single Cell Analysis of Murine Kidney

We further evaluated kidney under different digestion times using the full microfluidic platform. We also added endothelial cells (via CD31, Table 1) to the flow cytometry detection panel, since they are notoriously difficult to isolate using traditional dissociation methods.[84] Minced tissue was loaded into the digestion device and processed under the static format for 15 or 60 min, as well as interval time points of 1, 15, and 60 min.

Samples were then passed through the integrated dissociation/filtration device one time. Controls were minced, digested for 15 or 60 min, disaggregated by vortexing/pipetting, and filtered using a cell strainer. Results for epithelial cells are presented in Fig. 3.5A, and are generally similar to the optimization experiments in Fig. 3.2C. A notable change was that device processing, under both the static and interval formats, increased to ~20,000 cells/mg tissue at 60 min. This represents a similar 40% enhancement of single cells after treatment

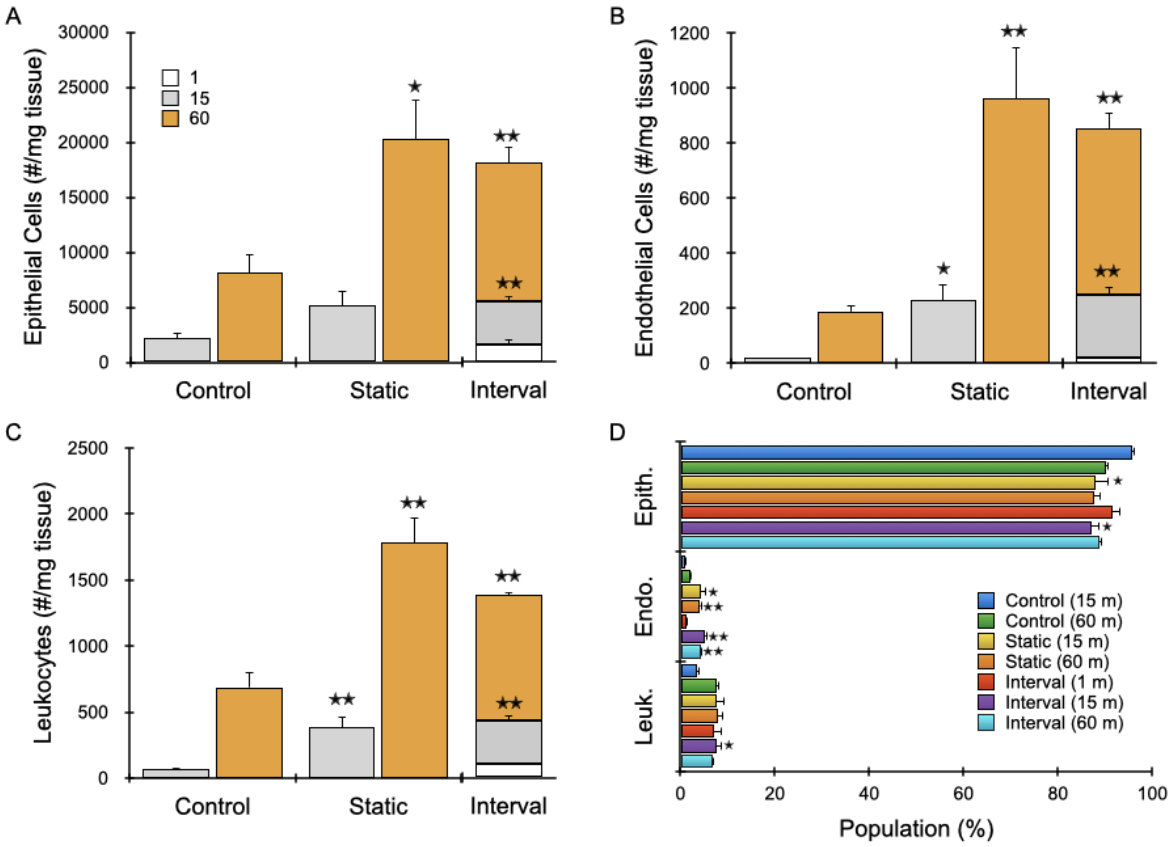

Figure 3.5: Single cell analysis of murine kidney. Kidney processing was evaluated after different digestion times using the full microfluidic device platform under either a static or interval format. Following digestion device processing, samples were passed through the integrated dissociation/filtration device one time. (A) Static and interval formats at 60 min doubled the epithelial cell yields of the 60 min control. A 1 min interval produced ~1500 epithelial cells/mg, comparable to the 15 min control. (B) Endothelial and (C) leukocyte cell yields followed trends similar to epithelial yields. Device processing was particularly effective for endothelial cells, as the 60 min condition yielded 5-fold more cells than the control. (D) Population distributions for each cell type that were liberated under the different processing conditions. Relative to the 60 min control, endothelial cells were enriched for all device conditions except the 1 min interval. Leukocytes were under-represented in the 15 min control. Error bars represent standard errors from at least three independent experiments. * indicates $p < 0.05$ and ** indicates $p < 0.01$ relative to the control at the same digestion time. # indicates $p < .05$ relative to the static digestion condition at the same digestion time.

with the integrated dissociation/filter, and is more than double the 60 min control. Surprisingly, the 1 min interval produced ~1500 epithelial cells/mg, which was similar to the 15 min control. This time point was chosen primarily to eliminate erythrocytes, which were found to be present at high levels (~50%) in this interval relative to the 60 min time point (Fig. 3.6). Findings for endothelial cells (Fig. 3.5B) and leukocytes (Fig. 3.5C) were

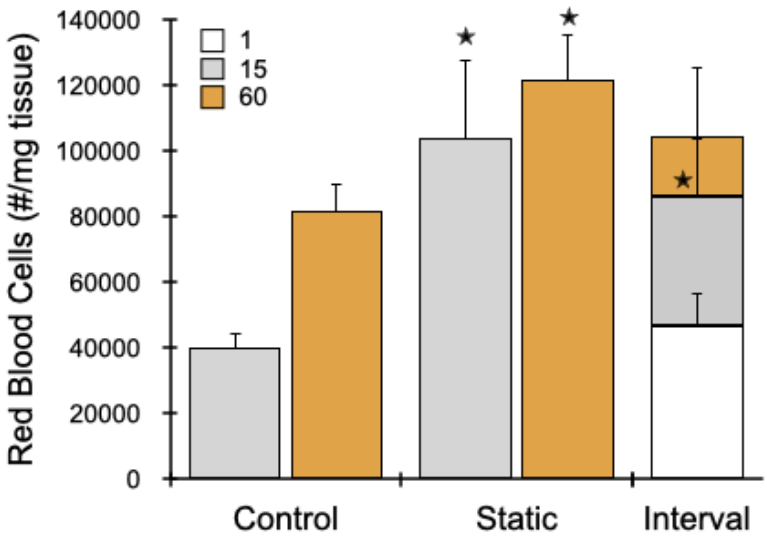

Figure 3.6: Erythrocyte cell yields from murine kidney. Most RBCs were eluted at earlier device timepoints. 1 min device interval was employed to remove as may erythrocytes as possible. Error bars represent standard errors from at least three independent experiments. * indicates $p < 0.05$ relative to the control at the same digestion time.

generally similar to epithelial cells. Device processing was particularly effective for endothelial cells, exceeding the control by more than 5-fold at 60 min. We note a slight decrease in total cell recovery for the interval sums relative to the 60 min static condition for all cell types, although this was not statistically significant. This modest decrease may have been due to sample loss during transfer and priming steps or elution of cell clusters at the earlier intervals that could have been broken down more effectively with additional time in the digestion device. Population distributions for each cell type that were collected under

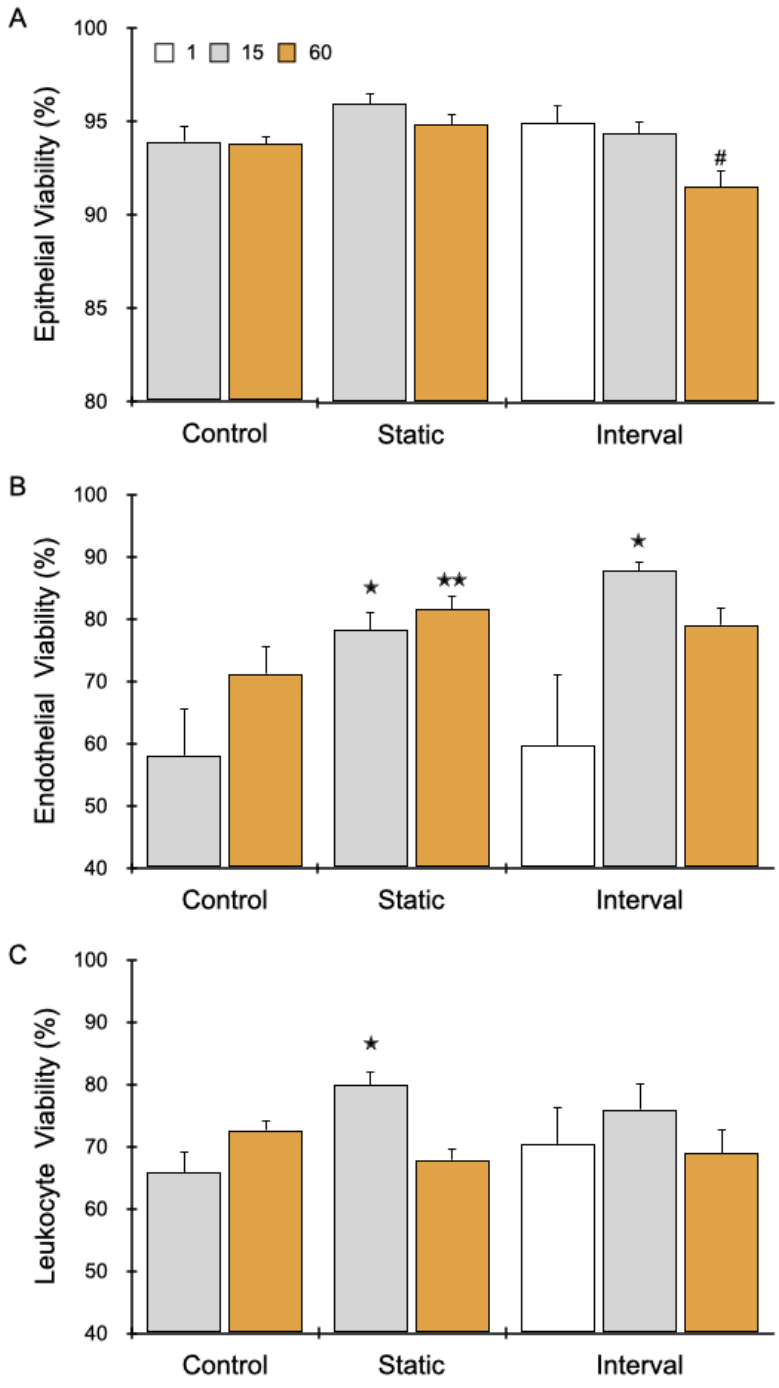

Figure 3.7: Murine kidney cell viability. Viability for all three cell types after device processing were similar to or exceeded the controls. (A) Epithelial cell viability was highest, at ~95% for all conditions. (B) Endothelial cell and (C) leukocyte viabilities ranged from ~60% to 90%, with the 60 min control at ~70% in both cases. Device processing resulted in higher viabilities for endothelial cells at all conditions except the 1 min interval, and leukocytes were elevated at the 15 min time points (static and interval). Error bars represent standard errors from at least three independent experiments. * indicates $p < 0.05$ and ** indicates $p < 0.01$ relative to the control at the same digestion time. # indicates $p < .05$ relative to the static digestion condition at the same digestion time.

the different processing conditions are shown in Fig. 3.5D. Relative to the 60 min control, endothelial cells were enriched for all device conditions except the 1 min interval. This is highly promising given the recent claim that certain cell types, including endothelial cells, are underrepresented in cell-based single cell analyses because they are challenging to dissociate.[84] Leukocytes were present at similar levels except the 15 min control, where they were under-represented. Viability for all three cell types after device processing were similar to or exceeded the controls (Fig. 3.7).

Next we performed scRNA-seq, which has been used to catalogue the diverse cell types and functional states residing within the kidney.[63,99] These atlasing efforts seek to provide comprehensive cell reference maps that will are critical to understanding kidney biology under normal and diseased scenarios.[63,100–102] Kidney tissue was processed using the device platform and collected at 15 and 60 min intervals, and we also tested a 60 min control for comparison. We isolated live single cells from debris and dead cells using fluorescence-activated cell sorting (FACS), loaded on to a droplet-enabled 10X Chromium platform, and sequenced a total 34,034 cells at an average of ~60,000 reads per cell. After quality control filtering of the data, we used Seurat to identify seven cell clusters (Fig. 3.8A). This included two distinct populations of proximal tubules (convoluted or S1 and straight or S2-S3), endothelial cells, macrophages, B lymphocytes, T lymphocytes, and a cluster containing cells from the distal convoluted tubule (DCT), Loop of Henle (LOH), and collecting duct (CD), as well as mesangial cells (MC). Importantly, all seven clusters were represented in control and device conditions (Fig 3.9A). The relative number of cells in each cluster are shown in Fig. 3.8B. Proximal tubules were the predominant cell population, with the S1 and S2-S3 clusters combining to represent ~53% of the control, which closely matches a previous mouse kidney

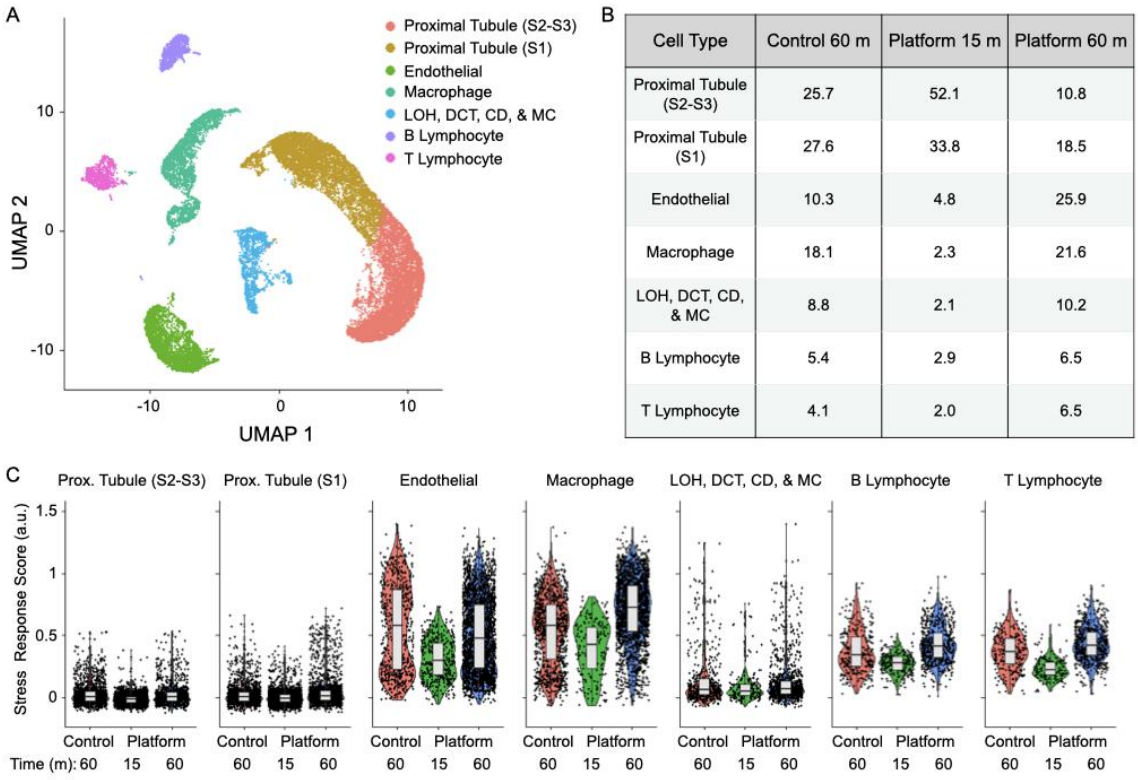

Cell Type	Control 60 m	Platform 15 m	Platform 60 m
Proximal Tubule (S2-S3)	25.7	52.1	10.8
Proximal Tubule (S1)	27.6	33.8	18.5
Endothelial	10.3	4.8	25.9
Macrophage	18.1	2.3	21.6
LOH, DCT, CD, & MC	8.8	2.1	10.2
B Lymphocyte	5.4	2.9	6.5
T Lymphocyte	4.1	2.0	6.5

Figure 3.8: Single cell RNA sequencing of murine kidney. Kidney processing was evaluated after 15 or 60 min intervals using the full microfluidic device platform and compared to a 60 min control digestion. (A) UMAP showing 7 cell clusters. (B) Table showing population frequencies in each cell cluster. Proximal tubules were enriched in the 15 min platform interval and depleted in the 60 min platform interval relative to the control, while the remaining populations were depleted in the 15 min platform interval and enriched in the 60 min platform interval. (C) Stress response scores were generally lower for the 15 min device interval, and for proximal tubule cell types.

atlas.[63] Proximal tubules were further enriched in the 15 min device condition, comprising ~86% of the cell suspension. The other cell populations were under-represented relative to the control, most by ~2-fold but reaching as high as 8-fold for macrophages. However, it is unclear whether this was caused by diminished recovery of these cell types or simply dilution by proximal tubules. The 60 min device condition only contained ~29% proximal tubules, but this was likely due to the fact that a significant number had already been removed in the 15 min interval sample. Another factor is that endothelial cells were clearly enriched at 60 min, increasing to ~25% of the suspension while the remaining cell types

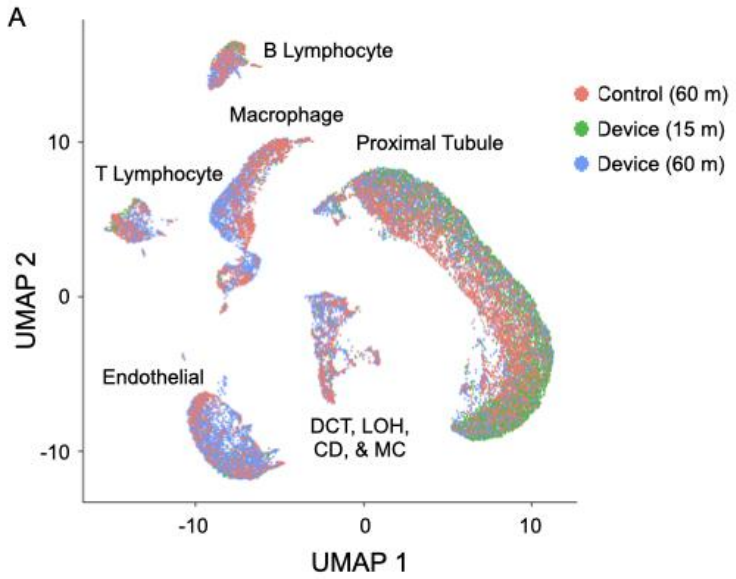

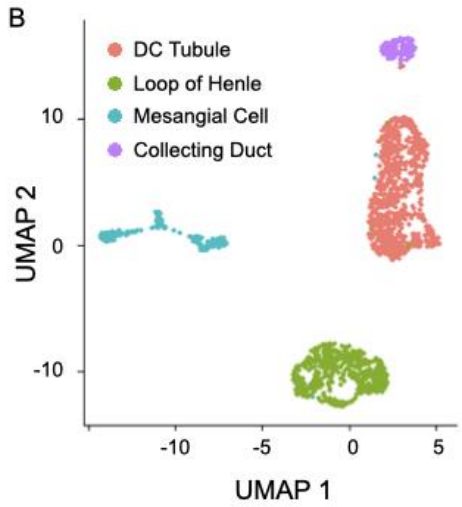

C

Cell Type	Control 60 m	Device 15 m	Device 60 m
Distal Convoluted Tubule	4.3	0.8	4.7
Loop of Henle	2.2	0.8	3.6
Mesangial Cell	1.3	0.2	1.4
Collecting Duct	0.9	0.4	0.6

Figure 3.9: Kidney subclustering. (A) All kidney clusters were represented in control and device conditions. (B) Subclustering of DCT, LOH, CD, & MC cluster identified 4 subclusters. (C) Population frequencies in each cell cluster. Distal convoluted tubule, loop of Henle, and mesangial cells were depleted in the 15 min platform interval and enriched in the 60 min platform interval relative to the control. Collecting duct cells were depleted in both the 15 and 60 min platform intervals.

remained closer to control values. Similar trends were observed for each processing condition within the DCT, LOH, DC, and MC sub-cluster (Fig s. 3.9B and C). Before population percentages obtained from scRNA-seq in Fig. 3.8B can be compared to flow cytometry results in Fig. 3.5D, consideration must be given to which cell populations were most likely to be EpCAM positive. DCT and CD cells have been shown to express EpCAM at high levels, while

proximal tubules and LOH cells ranged from low to undetectable.[103] We stained EpCAM using the brightest fluorophore, phycoerithrin (PE), to help discern low level expression, but it is possible that some cells were not detectable. Assuming a full accounting of proximal tubule, DCT, LOH, CD, & MC clusters, we arrive at prospective EpCAM positive population percentages of ~62, 88, and 40% for the control, device 15 m, and device 60 m conditions, respectively. This is directly in line with flow cytometry results for the 15 m device, but considerably lower for both 60 m cases. We note that if flow cytometry missed any cells from these clusters due to low EpCAM expression, this would only widen the disparity. We contend that the comprehensive manner in which scRNA-seq identifies cell types is superior to flow cytometry, particularly when a clear positive biomarker for each cell sub-population is lacking. Flow cytometry is better suited to cell counting, however, and based on those results, device processing consistently produced comparable numbers of cells at 15 m and at least 50% more cells at 60 m relative to the control. This would partially offset the lower proximal tubule content for the 60 m device condition, and enhance enrichment of other cell types. As an approximation, we weighted the 60 m device population percentages in Fig. 3.8B by a factor of 1.5 and added this to the 15 m results (see Table 3.2). This provided aggregate device yields that were ~4-fold greater than the control for endothelial cells and ~2- to 2.5-fold greater for the other cell types, which closely matches flow cytometry results in Fig. 3.5A-C. While this is only a rough approximation, it does appear that the relative numbers within each cell type is consistent between the two single cell detection methods. However, the relative numbers across the cell types varies considerably, which may have occurred

Table 3.2: Weighted kidney population analysis. As a crude estimation, 60 m device population percentages in Fig. 3.8B were weighted by a factor of 1.5 and added this to the 15 m results. This provided aggregate device yields that were ~4-fold greater than the control for endothelial cells and ~2- to 2.5-fold greater for the other cell types, which closely matches flow cytometry results in Fig. 3.5A-C.

Cell Type	Device 60 m (weighted)	Device Total (weighted)	Device Total (Norm. to control)	Device Total (%)
Proximal Tubule (S2-S3)	16.2	68.3	2.7	27.3
Proximal Tubule (S1)	27.8	61.6	2.3	24.6
Endothelial	38.9	43.7	4.2	17.5
Macrophage	32.4	34.7	1.9	13.9
LOH, DCT, CD, & MC	15.3	17.4	2.0	7.0
B Lymphocyte	9.8	12.7	2.3	5.1
T Lymphocyte	9.8	11.8	2.9	4.7

during sorting or droplet loading in the 10X Chromium system, as has been documented previously.[104] Our results suggest that endothelial cells and leukocytes would have been preferentially selected during these steps.

Finally, we evaluated stress response genes, which are a concern because they can complicate cell type identification and interfere with transcriptomic analyses. Induction of stress responses have been linked to both digestion time and temperature in tissue dissociation protocols.[17,84,87,88] Since a large number of genes have been implicated, we calculated a "stress response score" based on previous scRNA-seq work,[5,88] and the results are presented in Fig. 3.8C. We found that stress response scores were cell type specific, with proximal tubules exhibiting the lowest values, as recently reported.[87] Overall, stress

response scores were generally lower for the 15 m device condition compared to the 60 min device and control cases. This is consistent with previous findings that shortening enzymatic digestion time reduces dissociation-induced transcriptional artifacts.[17,87] Importantly, we found no evidence that continued exposure to fluid shear stresses within the digestion device heightened stress response for any cell type. This suggests that time was the predominant factor, which can be mitigated using the interval concept that can easily be employed with the microfluidic platform. Ideally, more intervals would be employed to shorten time for these artifactual transcription changes to take place. The intervals could be analyzed separately, with some cell types potentially being enriched, or stored and eventually combined into a single sample that most accurately represents the original kidney samples.

3.2.4 Processing and Single Cell Analysis of Murine Mammary Tumor Tissue

Solid tumors can exhibit high degrees of intratumoral heterogeneity, which has been directly implicated in cancer progression, metastasis, and the development of drug resistance.[2,3] This heterogeneity has successfully been captured using scRNA-seq and linked to survival for glioblastoma, drug resistance in melanoma, and prognosis for colorectal cancer.[5,42,44,45,62,105] Moreover, it is expected that expanded application of scRNA-seq in clinical settings will soon emerge to provide critical molecular and cellular information for guiding personalized therapies.[106] Due to abnormal extracellular matrix composition and density, however, tumor tissues are considered to be amongst the most difficult epithelial tissues to dissociate.[59] We evaluated microfluidic processing of mammary tumors that spontaneously arise in MMTV-PyMT transgenic mice, which were resected and minced into ~1 mm^3 pieces. We first tested the minced digestion and integrated dissociation/filtration devices separately to optimize performance and corroborate kidney results. The digestion

device generated ~2-fold more EpCAM+ epithelial cells than the controls after 15 and 30 min, and the difference extended to 2.5-fold at 60 min (Fig. 3.10A). Viability decreased with digestion time from 80% to 73% for the controls, while device processed samples remained at ~85% for all time points (Fig. 3.10B). We then tested the integrated dissociation/filtration device and again found that a single pass was optimal (Fig. 3.10C and 3.10D). In this case, recirculation for 1 and 4 min performed similarly with respect to cell numbers, but had lower viability. Results for the full microfluidic device platform are shown in Fig. 3.11, and are generally similar to kidney. Epithelial, endothelial, and leukocyte cell counts per mg tumor tissue were all lower than kidney by 2- to 3-fold. However, the device platform still produced

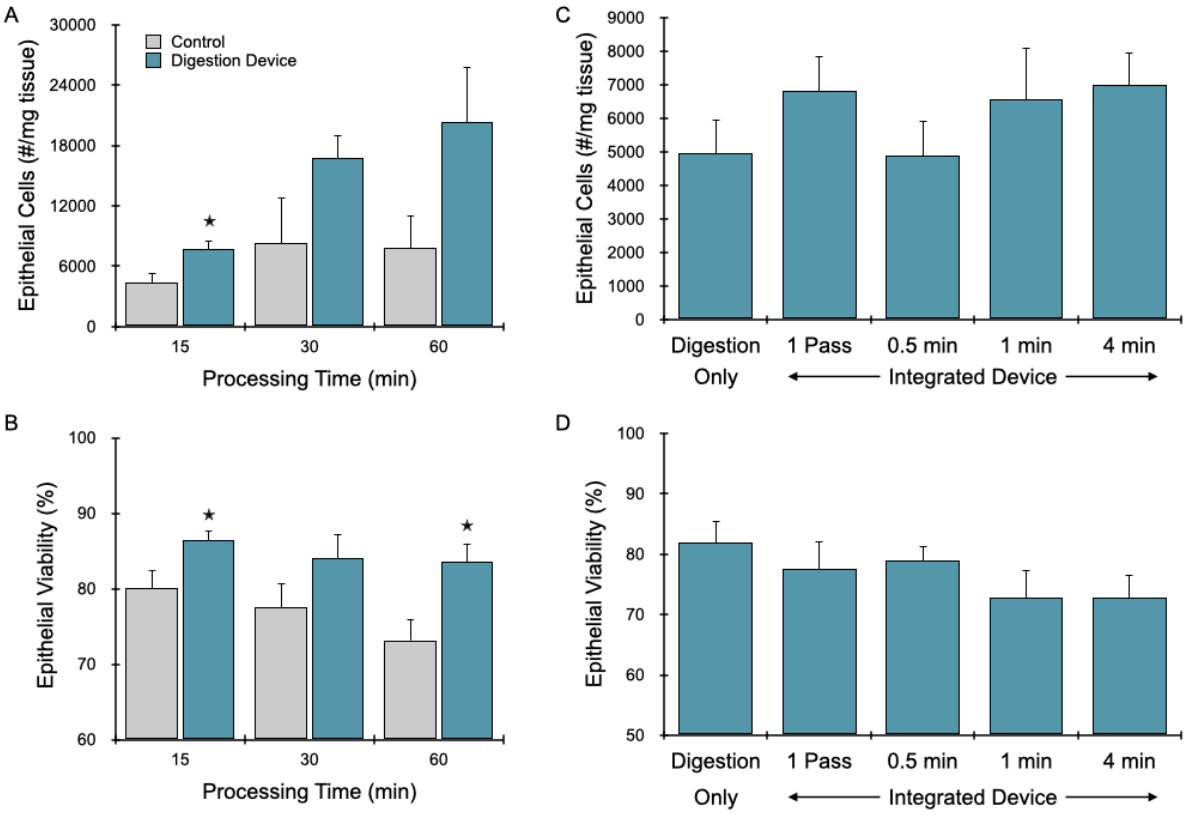

Figure 3.10: Optimization with murine mammary tumor. (A) Digestion device generated ~2- to 2.5-fold more epithelial cells than the controls at all timepoints. (B) Viability for the controls was less than device conditions at all timepoints. Following 15 min of digestion device operation, a single pass through the integrated dissociation/filtration device was found optimal in terms of (C) epithelial cell yields and without compromising (D) viability. Error bars represent standard errors from at least three independent experiments. * indicates $p < 0.05$ relative to the control at the same digestion time.

significantly more cells than controls. Epithelial cells were ~2-fold higher at both time points (Fig. 3.11A). Endothelial cells were liberated much more effectively by device processing, with 5-fold more cells recovered after 15 min and 10-fold more after 60 min (Fig. 3.11B). Leukocytes increased by 3- and 5-fold after 15 and 60 min, respectively (Fig. 3.11C). The interval format produced similar total epithelial and leukocyte cell numbers when compared to the corresponding static time point. However, ~30% more endothelial cells were obtained from intervals. We also note that a remarkably large number of epithelial cells (>15%) were

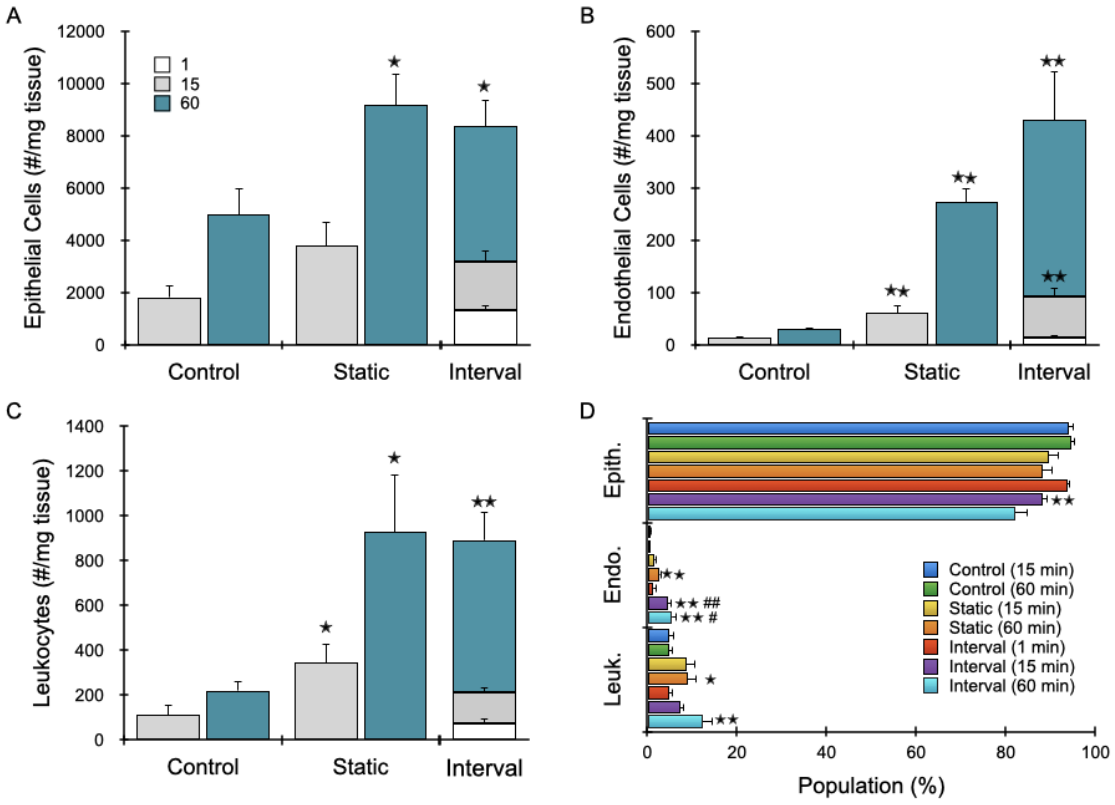

Figure 3.11: Single cell analysis of murine mammary tumor tissue. Mammary tumor was processed with the full microfluidic device platform under the same processing times and conditions as with kidney. Epithelial, endothelial, and leukocyte cell yields were all lower than kidney by 2- to 3-fold, but the device platform still produced significantly more cells than the control. (A) Epithelial cells were ~2-fold higher for device conditions at both 15 and 60 time points. (B) Endothelial cells were significantly more effectively liberated by device processing. 5- and 10-fold more cells were recovered after 15 min and 60 min, respectively. (C) With device processing, leukocytes increased by 3- and 5-fold after 15 and 60 min, respectively. The interval format produced similar total cell recoveries to the corresponding static time point for both leukocytes and epithelial cells. ~30% more endothelial cells were obtained from intervals compared to the static condition. (D) Population distributions for each cell type that were liberated under the different processing conditions. Device processing enriched for endothelial cells and leukocytes at all but the 1 min time point, which was similar to controls. * indicates $p < 0.05$ and ** indicates $p < 0.01$ relative to the control at the same digestion time. # indicates $p < .05$ and ## indicates $p < .01$ relative to the static digestion condition at the same digestion time.

obtained at the 1 min interval. Relative population percentages are shown in Fig. 3.11D. Device processing enriched for endothelial cells and leukocytes at all but the 1 min time point, which remained similar to controls. Viability for all three cell types under most device-

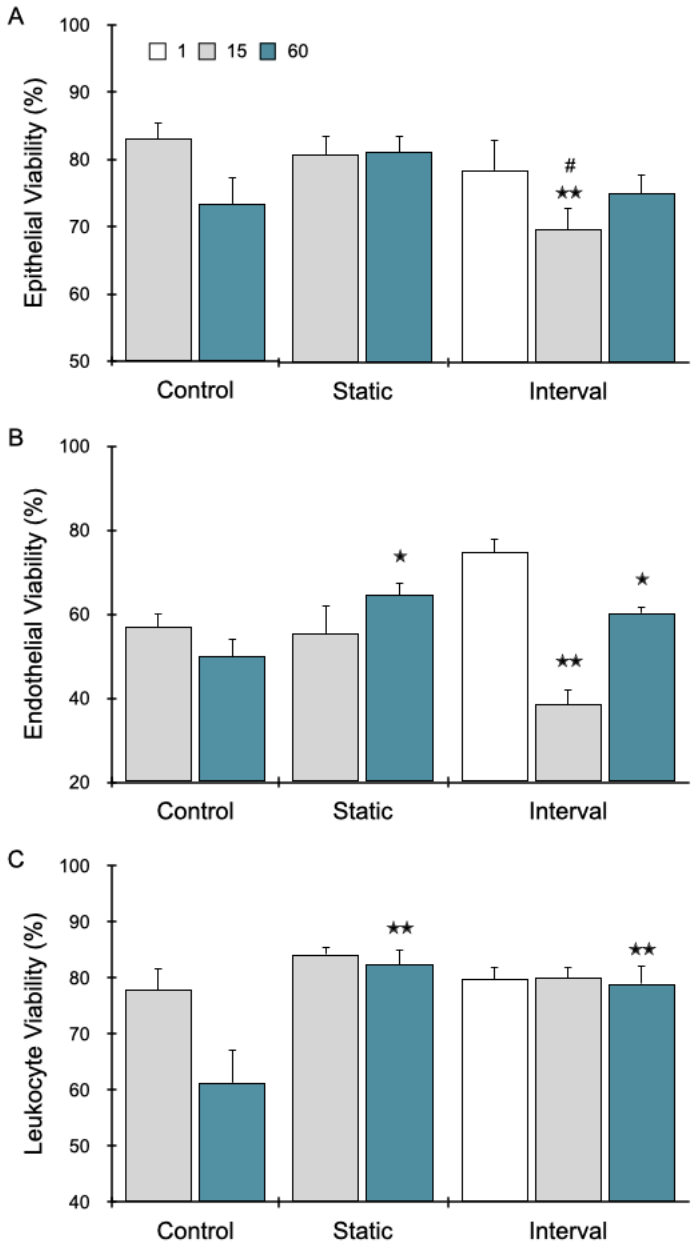

Figure 3.12: Murine mammary tumor cell viability. (A) Epithelial cell viabilities were ~70-80% for all conditions. (B) Endothelial cell viability was generally low at ~50-60%. However, the 1 min device interval was higher at 75%, while the 60 min control and 15 min device interval were lower at 50% and 40%, respectively. (C) Leukocyte viability remained ~80% for all but the 60 min control, which was ~60%. Error bars represent standard errors from at least three independent experiments. * indicates $p < 0.05$ and ** indicates $p < 0.01$ relative to the control at the same digestion time. # indicates $p < .05$ relative to the static digestion condition at the same digestion time.

processing conditions were similar to the 15 min control and exceeded the 60 min control (Fig. 3.12). Thus, for tumor, the microfluidic device platform liberated more single cells, while also preserving cell viability at longer time points.

We then performed scRNA-seq, again using the 15 and 60 min device intervals and the 60 min control. A total 24,527 cells were sequenced at an average of ~45,000 reads per cell. We identified 6 main clusters that corresponded to epithelial cells, macrophages, endothelial cells, T lymphocytes, fibroblasts, and granulocytes (Fig. 3.13A). Epithelial cells were the predominant cell population, representing 62.0% of control cells (Fig. 3.13B).

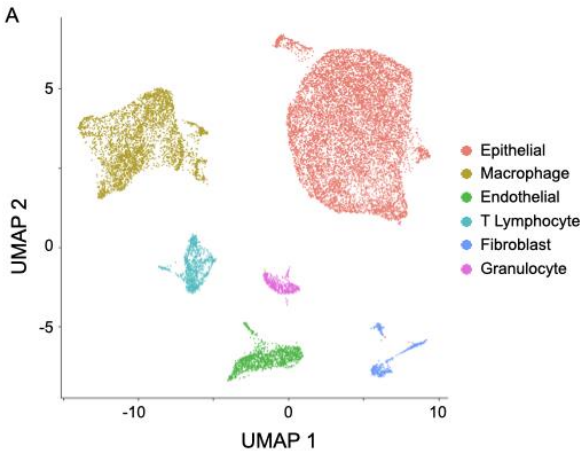

B

Cell Type	Control 60 m	Platform 15 m	Platform 60 m
Epithelial	62.0	68.5	43.6
Macrophage	19.9	18.5	28.8
Endothelial	5.9	4.6	13.6
T Lymphocyte	5.8	4.3	6.3
Fibroblast	1.1	1.8	6.5
Granulocyte	5.3	2.2	1.3

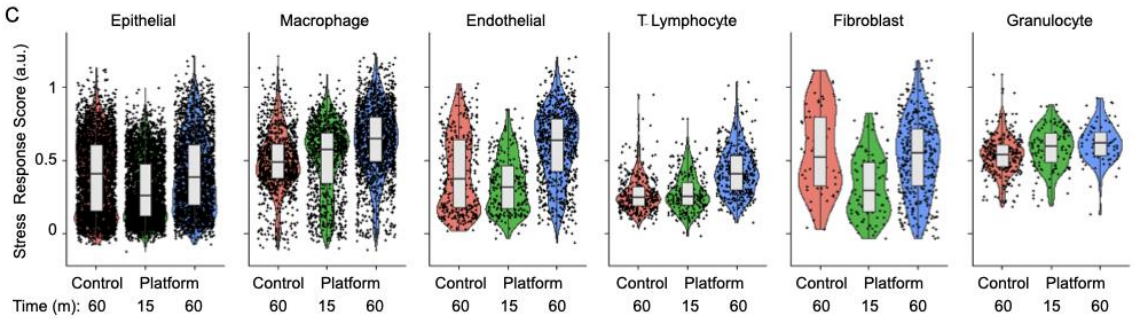

Figure 3.13: Single cell RNA sequencing of murine mammary tumor. Tumor processing was evaluated after 15 or 60 min intervals using the full microfluidic device platform and compared to a 60 min control digestion. (A) UMAP showing 6 cell clusters. (B) Table showing population frequencies in each cell cluster. Epithelial cells were enriched in the 15 min platform interval and depleted in the 60 min platform interval relative to the control, while macrophages, endothelial and T lymphocytes were depleted in the 15 min platform interval and enriched in the 60 min platform interval. Fibroblasts were enriched in both platform conditions while granulocytes were depleted in both platform conditions. (C) Stress response scores were generally similar across conditions and cell types.

Similar to kidney, device processing produced a higher percentage of epithelial cells in the 15 m interval relative to the 60 m, but differences were now more modest. We reiterate that epithelial percentages were lower at 60 m due to removal of a significant portion in the 15 m interval, as well as a clear enrichment of other cell types, this time endothelial cells and fibroblasts. We also identified three sub-clusters within the epithelial population corresponding to luminal, basal, and proliferating luminal cells based on expression of Krt14, Krt18, and Mki67 genes, respectively (Fig. 3.14). The luminal sub-type dominated, as expected since MMTV-PyMT is a luminal tumor. The basal subpopulation was enriched with

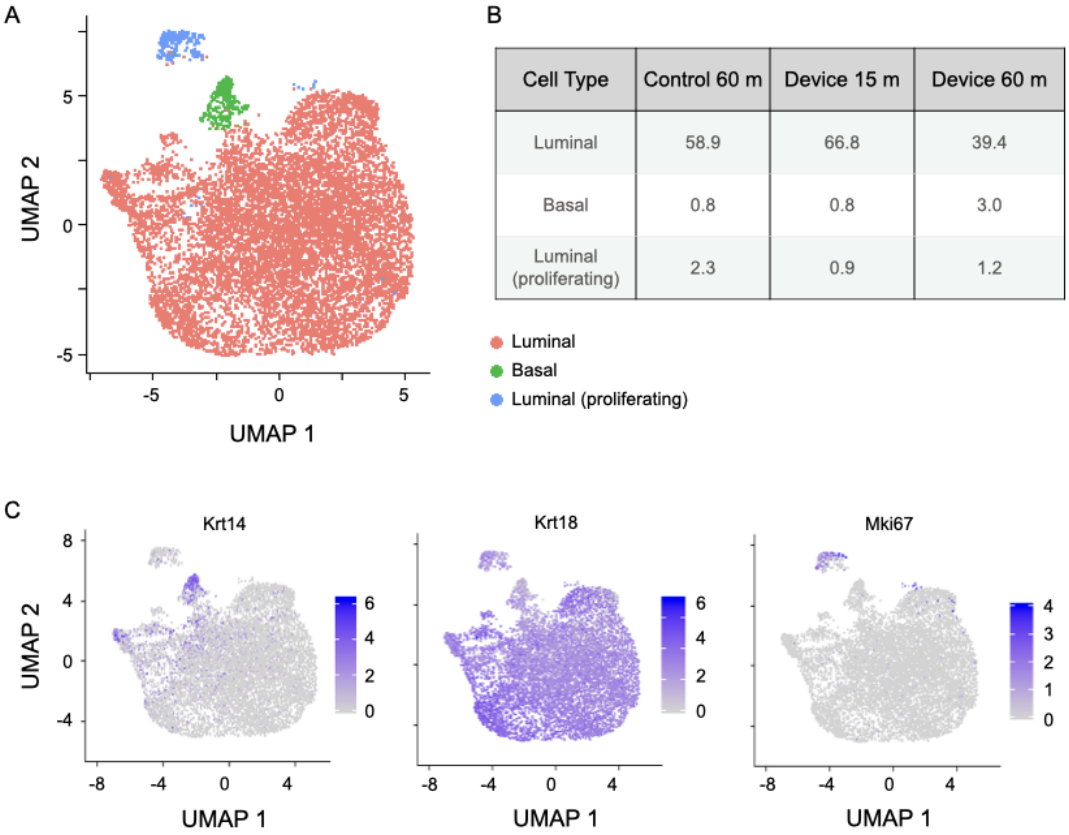

Cell Type	Control 60 m	Device 15 m	Device 60 m
Luminal	58.9	66.8	39.4
Basal	0.8	0.8	3.0
Luminal (proliferating)	2.3	0.9	1.2

Figure 3.14: Single cell RNA sequencing of murine mammary tumor. Tumor processing was evaluated after 15 or 60 min intervals using the full microfluidic device platform and compared to a 60 min control digestion. (A) UMAP showing 6 cell clusters. (B) Table showing population frequencies in each cell cluster. Epithelial cells were enriched in the 15 min platform interval and depleted in the 60 min platform interval relative to the control, while macrophages, endothelial and T lymphocytes were depleted in the 15 min platform interval and enriched in the 60 min platform interval. Fibroblasts were enriched in both platform conditions while granulocytes were depleted in both platform conditions. (C) Stress response scores were generally similar across conditions and cell types.

device processing, while the proliferating luminal subpopulation was under-represented. Comparing cell populations between scRNA-seq and flow cytometry was more straightforward for tumor, however, attention must be drawn to the fact that fibroblasts were not detected by flow cytometry, and account for a significant component of the 60 m device interval. As with kidney, tumor epithelial percentages were significantly higher in flow cytometry data, which would again suggest sorting and/or droplet encapsulation efficiencies were higher for endothelial cells and leukocytes. If we again approximate total cell numbers using the same weighting factors as with kidney (1 and 1.5 for 15 and 60 m intervals, respectively, see Table 3.3), the difference between aggregate device and control values would be ~2-fold for epithelial cells and 2.5-3-fold for T lymphocytes and macrophages, similar to flow cytometry results in Figs. 3.11A and C. It is noted that

Table 3.3: Weighted tumor population analysis. As a crude estimation, 60 m device population percentages in Fig. 3.13B were weighted by a factor of 1.5 and added this to the 15 m results. This provided aggregate device yields that were ~2-fold greater than the control for epithelial cell and 2.5-3-fold greater for T lymphocytes and macrophages, similar to flow cytometry results in Figs. 3.11A and C.

Cell Type	Device 60 m (weighted)	Device Total (weighted)	Device Total (Norm. to control)	Device Total (%)
Epithelial	65.4	133.9	2.2	53.5
Macrophage	43.2	61.7	3.1	24.7
Endothelial	20.4	25.0	4.2	10.0
T Lymphocyte	9.5	13.8	2.4	5.5
Fibroblast	9.8	11.6	10.5	4.6
Granulocyte	2.0	4.2	0.8	1.7

endothelial cells would be ~4-fold greater for the device platform, which is lower than the 10-fold difference by flow symmetry in Fig. 3.11. Fibroblasts would also be 10-fold enriched by the device platform. Our results confirm that tissue processing with the microfluidic device platform can improve isolation of difficult to liberate cell types such as endothelial cells and fibroblasts from solid tumors.

Finally, we performed the same stress response scoring described for kidney. The importance of stress responses can be heightened for tumor since some response genes, such as members of the Jun and Fos families, have been associated with metastatic progression and drug resistance.[87,107–109] Interestingly, stress responses in tumor were much more similar across cell types and conditions (Fig. 3.13C). It is possible that tumor cells are more sensitive to dissociation-induced transcriptional changes, and that even shorter intervals would be necessary to lower these responses.

3.2.5 Isolation of Hepatocytes from Murine Liver

The liver plays a major role in drug metabolism and is frequently assessed for drug-induced toxicity. In fact, liver damage is one of the leading causes of post-approval drug withdrawal.[74,110,111] Thus, *in vitro* screening of drugs against liver tissue is a critical component of preclinical testing. Increasingly, organ-on-a-chip systems are being employed to better maintain hepatocyte functionality and activity in culture settings and to enable personalized testing on viable cells isolated from a patient's primary tissue.[79,112] While liver is softer and generally easier to dissociate, hepatocytes are well known to be fragile, and thus liver presents a unique dissociation challenge.[58] As such, we hypothesized that shorter device processing times would be effective at liberating hepatocytes and other cell types from liver. For these experiments, murine liver was minced into 1 mm^3 pieces and

hepatocytes were detected based on ASGPR1 expression. We first processed liver using the minced digestion device for either 15 or 60 min. After 15 min, hepatocyte recovery was ~4-fold higher for the device than the comparable control (Fig. 3.15A). Continued digestion of the control increased hepatocyte numbers further. Counterintuitively, continued processing in the digestion device diminished hepatocyte yield by approximately half. We believe this finding was caused by the combination of two factors: softer liver tissue is effectively broken down at earlier time points and fragile hepatocytes are more sensitive to damage in the recirculation format. We also tested a single pass through the integrated dissociation/filtration device following both 15 and 60 min digestion device processing, and found that hepatocyte recovery decreased in both cases. While general hepatocyte fragility could also be factor in this case, we hypothesized that their large size (~30 μm) could be the primary issue. Specifically, the 15 μm filter employed near the outlet of the filtration component may have retained or damaged hepatocytes. It also appears that damage may have been additive, as viability dropped to 45% for sample that was processed for 60 min in the digestion device and then passed through the integrated device, while all other conditions were ~80% (Fig. 3.15B). As expected, removing the 15 μm filter from the integrated dissociation/filtration device increased hepatocytes by 30% relative to the digestion device alone and by nearly 3-fold relative to the control, while preserving viability (Fig. 3.16).

Based on the initial optimization studies, we concluded that the microfluidic device platform should utilize short term digestion device times and use the modified

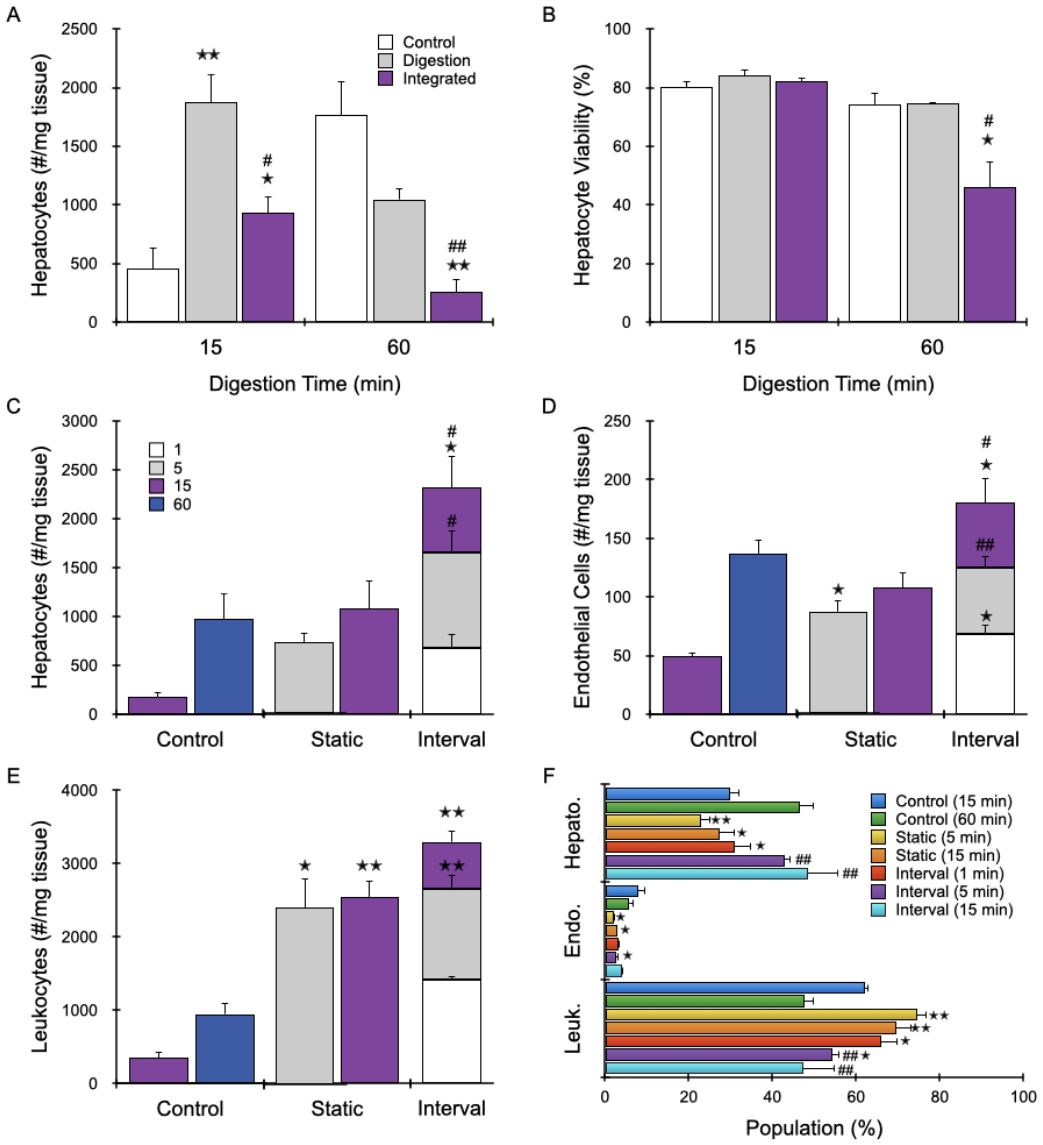

Figure 3.15: Single cell analysis of murine liver. (A) Hepatocyte yields increased with digestion time for the controls. Continued processing in the digestion device diminished hepatocyte yield by half, likely due to softer liver tissue being effectively broken down by earlier time points and fragile hepatocytes being damaged by the recirculation format. (B) Hepatocyte viability was ~75-80% for all conditions except the 60 min integrated condition which dropped to 45%. (C-F) Shorter digestion device operating times and a single pass with the modified dissociation/filtration device (50 µm filter only) was used to avoid over processing and maximize hepatocyte recovery. (C) A 5 min digestion device time point yielded ~700 hepatocytes/mg liver tissue, 4-fold higher than the 15 min control. Processing for 15 min increased recovery levels of the 60 min control. Interval processing greatly increased yields. In sum, interval operation yielded ~2400 hepatocytes/mg, ~2.5-fold more than both the 60 min control and 15 min static conditions. (D) Endothelial cell and (E) leukocyte yields generally followed similar trends seen for epithelial cells. (F) Population distributions for each cell type that were liberated under the different processing conditions. Cell suspensions were enriched for leukocytes in comparison to the 60 min control. The interval conditions often contained significantly different representations of hepatocytes and leukocytes than static conditions. Error bars represent standard errors from at least three independent experiments. * indicates $p < 0.05$ and ** indicates $p < 0.01$ relative to the 60 min control. # indicates $p < .05$ and ## indicates $p < .01$ relative to the static digestion condition at the same digestion time.

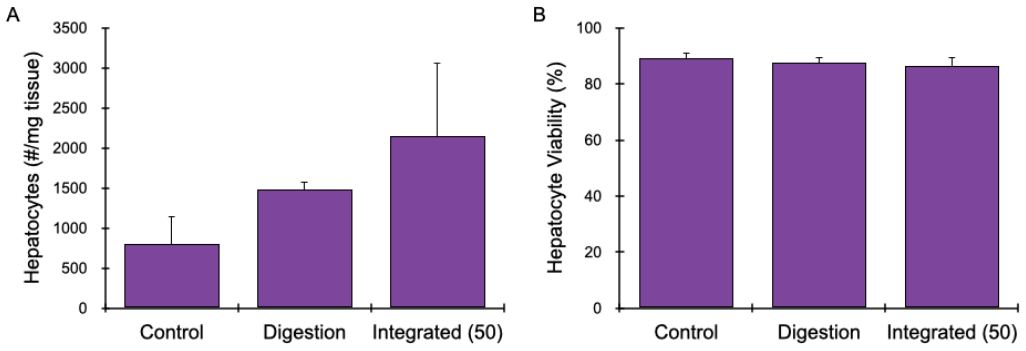

Figure 3.16: Optimization with murine liver. (A) After processing for 15 min with the digestion device, the modified dissociation/filtration device (only 50 μm filter) increased hepatocytes by 30% relative to the digestion device alone and by nearly 3-fold relative to the control. (B) Hepatocyte viability was >85% for all conditions. Error bars represent standard errors from at least three independent experiments.

dissociation/filtration device with only the 50 μm filter to avoid over processing and maximize hepatocyte recovery. Now using a 5 min device digestion, ~700 hepatocytes were recovered/mg liver tissue (Fig. 3.15C). This was 4-fold higher than the 15 min control and just slightly less than the 60 min control (~1000 hepatocytes/mg). Increasing digestion device processing time to 15 min only enhanced hepatocyte recovery by 40%, to the same level as the 60 min control. The most striking results were observed under the interval format. After only 1 min of digestion device processing, ~700 hepatocytes/mg tissue were recovered. Adding the 5 and 15 min intervals resulted in ~2400 hepatocytes/mg, for a ~2.5-fold enhancement relative to either the 60 min control or 15 min static condition. Hepatocyte viability remained at 90% for controls and most device conditions (Fig. 3.17A). The 5 min static and 1 min interval device conditions displayed higher viability, while the 15 min interval was lower at ~80%. Similar cell yield trends were observed for endothelial cells (Fig. 3.15D) and leukocytes (Fig. 3.15E), including significant cell recovery from the 1 min interval and enhanced overall cell numbers from the interval format. For endothelial cells, interval operation produced ~1.5-fold more than were produced by the 60 min control or 15 min static device cases. For leukocytes, static device operation produced >2.5-fold more cells

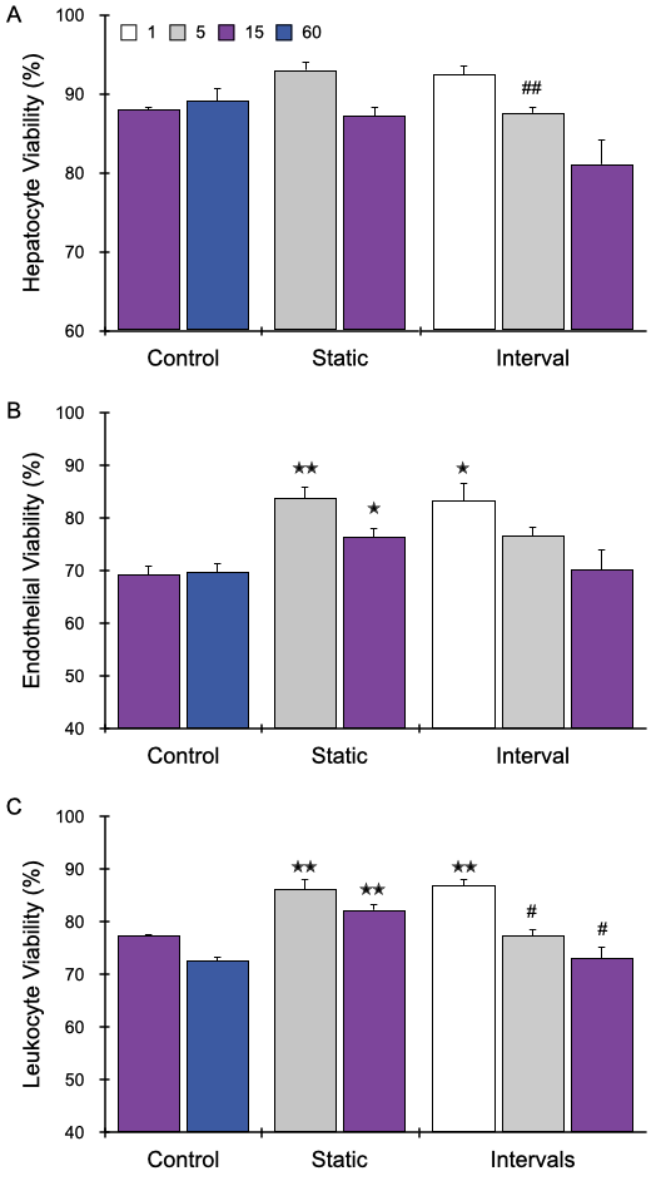

Figure 3.17: Murine liver viability. (A) Hepatocyte viability remained near 90% for most conditions. (B) Endothelial cell and (C) leukocyte viabilities were generally between ~70% and 85%. Error bars represent standard errors from at least three independent experiments. * indicates $p < 0.05$ and ** indicates $p < 0.01$ relative to the 60 min control. # indicates $p < .05$ and ## indicates $p < .01$ relative to the static digestion condition at the same digestion time.

than the 60 min control. Interval operation further enhanced recovery by 30% relative to the static conditions, or ~3.5-fold relative to the 60 min control. Given the strong performance of the device platform with leukocytes and their relative abundance in liver compared to kidney and tumor, cell suspensions were enriched for leukocytes in comparison to the 60 min control (Fig. 3.15F). This was particularly true for the static time points and

the 1 min interval. Interestingly, the three interval conditions contained very different representations of hepatocytes and leukocytes, suggesting that the choice of elution time could serve as a means to crudely select for one population over the other. Viability for endothelial cells and leukocytes ranged between ~70% and 85%, and variations for the different conditions closely mirrored hepatocytes (Figs. 3.17B and C). Taken together, the performance of the microfluidic processing platform with liver was quite unique relative to kidney and tumor. We believe that this caused by the fact that there is a balance that must to be maintained between the need to process/digest tissue that has yet to be broken down with the need to preserve cells that have already been liberated. For softer tissues like liver, this balance is shifted away from breakdown and towards preservation. In fact, the need to preserve hepatocytes is so strong that the temporal resolution of interval recovery should likely be increased, or ideally, be continuous. The interval recovery results suggest that liver endothelial cells and leukocytes are also sensitive to over-processing, but to a lesser degree. It is unclear whether this finding can be generalized to other tissues. Liver sinusoidal endothelial cells are highly specialized, with abundant fenestrae and no underlying basement membrane.[113] These properties could also make sinusoidal endothelial cells particularly sensitive to damage. For leukocytes, we did not distinguish between those that originated within the liver, which would predominantly be Kupffer cells, from those that came from blood that should be less sensitive to shear. Future studies directly assessing Kupffer cells, as well as hepatic stellate cells, would be of interest, particularly for complex culture liver models that utilize multiple liver cell types.[114–117]

3.2.6 Isolation of Cardiomyocytes from Murine Heart

Heart failure also ranks as one of the leading causes of drug withdrawal from the market, combining with liver failure to account for ~70% of withdrawal cases.[110,111] Thus, there is robust interest in developing heart-on-chip technologies for preclinical testing of drugs.[82,110,111,118,119] Cardiomyocytes have been shown to be highly sensitive to mechanical and enzymatic dissociation techniques.[120] In addition, they are disproportionately long in one direction, on the order of 100 μm and more.[121] For these experiments, murine heart was minced into ~1 mm^3 pieces and cardiomyocytes were detected based on Troponin T expression. Since this is an intracellular marker, we used a fixable viability dye, Zombie Violet, in place of 7-AAD. Given potential concerns about cardiomyocyte size and shape, we first tested the effect of filter pore size in the integrated dissociation/filtration device. After 15 min processing with the minced digestion device, sample was passed through the standard integrated dissociation/filtration device with 50 and 15 μm pore size filters or the modified version with only the 50 μm filter. Cell numbers and viability were similar to all

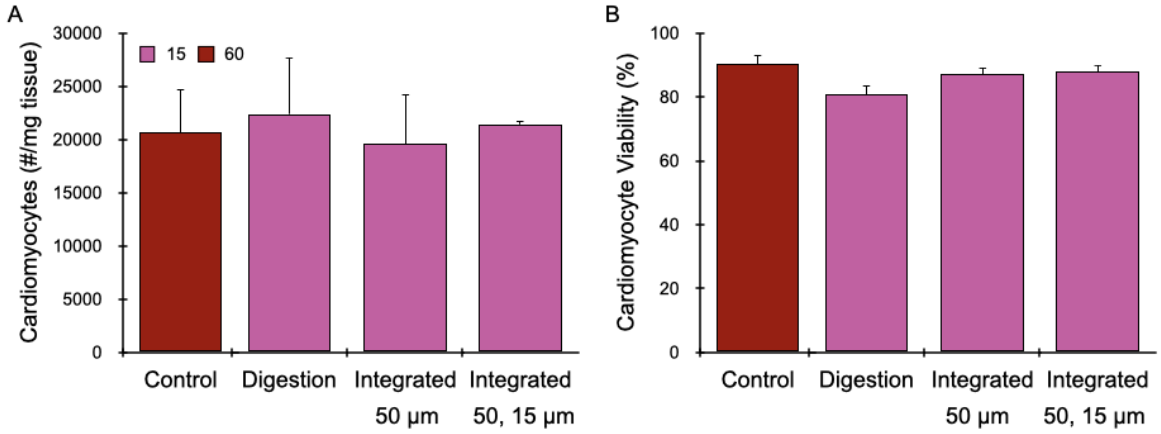

Figure 3.18: Device optimization with murine heart. (A) Cardiomyocyte cell yields and (B) cardiomyocyte viabilities were similar for all conditions. Error bars represent standard errors from at least three independent experiments.

conditions (Fig. 3.18), and thus we selected to use the standard version with both 50 and 15 μm filters for heart tissue.

Next we evaluated the full microfluidic platform at different digestion times. We again focused on shorter processing times due to the sensitivity of heart tissue to both mechanical and enzymatic dissociation.[120,122] After 5 min treatment with the digestion device, ~2000 cardiomyocytes were recovered per mg heart tissue (Fig. 3.19A). This was lower than both the 15 and 60 min controls, by ~half and one-third, respectively. Increasing digestion device processing to 15 min dramatically improved recovery to ~12,000 cells/mg, which was ~2-

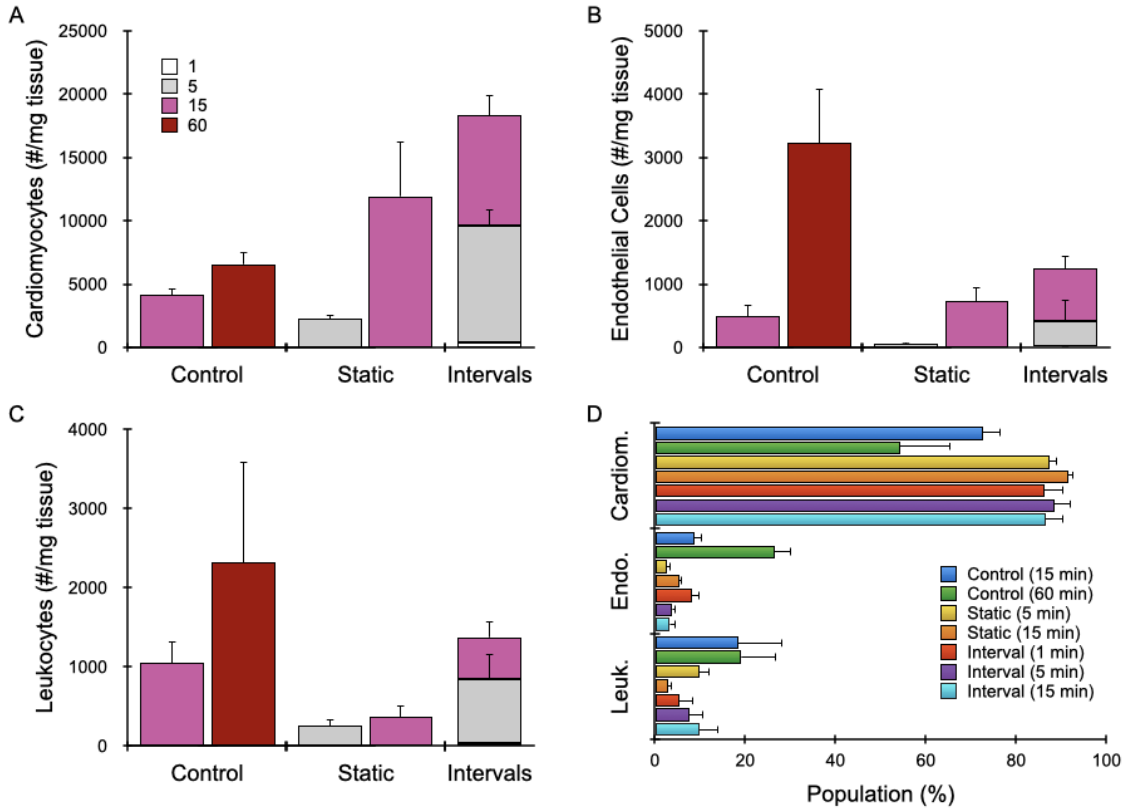

Figure 3.19: Single cell analysis of murine heart. Shorter processing times with the microfluidic platform were used due to heart tissue sensitivity to both mechanical and enzymatic dissociation. (A) 5 min treatment with the device platform yielded ~2000 cardiomyocytes/mg. 15 min treatment improved recovery to ~12,000 cells/mg, ~2-fold higher than the 60 min control. Interval format further increased recovery. (B) Endothelial cell yields were significantly lower than the 60 min control. Interval format did improve recovery, but the 60 min control remained higher by ~2-fold. (C) Leukocyte cell yields were also significantly lower than the 60 min control. Using the interval format, yields were still lower than the 60 min control by ~1.5-fold. (D) Population distributions for each cell type that were liberated under the different processing conditions. Device platform processing resulted in significant enrichment of cardiomyocytes. Error bars represent standard errors from at least three independent experiments.

fold higher than the 60 min control. As with kidney, the interval format further increased cardiomyocyte recovery to ~18,000 cells/mg. However, very few cardiomyocytes were obtained at the 1 min interval. Another difference for heart was that endothelial cell (Fig. 3.19B) and leukocyte (Fig. 3.19C) yields from the microfluidic device platform were significantly lower than the 60 min control. The interval format did improve recovery for

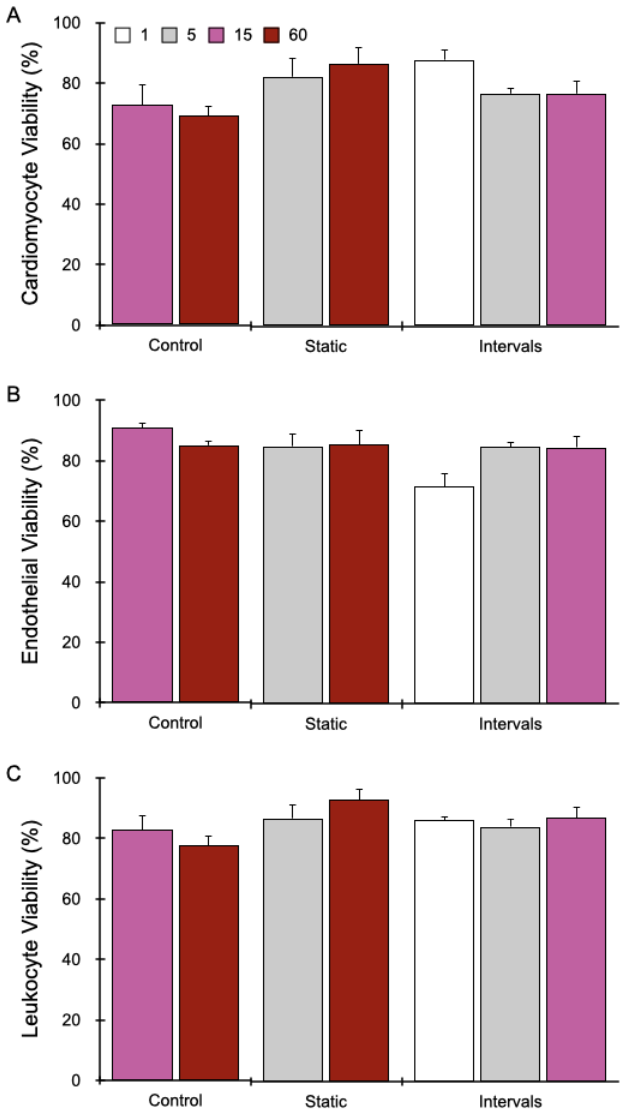

Figure 3.20: Murine heart cell viability. (A) Cardiomyocyte viability for device processed samples matched or exceeded controls. (B) Endothelial cell and (C) leukocyte viability was generally >80% for device and control conditions. Error bars represent standard errors from at least three independent experiments.

both cases, but the 60 min control remained higher by ~2-fold for endothelial cells and ~1.5-fold for leukocytes. Based on this differential recovery, device platform processing resulted in significant enrichment of cardiomyocytes (Fig. 3.19D). Viabilities for all three cells types were similar to controls (Fig. 3.20). However, the improved performance of intervals for all three cell types further indicates that cell damage could be a factor during extended periods of recirculation within the digestion device for tissues containing more sensitive cell types. As discussed previously, potential for cell damage could be minimized by reducing interval times to every few minutes, or even eliminated by introducing a separation scheme that diverts individual cells from the recirculation system into an elution stream or holding chamber. Nevertheless, the microfluidic platform as currently configured and operated in this study dramatically improved the recovery of single cells from diverse tissue types based on increased total cell yield, decreased processing time, and in some cases, both.

3.3 Materials and Methods

3.3.1 Device Fabrication

Microfluidic minced digestion and integrated dissociation/filter devices were fabricated by ALine, Inc. (Rancho Dominguez, CA). Briefly, fluidic channels, vias, and openings for membranes, luer ports, and hose barbs were etched into PMMA polyethylene terephthalate (PET) layers using a CO_2 laser. Nylon mesh membranes were purchased from Amazon Small Parts (15, and 50 μm pore sizes; Seattle, WA) as large sheets and were cut to size using the CO2 laser. Device layers, nylon mesh membranes, and hose barbs were then assembled, bonded using adhesive, and pressure laminated to form a single monolithic device.

3.3.2 Cell Aggregate and Murine Tissue Models

MCF-7 human breast cancer cells were obtained from ATCC (Manassas, VA) and cultured as recommended. Prior to experiments, confluent monolayers were briefly digested for 5 min with trypsin-EDTA, which released cells with a substantial number of aggregates. Cell suspensions were then centrifuged and resuspended in PBS containing 1% BSA (PBS+). Kidney, liver, and heart were harvested from freshly sacrificed BALB/c or C57B/6 mice (Jackson Laboratory, Bar Harbor, ME) that were determined to be waste from a research study approved by the University of California, Irvine's Institutional Animal Care and Use Committee (courtesy of Dr. Angela G. Fleischman). Mammary tumors were harvested from freshly sacrificed MMTV-PyMT mice (Jackson Laboratory, Bar Harbor, ME). For kidneys, a scalpel was used to prepare ~1 cm long x ~1 mm diameter strips of tissue, each containing histologically similar portions of the medulla and cortex. Each tissue strip was then further minced with a scalpel to ~1 mm^3 pieces. Liver, mammary tumor, and heart were uniformly minced with a scalpel to ~1 mm^3 pieces. Minced tissue samples were then weighed and either device-processed, or placed within microcentrifuge tubes, digested at 37°C in a shaking incubator under gentle agitation for 15, 30, or 60 min, and mechanically disaggregated by repeated pipetting and vortexing. 0.25% collagenase type I (Stemcell Technologies, Vancouver, BC) was used for both control and device-processed conditions. Finally, cell suspensions were treated with 100 Units of DNase I (Roche, Indianapolis, IN) for 10 min at 37°C and washed by centrifugation into PBS+. Cell suspensions were then ready for either gDNA quantification or flow cytometry analysis.

3.3.3 Minced Digestion Device Operation

Minced digestion devices were prepared by affixing 0.05" ID tubing (Saint-Gobain, Malvern, PA) to the device inlet and outlet hose barbs. 0.05" ID tubing was then connected to an Ismatec peristaltic pump (Cole-Parmer, Werheim, Germany) with 2.62 mm ID tubing (Saint-Gobain, Malvern, PA). Prior to experiments, devices and tubing were incubated with SuperBlock (PBS) blocking buffer (Thermo Fisher Scientific, Waltham, MA) at room temperature for 15 min to reduce non-specific binding of cells to channel walls and washed with PBS+. Minced pieces of tissue were loaded into the device tissue chamber through the luer inlet port. Devices and all tubing were then primed with 0.25% collagenase type I solution (StemCell Technologies, Vancouver, BC), and the luer port was closed off using a stopcock. The experimental setup consisting of the device, tubing, and peristaltic pump were then placed inside an incubator at 37 °C in order to maintain optimal enzymatic activity. The collagenase solution was recirculated through the device and tubing using the peristaltic pump at a flow rate of 10 or 20 mL/min for the specified time.

3.3.4 Quantification of DNA Recovered from Cell Suspensions

Purified genomic DNA (gDNA) content of digested kidney tissue suspensions were assessed following isolation using the QIAamp DNA Mini Kit (Qiagen, Germantown, MD), according to manufacturer instructions. gDNA content was quantified using a Nanodrop ND-1000 (Thermo Fisher, Waltham, MA). gDNA for device processed samples represents the cellular contents eluted from the device after operation, while gDNA for control samples represent the total amount of gDNA present in these samples.

3.3.5 Integration of Devices and Platform Operation

Following minced digestion device operation, tubing was connected from the outlet of the minced digestion device to the inlet of the integrated dissociation and filtration device. If recirculation through the dissociation device component was utilized, tubing was connected from the cross-flow outlet to the peristaltic pump, while the outlet of the integrated device was closed off with a stopcock. Fluid was then pumped through the devices at 10 mL/min. For final collection of the sample, or if only 1 pass through the dissociation device component was utilized, the cross-flow outlet was closed off with a stopcock, and sample was pumped at 10 mL/min and collected from the integrated device effluent outlet into a conical. Following all experiments, devices were washed with 2 mL PBS+ to flush out and collect any remaining cells. For time interval collections, following each PBS+ wash, all devices and tubing were reprimed with collagenase solution, and the outlet of the minced digestion device was reconnected to the peristaltic pump for continued recirculation through the device until the next interval collection.

3.3.6 Recirculation Studies

Integrated dissociation and filter devices were prepared by affixing 0.05" ID tubing to the device inlet and outlet hose barbs. 0.05" ID tubing from the integrated device inlet and cross-flow outlet were then connected to the 2.62 mm ID tubing of an Ismatec peristaltic pump. For this initial study, flow was recirculated only through the dissociation portion of the integrated device but not passed through the nylon filters of the filtration component for final sample collection in order to avoid confounding effects. To achieve this, the effluent outlet of the integrated device was closed off during pump operation using a stopcock. Prior to experiments, devices and peristaltic tubing were incubated with SuperBlock blocking

buffer at room temperature for 15 min to reduce non-specific binding of cells to channel walls and washed with PBS+. MCF-7 cells suspended in PBS+ were loaded into the tubing and recirculated through the dissociation component of the integrated device using a peristaltic pump set to a flow rate of 5, 10, or 20 mL/min. A condition where no device was used also included, in order to determine if there was any significant effect of the tube squeezing mechanism of the peristaltic pump mechanism. Following all experiments, devices were washed with 2 mL PBS+ to flush out and collect any remaining cells. Cell counts and viability were obtained both before and after recirculation using a Moxi Flow cytometer with type MF-S cassettes (Orfo, Hailey, ID) and propidium iodide staining.

3.3.7 Analysis of Cell Suspensions using Flow Cytometry

Cell suspensions were analyzed using the tissue-specific flow cytometry panels shown in Table 3.1. For initial studies with kidney tissue, cell suspensions were stained concurrently with 5 μg/mL anti-mouse CD45-AF488 (clone 30-F11, BioLegend, San Diego, CA), 7 μg/mL EpCAM-PE (clone G8.8, BioLegend, San Diego, CA), and 5 μg/mL TER119-AF647 (clone TER-119, BioLegend, San Diego, CA) monoclonal antibodies for 30 minutes. Samples were then washed twice using PBS+ by centrifugation, stained with 3.33 μg/mL viability dye 7-AAD (BD Biosciences, San Jose, CA) on ice for at least 10 minutes, and analyzed on a Novocyte 3000 Flow Cytometer (ACEA Biosciences, San Diego, CA). Flow cytometry data was compensated using single stained cell samples or compensation beads (Invitrogen, Waltham, MA). Gates encompassing the positive and negative subpopulations within each compensation sample were inputted into FlowJo (FlowJo, Ashland, OR) to automatically calculate the compensation matrix. A sequential gating scheme (Fig. 3.21) was used to identify live and dead single epithelial cells from leukocytes, red blood cells, non-cellular

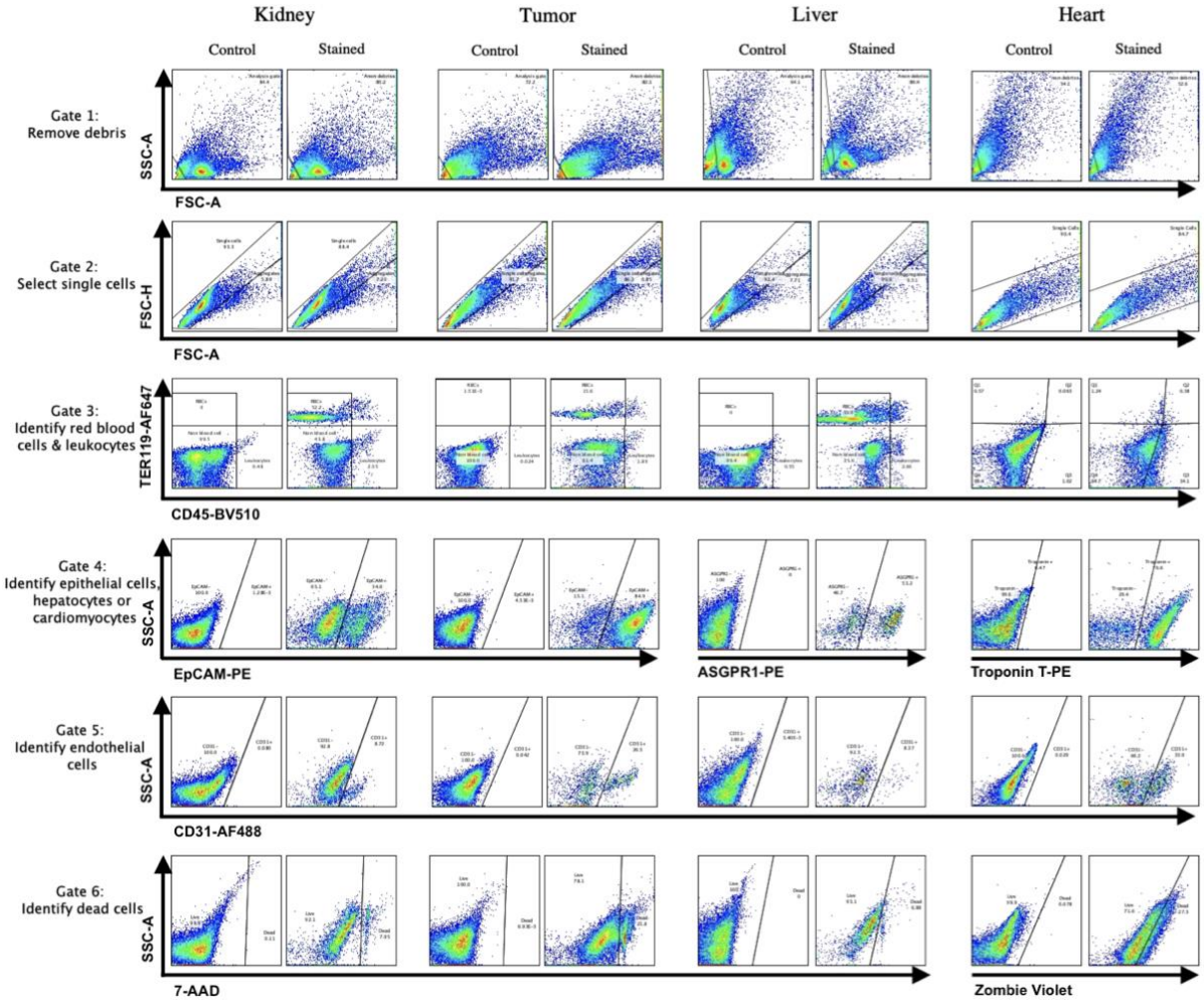

Figure 3.21: Flow cytometry gating scheme for final kidney, tumor, liver, and heart tissue staining panels. Cell suspensions obtained from digested murine kidney, mammary tumor, liver, and heart samples were stained with the fluorescent probes listed in Table 1 and analyzed using flow cytometry. Acquired data was compensated and assessed using a sequential gating scheme. Gate 1, based on FSC-A vs. SSC-A, was used to exclude debris near the origin. Gate 2 was was used to select single cells based on FSC-A vs. FSC-H. Gate 3 distinguished leukocytes based on CD45-BV510 positive signal and TER119-AF647 negative signal, and identified red blood cells based on TER119-AF647 positive signal and CD45-BV510 negative signal. Gate 4 was applied to the CD45-, TER119- cell subset to identify epithelial cells in kidney and tumor samples based on positive EpCAM-PE signal, to identify hepatocytes in liver samples based on positive ASGPR1-PE signal, and to identify cardiomyocytes in heart samples based on positive Troponin T-PE signal. Gate 5 was applied to the EpCAM- cell subset in kidney and tumor samples, to the ASGPR1- cell subset in liver tissue, and to the Troponin T- cell subset in heart tissue to identify endothelial cells based on positive CD31-AF488 signal. Finally, gate 6 was used to identify live cells in epithelial, hepatocyte, cardiomyocyte, leukocyte, and endothelial cell subsets based on negative 7-AAD signal. Appropriate isotype controls were initially used to assess nonspecific background staining, and appropriate fluorescence minus one (FMO) controls were used to determine positivity and set gates. Control samples were left unstained.

debris, and cellular aggregates. Signal positivity was determined using appropriate Fluorescence Minus One (FMO) controls. Final studies with kidney as well as all tumor and

liver studies used 12.5 μg/mL CD45-BV510 (clone 30-F11, BioLegend, San Diego, CA) in place of CD45-AF488 and also incorporated 8 μg/mL CD31-AF488 as a marker for endothelial cells. Liver demonstrations also replaced EpCAM-PE with 10 μg/mL ASGPR1-PE (clone 8D7, Santa Cruz Biotechnology, Dallas, TX), a known marker for hepatocytes. Heart demonstrations used 1:1000 dilution of Zombie Violet (Biolegend, San Diego, CA) instead of 7-AAD for viability, and replaced EpCAM-PE with 0.15 μg/mL Troponin T-PE (clone REA400, Milentyi Biotec, San Diego, CA), a known intracellular marker for cardiomyocytes.

3.3.8 Single Cell RNA Sequencing Studies

12 week old mice (male, C57BL/6 for kidney; female, MMTV-PyMT for mammary tumor, both Jackson Laboratory, Bar Harbor, ME) were euthanized by CO2 inhalation, and kidney or mammary tumor was dissected and minced into ~ mm^3 pieces. Tissue samples were digested with 0.25% type I collagenase, centrifuged (400xg, 5 min), treated with 100 Units of DNase I for 5 min at 37°C and washed by centrifugation into PBS+. Samples were then treated with RBC lysis buffer for 5 min on ice, so that RBCs did not interfere with results, and then centrifuged and resuspended in PBS+. Cells were stained with SytoxBlue (Life Technologies, Carlsbad, CA, USA) prior to FACS (FACSAria Fusion, BD Biosciences, Franklin Lakes, NJ) to remove dead cells and ambient RNA. Sorted live signgle cells (SytoxBlue-neg) were centrifuged and resuspended at a concentration of 1000 cells/μL. The 10x Chromium system (10x Genomics, Pleasanton, CA) was then used for droplet-enabled scRNA-seq. Oil, cells and reagents, and beads were loaded onto an eight-channel microfluidic chip. Lanes were loaded with ~10,000 cells from each of the samples, determined using an automated cell counter (Countess II, Invitrogen, Carlsbad, CA). Library generation for 10x Genomics v3 chemistry was then performed according to manufacturer's instructions. An Illumina

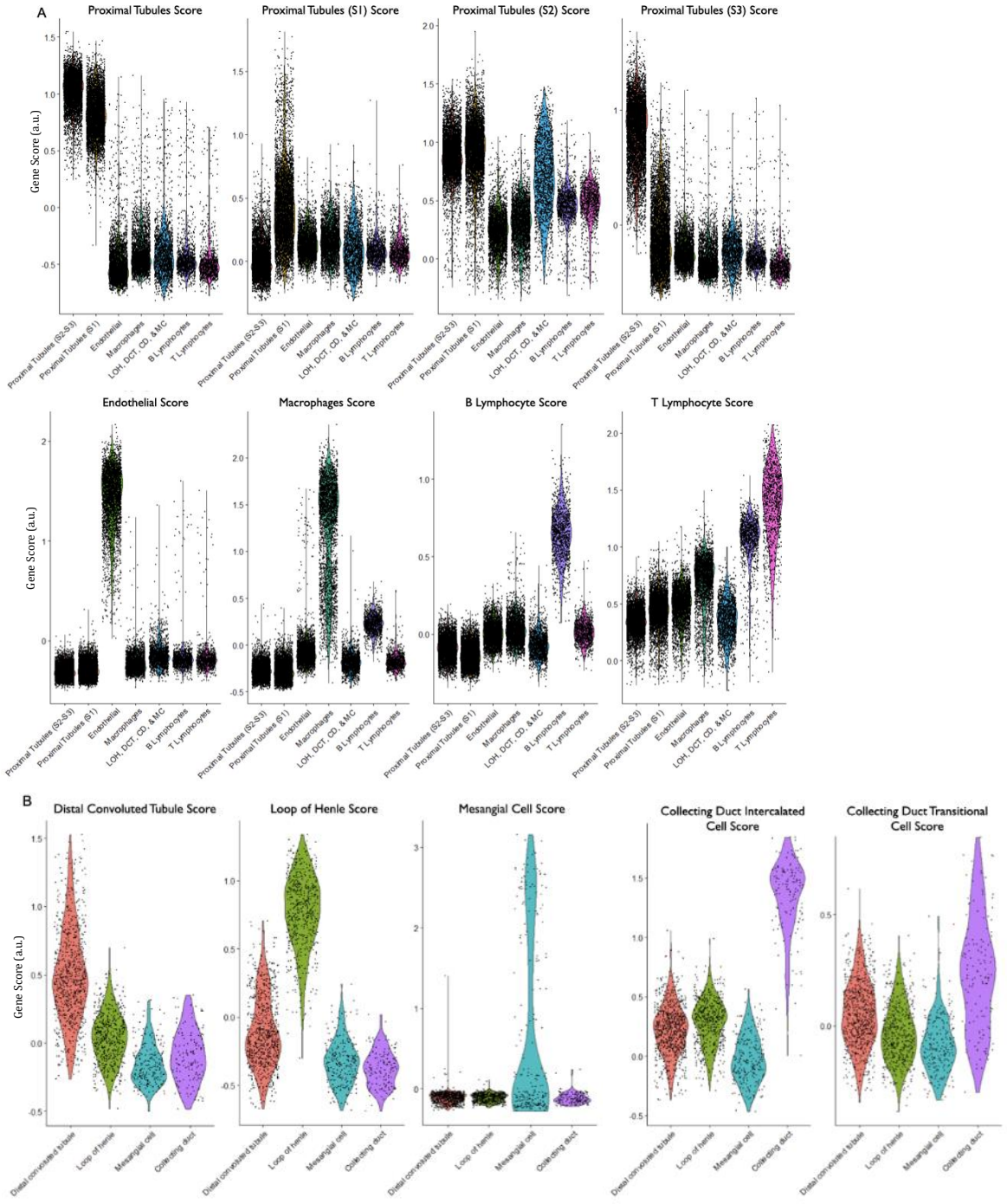

Figure 3.22: Gene scoring of kidney cell types. Cell scoring method was used to compare marker gene signatures from each of our main clusters (A) and subclusters (B).

NovaSeq 6000 platform (Illumina, San Diego, CA) was used to sequence the samples at a depth of ~60,000 reads/cell for kidney and ~45,000 reads/cell for mammary tumor. Genes

that were not detected in at least 3 cells were discarded from further analysis. Cells with low (<200) or high (>3000 for kidney; >4000 for mammary tumor) unique genes expressed were also discarded, as these potentially represent low quality or doublet cells, respectively.[63] Cells with high mitochondrial gene percentages were also discarded (>50% for kidney and >25% for mammary tumor), as these can also represent low quality or dying cells.[123] The Seurat pipeline was used for cluster identification in our datasets.[124] Principle component analysis (PCA) was performed using genes that are highly variable, and density clustering was then performed to identify groups in the data. Uniform Manifold Approximation and Projection (UMAP) plots were used to visualize these groupings. For kidney, cell clusters were annotated using two approaches. First, top differential genes in each cluster were examined to determine the cell type of the cluster based on expression of known marker genes (e.g. Kap, Napsa, and Slc27a2 for S2-S3 proximal tubules,[17] Gpx3 for S1 proximal tubules,[17] Emcn for endothelial cells,[84] Slc12a1 for loop of Henle,[63] Slc12a3 for distal convoluted tubule,[63] etc. Second, since a well-established atlas of murine kidney was available, we used a cell scoring method[5] to compare marker gene signatures from each of our clusters to published datasets[63,125] to confirm cluster annotations (Fig. 3.22). For tumor, cell clusters were annotated by examining top differential genes in each cluster to determine the cell type based on expression of known marker genes (e.g. Epcam for epithelial cells).

3.4 Conclusion

In this work, we have presented a novel digestion device that can process minced tissue specimens and is thus capable of being applied to the dissociation of many commonly used solid tissues. The device utilizes a luer input port, allowing it to be easily loaded with minced tissue pieces and immediately operated, without requiring any user assembly.

Operated as a stand alone device, we show that this device efficiently digests murine kidney, mammary tumor, liver, and heart specimens, even down to the single cell level. We then developed a complete microfluidic tissue processing platform by incorporating previously developed aggregate dissociation and filtration technologies that are able to process specimens spanning a wide range of size scales from solid tissue pieces down to single cells. We evaluated this platform using a diverse array of tissue types that exhibit a wide range of processing difficulty and that may each pose unique challenges at the molecular level. Incorporating these downstream technologies increased cell yields and also obviated the need for cell straining prior to single cell analyses. We also introduced a novel processing scheme: interval operation, which allowed us to investigate how single cells of key cell types are eluted as a function of digestion time. For tougher, more robust tissues like kidney and tumor, we found that results obtained using interval operation performed very similarly to static device operation, and outperformed time-matched controls by at least 2-fold for epithelial, endothelial, and leukocyte populations without compromising cell viability. Using single cell RNA sequencing of murine kidney, we show that all expected populations are found in control and device conditions, with more difficult to dissociate cell types like endothelial cells preferentially liberated earlier in the digestion. We also show that shortened interval operation minimizes cellular stress responses. Using scRNA-seq with tumor tissue, we found comparable population distributions across control and device conditions, and also found that stress responses are more similar across digestion lengths. Tumor specimens are increasingly analyzed using scRNA-seq to characterize the abundant heterogeneity, and this platform could provide much needed upstream tissue processing to feed into microfluidic scRNA-seq platforms. For more sensitive tissues like liver and heart,

we found that interval operation leads to higher cell recovery, likely by removing fragile cells from the platform earlier and preventing overprocessing. For liver hepatocytes and cardiomyocytes, there is an increasing need for their inclusion in organ-on-a-chip models for pharmacological studies, and this platform could integrate upstream of these models to provide the required cells. Based on interval processing results with liver and heart, and stress response scores with kidney and tumor, there is a need to decrease the temporal resolution of these processing intervals. Interval resolution would ideally reach continuous recovery, where cells are removed from the platform in real time as they are dissociated to the single cell level. In future work, we will explore utilizing inertial microfluidics to achieve this goal and also employing cold-active proteases to eliminate artifactual dissociation-induced stress responses. We also envision incorporating cell sorting and single cell analysis capabilities on-chip, to facilitate point-of-care single cell diagnostics, and expanding to processing other tissue types, with a focus on human tissues for clinical applications.

CHAPTER 4: Microfluidic Splenocyte Isolation for Single Cell Analysis

4.1 Introduction

The spleen is the most important organ for immune reactivity, involved in both innate and adaptive responses.[126] It's unique structure and organization allows it to meet its functions: removing blood-borne pathogens and cellular debris, and maintaining erythrocyte homeostasis.[127] The two main structures of the spleen, the red and white pulp, are composed of different cell types that carry out specific functions. The red pulp houses an abundance of macrophages, responsible for removing microorganisms, cellular debris, and aged erythrocytes. Red pulp also contains connective tissue that is home to large populations of monocytes and granulocytes. The white pulp, meanwhile, is a lymphoid tissue composed of distinct regions of B and T cells that are surrounded by the marginal zone, which contains subsets of macrophages, dendritic cells, and B cells. These white pulp cells are responsible for initiating adaptive immune responses.[126,127]

The various immune populations of the spleen represent significant cellular heterogeneity which is increasingly interrogated at single cell resolution.[13,128,129] To analyze the spleen at the single cell level, however, this organ must first be dissociated into a high-quality single cell suspension. Spleen dissociation methods are numerous and varied, with different methods employed as a matter of personal preference or for preferential dissociation of certain cell types.[130–132] Different dissociation kinetics for certain cell types may be present due to anatomical location within the spleen, and the adherence of these cell types. T cells, B cells, granulocytes, and some dendritic cell populations tend to be nonadherent. Other dendritic cell populations are weakly adherent, and macrophages and monocytes are known to be strongly adherent.[133] While these classifications are primarily

based on *in vitro* observations of plastic adherence, they also likely reflect the level of adherence *in vivo*. Commonly used spleen dissociation methods for liberating splenocytes include grinding on a strainer, rubbing between two frosted microscope slides, and digesting using proteolytic enzymes. These methods can all suffer from significant inter-operator variability, as well as from their time-consuming and manual intensive procedures. For users inexperienced in spleen processing techniques, intra-operator variability is also likely significant.

Here, we use a simple microfluidic device to either enzymatically or nonenzymatically dissociate splenocytes from minced murine spleen specimens. Previously, this device has been shown to efficiently digest murine kidney, mammary tumor, liver, and heart specimens enzymatically (see Chapter 3). In this work, we demonstrate that this device can dissociate all major spleen populations more effectively than traditional dissociation methods, under both enzymatic and nonenzymatic conditions. Using this device, manual processing steps are minimal, and thus operator variability is minimized. Spleen samples can also be easily sub-fractionated based on processing time. We show that either enzymatic or nonenzymatic conditions can be utilized with this device, and we find that certain cell types are more likely to be eluted in nonenzymatic conditions or during earlier enzymatic digestion periods. Thus, this device could be used as a crude method to select one population over another. Both enzymatic and nonenzymatic conditions generate improved cell yields relative to comparable controls, and these conditions can even be used sequentially with the same sample, if desired.

4.2 Results and Discussion

4.2.1 Characterizing Nonenzymatic Dissociation

We initially characterized our device performance using nonenzymatic conditions. Nonenzymatic methods for spleen dissociation are frequently utilized, as they require minimal processing time and effort, and preserve surface marker integrity.[16] For these initial studies, freshly dissected murine spleens were minced using a scalpel into ~1 mm^3 pieces, and then up to 30 mg of minced tissue was loaded into the device (Fig. 3.1D) through the luer port. For adult mice, this total amount of tissue represented roughly a quarter of a whole spleen. Next, tubing was connected to the inlet and outlet hose barbs, and the device and tubing were primed using PBS buffer containing 1% BSA (PBS+), to be used as the recirculating fluid. The luer input port was then sealed using a stopcock, and a peristaltic pump recirculated the buffer solution through the device. For a control, a frequently used nonenzymatic dissociation method was employed, where minced pieces of spleen were placed on a 100 μm pore cell stainer, a plunger from a syringe was used to break up the tissue on the cell strainer membrane, and then PBS+ buffer was used to wash the cells through the filter into a conical for collection.

We first explored device operation using a recirculation flow rate of 10 or 20 mL/min. 20 mL/min represents the flow rate used in previous work using this digestion device (see Chapter 3), while a 10 mL/min flow rate has been previously used for microfluidic dissociation and filtration devices with a variety of tissues.[39,97] Due to the anatomy of the spleen and the presence of many non- or weakly adherent cell types, we hypothesized that device operation with a lower flow rate may be sufficient to liberate many of these cells. To initially evaluate dissociated cellular suspensions, we designed a flow cytometry panel to

exclude red blood cells (RBCs) and identify leukocytes broadly based on CD45 positivity. Samples were processed using an interval operation scheme, in which devices were run for an initial time period, cell suspensions were eluted from the device, buffer was replaced, and device operation was resumed. For this initial experiment, 0.25, 1, and 3 minute intervals were chosen, in order to identify leukocytes that can quickly be liberated using nonenzymatic methods. Only 15 seconds of device processing at a 10 mL/min flow rate produced over 30,000 leukocytes/mg, equaling the total number of leukocytes dissociated using the strainer control (Fig. 4.1A). However, using a higher 20 mL/min flow rate for the same duration yielded over 60,000 leukocytes/mg tissue, doubling the number dissociated using the strainer control and equaling the total number freed by the sum of the 10 mL/min device intervals. After a total of 3 min of interval processing at 20 mL/min, 140,000 leukocytes/mg tissue were liberated using the device, over 2-fold more than the 10 mL/min interval sum, and over 4-fold more than the strainer control. Leukocyte viability for the strainer control was ~80%, while device-processed samples had ~90% viability using either flow rate (Fig. 4.1B). Since device operation at 20 mL/min flow rate increased leukocyte yields without compromising cell viability, this higher flow rate was utilized for device operation moving forward.

Next, we investigated how interval operation affects leukocyte recovery compared to a single, static device processing period. In previous work, we demonstrated that certain cell types can benefit from early cell removal from device processing, as significantly increased cell yields are observed when interval operation is used relative to static processing (see Chapter 3). For this experiment, 1, 2, and 3 min intervals were compared to a 3 min static operation, as well as to a strainer control. While the strainer control produced ~75,000

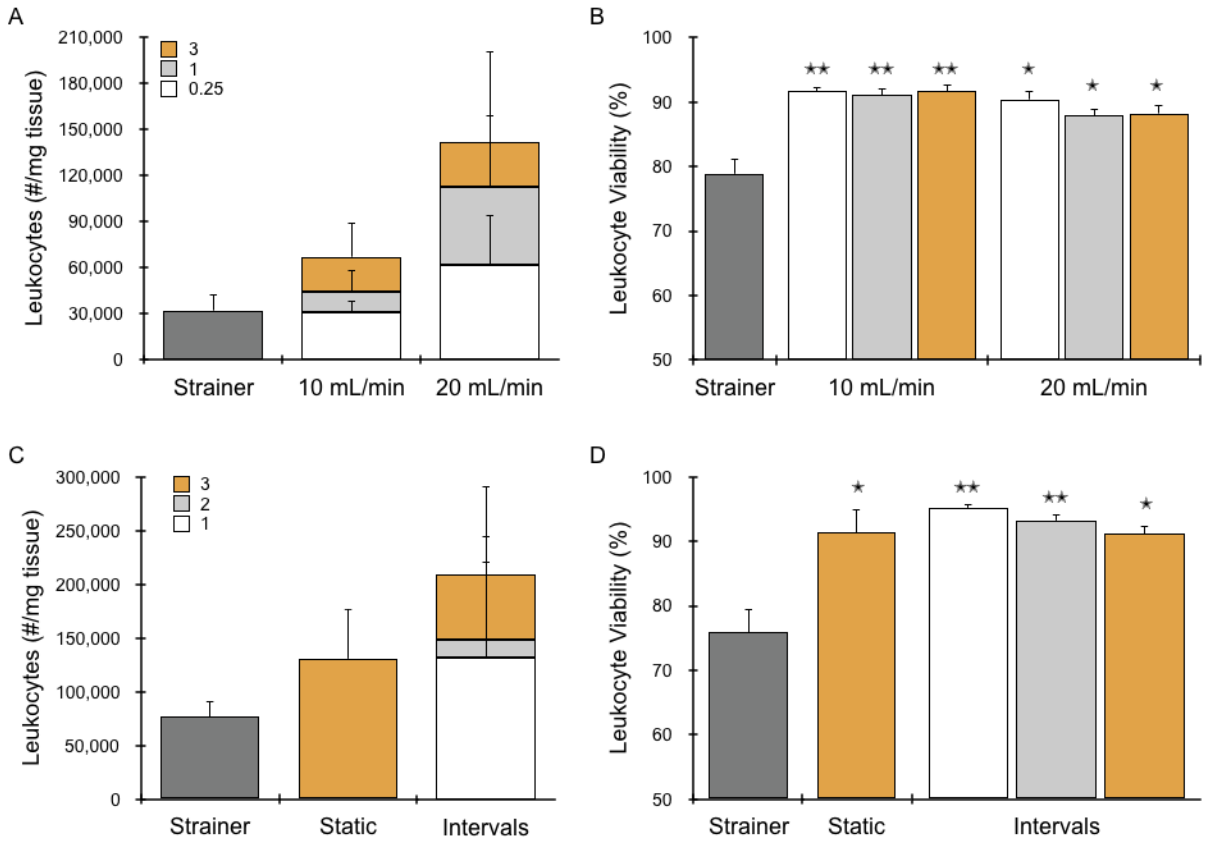

Figure 4.1: Characterizing nonenzymatic device operation. Microfluidic digestion device was loaded with minced spleen tissue and operated using PBS+ buffer as a recirculating fluid. Results were compared to a strainer control method, where spleen samples were grinded on a cell strainer membrane using a syringe plunger and then washed through and collected. (A-B) 10 and 20 mL/min device flow rates were explored using interval operation, where device was operated for an initial time period, cell suspensions were eluted from the device, buffer was replaced, and device operation was resumed. (A) The device interval sum using a 10 mL/min flow rate doubled leukocyte yields of the control, while the interval sum at 20 mL/min flow rate resulted in a 4-fold increase relative to the control. (B) Leukocyte viability for all device processed samples at either flow rate was ~90%, while the control had lower viability at ~80%. Since 20 mL/min flow rate increased cell yields and did not compromise viability, this flow rate was used moving forward. (C-D) Static and interval device operation were compared. (C) Both static and interval device processing yielded over 2-fold more leukocytes than the control (D) without compromising cell viability. Error bars represent standard errors from at least three independent experiments. * indicates $p < 0.05$ and ** indicated $p < .01$ relative to strainer control.

leukocytes/mg tissue, 3 min of device processing under static and interval formats yielded ~170,000 and 210,000 leukocytes/mg tissue, respectively, representing between 2- and 3-fold increases over the control (Fig. 4.1C). Promisingly, only 1 min of interval processing was required to dissociate substantially more cells than the strainer control. A modest increase in leukocyte recovery was observed in the interval sum compared to the static condition.

This may be due to the additional elution and re-priming steps involved in interval operation that would likely further agitate the tissue and could allow for improved liberation of cells. This difference, however, was not statistically significant. Leukocyte viability remained >90% for all static and interval device conditions, while viability for the strainer control was lower at ~75% (Fig. 4.1D). Taken together, these results suggest that nonenzymatic device operation can improve spleen dissociation relative to a standard strainer control method and that recirculation through the device does not cause significant harm to liberated leukocytes.

4.2.2 Characterizing Enzymatic Dissociation

Next, we characterized our device under enzymatic digestion conditions, and compared results to a standard, enzymatically digested control. For enzymatically digested controls, spleen specimens were similarly minced into ~1 mm^3 pieces, digested for 60 min with 0.25% type I collagenase at 37°C in a shaking incubator under gentle agitation, and mechanically disaggregated by repeated pipetting and vortexing. For device conditions, the same 0.25% type I collagenase was used as the recirculating fluid, in place of the PBS+ buffer used previously. For these experiments, the flow cytometry panel was expanded to include surface markers for dendritic cells as well as macrophages and monocytes (Table 4.1). Phenotypically, murine dendritic cells have been defined as $CD11c^{hi}$, MHC class II+ cells,[134–136] and macrophages and monocytes as $F4/80^{hi}$.[137] We chose to initially focus our analysis on these tissue-resident cell types as they can be more difficult to dissociate using purely mechanical methods and thus often require enzymatic digestion for improved dissociation.[130–132]

Enzymatic digestions in spleen dissociation protocols are frequently up to 1 hour in

length, so we chose 5, 15, and 60 min interval timepoints to allow comparison to a standard 60 min control digestion, as well as to investigate how cells are dissociated at earlier timepoints. Nonenzymatic device intervals using PBS+ buffer were also included for comparison and because longer nonenzymatic timepoints (past 3 min) had yet to be investigated.

Table 4.1: Primary flow cytometry panel

Cell Type	Surface Markers
Leukocytes	CD45+
Macrophage and monocytes	F4/80+
Dendritic cells	CD11c+, MHC class II+

After a 60 min collagenase digestion, controls generated ~160,000 leukocytes/mg tissue (Fig. 4.2A). In sum, the buffer device intervals yielded ~270,000 leukocytes/mg tissue, over 1.5-fold more than the control, suggesting that our microfluidic device can liberate at least as many immune cells compared to standard collagenase digestions but while using purely mechanical methods. For buffer intervals, most of the total cells dissociated were freed within 5 min of processing, equaling the number of cells recovered after a much longer 60 min control. Few cells were recovered after longer 15 and 60 min buffer intervals, suggesting that the effectiveness of nonenzymatic device processing plateaus after a short period of time. The collagenase interval sum produced a total of ~670,000 leukocytes/mg tissue, over 4-fold more than the collagenase control. Even a very brief 5 min collagenase interval yielded ~310,000 leukocytes/mg tissue, nearly 2-fold more than the control and comparable to the buffer interval sum. Taken together, these results suggest that collagenase device digestion is necessary for more complete liberation of leukocytes. Control leukocyte viability was 85%, and viability remained above 90% for all buffer and collagenase intervals

(Fig. 4.2B).

Dendritic cells, as expected, accounted for a small fraction of the total leukocytes

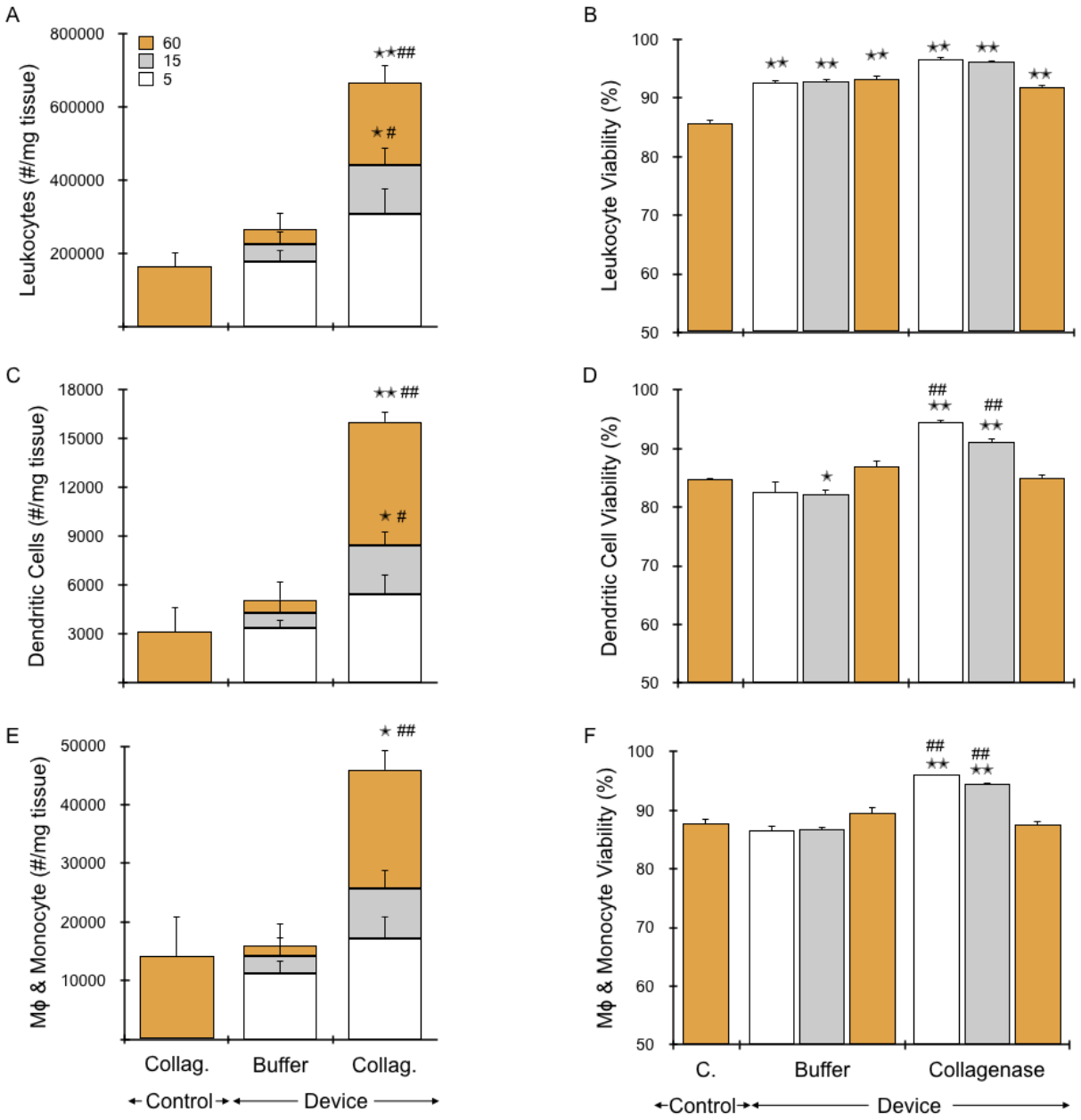

Figure 4.2: Comparing enzymatic and nonenzymatic device operation. Tissue samples were processed using devices under interval operation using either collagenase or buffer as the recirculating fluid. Results were compared to a collagenase control method, where samples were minced, digested with collagenase, and repeatedly pipette and vortexed. For (A-B) leukocytes, (C-D) dendritic cells, and (E-F) macrophages and monocytes, the buffer interval sum yielded at least as many cells as the collagenase control, while the collagenase interval sum yielded at least 3-fold more cells than the control. Viability for device conditions were generally comparable or greater than that of the control for all investigated cell types. Error bars represent standard errors from at least three independent experiments. * indicates $p < 0.05$ and ** indicates $p < .01$ relative to collagenase control. # indicates $p < .05$ and ## indicates $p < .01$ relative to time-matched buffer interval condition.

recovered, with the 60 min collagenase control generating 3,000 dendritic cells/mg tissue (Fig. 4.2C). Trends for buffer and collagenase intervals mirrored those seen with leukocytes; the collagenase intervals totaled 16,000 dendritic cells/mg tissue, over 5-fold more than the control and over 3-fold more than the buffer interval sum. Viability remained between 80 and 95% for all conditions (Fig. 4.2D). The 5 min collagenase interval had the highest viability at ~95%, which decreased slightly with increased interval processing to 85% for the 60 min collagenase interval.

For macrophage and monocytes, both the 60 min collagenase control and the buffer interval sum produced ~15,000 cells/mg tissue (Fig. 4.2E). The 5 min collagenase interval, by itself, matched the yields of the collagenase control and buffer interval sum, while the collagenase interval sum totaled 3-fold more cells. Viability remained >85% for all control and device conditions (Fig 4.2F).

While interval collagenase digestions were utilized in this experiment, it is noted that static collagenase device digestions perform very similarly to the interval sums in terms of cell recovery and viability for all investigated cell types (Fig. 4.3). Interestingly, in both experiments (Figs. 4.2 & 4.3) viability for all 3 cell types decreased modestly with increased digestion time for collagenase interval conditions. Continued recirculation through the device could be a concern in terms of cell damage for either interval or static formats. However, if significant recirculation-induced damage were occurring, we would expect cell viabilities for the 60 min static condition to be lower than the 60 min interval, and this is not observed. Overall, the comparable cell yield and viability results between static and interval operation conditions suggest that interval operation is not necessary for improved spleen dissociation efficiency, and static operation could be employed in experiments where a

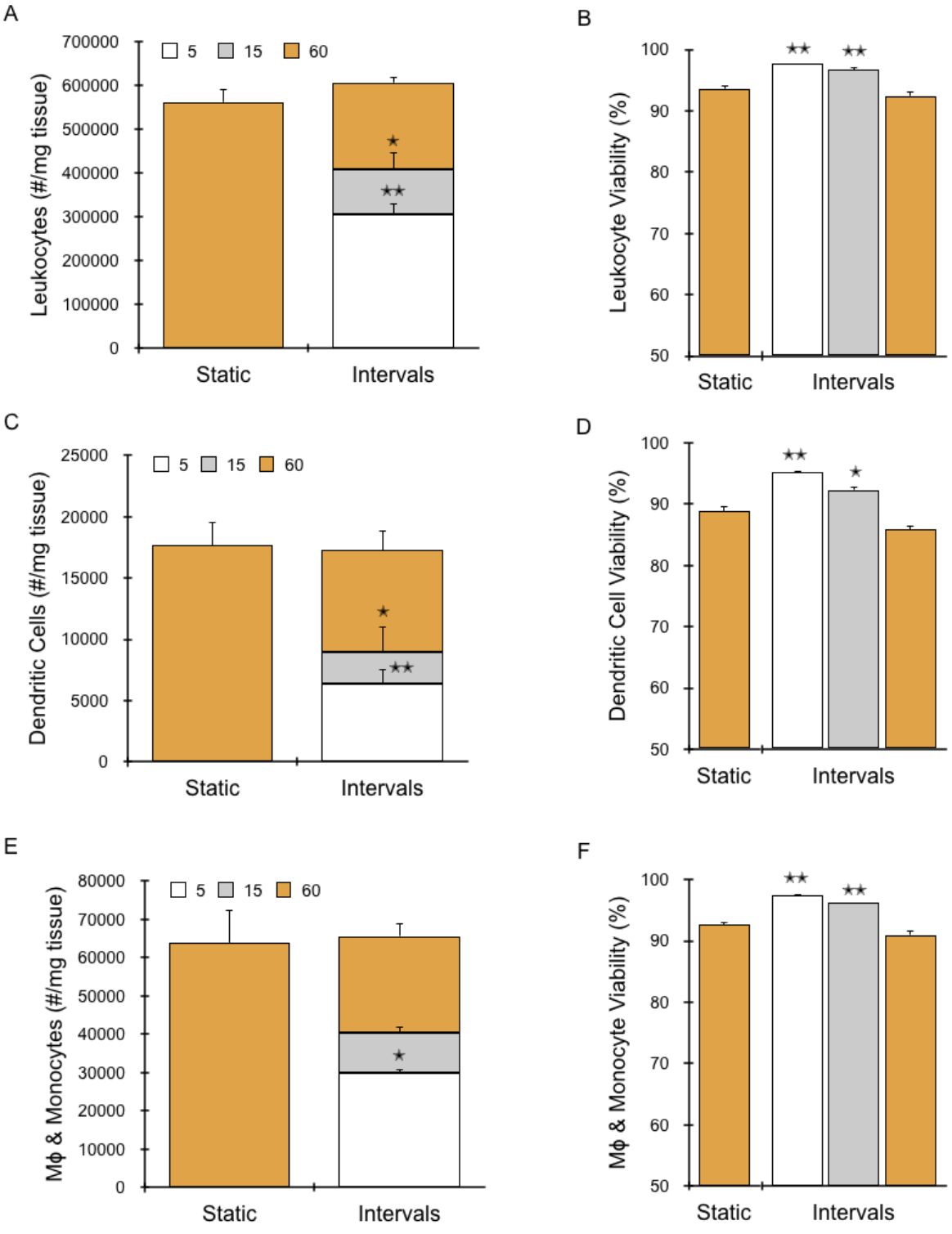

Figure 4.3: Static and interval operation modes under enzymatic conditions. (A-B) Leukocyte, (C-D) dendritic cell, and (E-F) macrophage and monocyte cell yields and viability were comparable between static and interval sum conditions. Error bars represent standard errors from at least three independent experiments. * indicates $p < 0.05$ and ** indicated $p < .01$ relative to static device control.

simpler operation scheme is desired.

4.2.3 Final Dissociation Protocol

Next, we developed a final device operational scheme combining nonenzymatic and enzymatic intervals. To do so, we first operated the device for a 2 min buffer interval. This interval was meant to liberate as many nonadherent or loosely adherent cell types as possible nonenzymatically, in order to conserve costly enzymatic solution and preserve cell surface marker integrity.[16] After eluting the buffer interval, we switched to a collagenase recirculating fluid (5, 15, 60 min intervals) to free cells that are more difficult to dissociate. To assess spleen dissociation more comprehensively, we designed a secondary flow cytometry panel to allow us to study the dissociation kinetics of the other dominant cell types in the spleen. Using standard cell surface markers,[138] we included antibody-fluorophores specific for CD3 to identify T cells, CD8 to identify cytotoxic T cells, CD19 to identify B cells, and CD11b and Ly6G to identify granulocytes, while retaining TER-119 for excluding red blood cells and 7-AAD dye for determining cell viability (Table 4.2).

Table 4.2: Secondary flow cytometry panel

Cell Type	Surface Markers
T cells	CD3+
Cytotoxic T cells	CD8a+
Other T cells (helper T)	CD3+, CD8a-
B cells	CD19+
Granulocytes	CD11b+, Ly6G+

For this study, we included both nonenzymatic (strainer method) and enzymatic (60 min collagenase) controls for comparison, and both primary and secondary flow cytometry panels were utilized. Analyzed using the primary flow cytometry panel, the 60 min

collagenase control produced ~230,000 leukocytes/mg tissue, a third more than the strainer control (Fig. 4.4A). The 2 min buffer interval successfully released more leukocytes than the strainer control, again confirming the ability of this device to effectively liberate cells nonenzymatically. It is noted that the 2 min buffer interval did not dissociate cells as well relative to the collagenase control in this experiment as the first buffer interval in Fig. 4.2A, possibly since this interval was shorter (2 min) compared to the 5 min interval used previously. The 2 min buffer interval also performed more similarly relative to the strainer control than seen previously (Fig. 4.1C), although variability in the previous data was high. Overall cell counts were also higher in this study, which could be due to differences in mouse strain, age, gender, or general health used in the experiments.[101,139,140] Following the 2 min buffer interval, 5, 15, and 60 min collagenase intervals were employed. After the 5 min collagenase interval, the device interval sum totaled as many cells as the much longer 60 min collagenase control, again demonstrating the ability of this device to liberate cells more efficiently than standard methods, with greatly reduced processing time. After the final, 60 min collagenase interval collection, the device interval sum yielded ~460,000 leukocytes/mg tissue, ~2-fold more than the collagenase control and ~2.5-fold more than the strainer control. Trends for dendritic cells again followed those seen with leukocytes, with lower overall cell numbers. The device interval sum produced ~13,500 cells/mg tissue, 2- and 4.5-fold more than the collagenase and strainer controls, respectively (Fig. 4.4B). For macrophages and monocytes, the device interval sum generated ~30,000 cells/mg tissue (Fig. 4.4C). This represents a statistically significant 2-fold increase compared to the strainer control. Interestingly, while the device interval sum also yielded 1.5-fold more cells than the collagenase control, this result was not significant, and represents a less dramatic

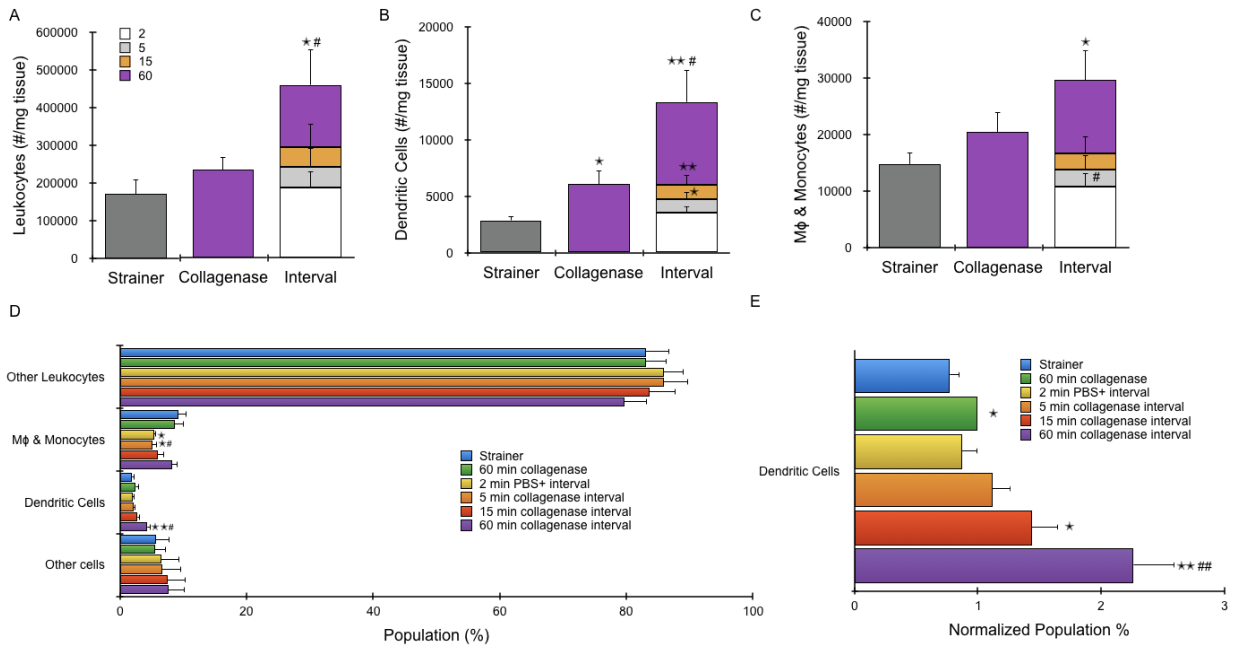

Figure 4.4: Final protocol characterization using primary flow cytometry panel. Final device operation protocol consisted of a 2 min buffer interval followed by 5, 15, and 60 min collagenase intervals. Results were compared to strainer and 60 min collagenase controls. In sum, device processing with a combination of both enzymatic and nonenzymatic intervals yielded greater numbers of (A) leukocytes, (B) dendritic cells, and (C) macrophages and monocytes than both strainer and collagenase controls. (D) Population percentages for each cell type that were liberated under the different processing conditions. Dendritic cell and macrophage and monocyte population percentages increased with longer collagenase interval digestions. (E) Dendritic cell population percentages were normalized to the 60 min collagenase control, and were at least 2-fold higher in the 60 min collagenase interval compared to both strainer and collagenase controls. Error bars represent standard errors from at least three independent experiments. * indicates $p < 0.05$ and ** indicates $p < .01$ relative to strainer control. # indicates $p < .05$ and ## indicates $p < .01$ relative to collagenase control.

improvement compared to Fig. 4.2E. This may be due to aggregates of macrophages or monocytes that were eluted during the 2 min buffer interval that could potentially have been broken down more effectively into single cells with enzymatic digestion. For monocytes specifically, it has also been shown that clusters of ~20-50 cells are aggregated in the red pulp,[141] which contains collagen cords, so superior dissociation of these aggregates could increase yields. If these cells were eluted during the buffer interval but remained aggregated, they could have been lost during aggregate exclusion in flow cytometry gating.

Population percentages of macrophages and monocytes, dendritic cells, other CD45+ leukocytes (non-macrophage and monocyte, non-dendritic cells), and other cells, as

determined by flow cytometry, are shown in Fig. 4.4D. RBCs, aggregates, and debris were excluded from this analysis. These population percentages match those seen in the literature,[140,142] suggesting that device processing generally dissociates spleen in the expected cellular proportions, although with greater overall cell numbers. For both dendritic cells and macrophages and monocytes, the relative percentage of these cell populations generally increased with longer collagenase intervals compared to the buffer interval. In Figure 4E, population percentages of dendritic cells have been normalized to the 60 min collagenase control. For the 60 min collagenase interval, the normalized population percentage of dendritic cells is over 2-fold higher compared to the 2 min buffer interval. This result suggest that the choice of elution time could serve as a means to crudely select for one population over the other.

For both strainer and collagenase controls, viability for all cell types were generally ~75-85% (Fig. 4.5). Viability for device conditions tended to be higher at ~85-95%, again with modest viability decreases as collagenase interval processing time increased.

Using the secondary flow cytometry panel, B cells (CD19+), cytotoxic T cells (CD3+, CD8+), granulocytes (CD11b+, Ly6G+), and other T (CD3+, CD8-) cells were quantified. For B cells, the device interval sum produced 260,000 cells/mg tissue, ~2-fold more than the collagenase control and ~4-fold more than the strainer control (Fig. 4.6A). For granulocytes, the strainer control yielded ~1,000 cells/mg tissue, while the collagenase control and device interval sum generated 4- and 5-fold more cells, respectively (Fig. 4.6B). Trends for cytotoxic and other T cells were similar to B cell results, although with lower cell counts and with the strainer and collagenase controls performing more similarly to one another. The 2 min buffer interval produced as many cytotoxic T cells as the collagenase control, and the interval sum

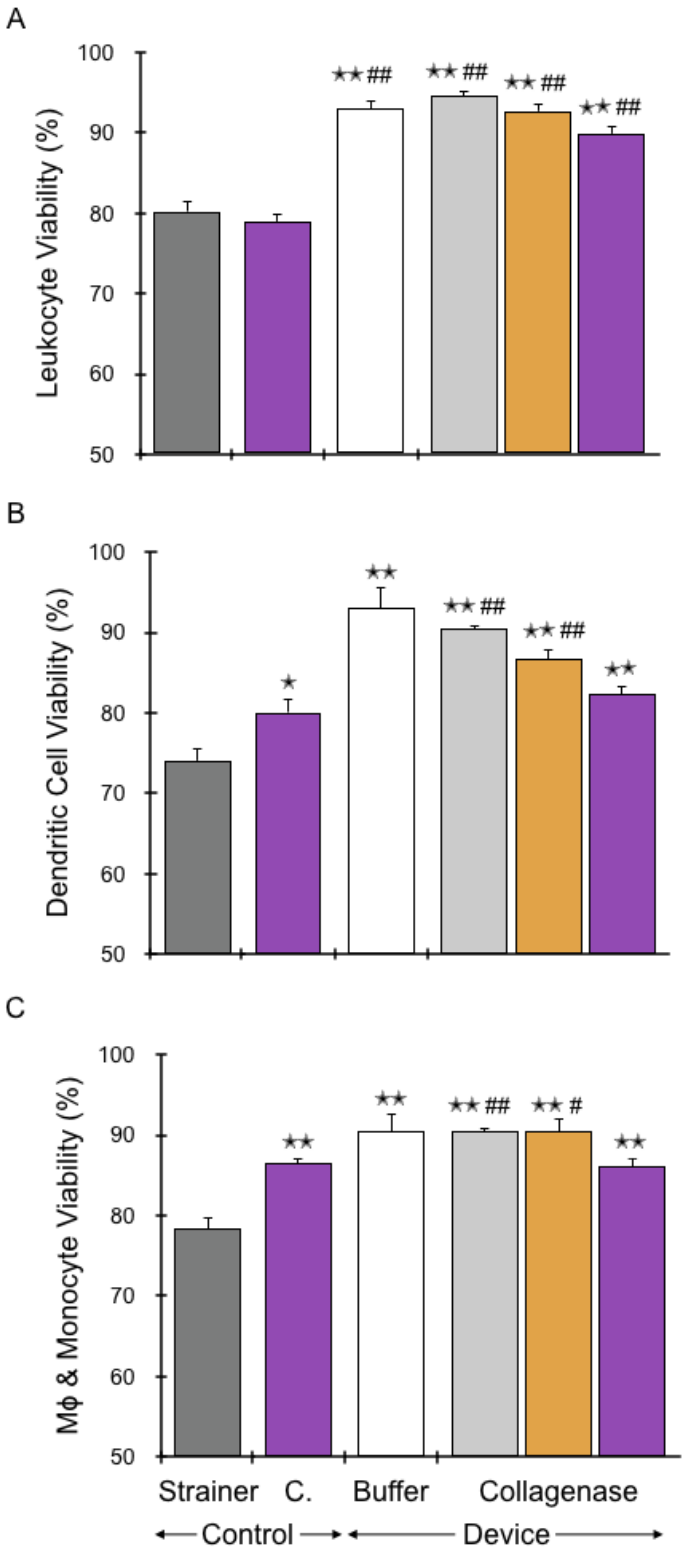

Figure 4.5: Cell viabilities from primary flow cytometry panel. Viability for (A) leukocytes, (B) dendritic cells, and (C) macrophages and monocytes were ~70-85% in controls and ~85-95% in device conditions. Error bars represent standard errors from at least three independent experiments. * indicates $p < 0.05$ and ** indicates $p < .01$ relative to strainer control. # indicates $p < .05$ and ## indicates $p < .01$ relative to collagenase control.

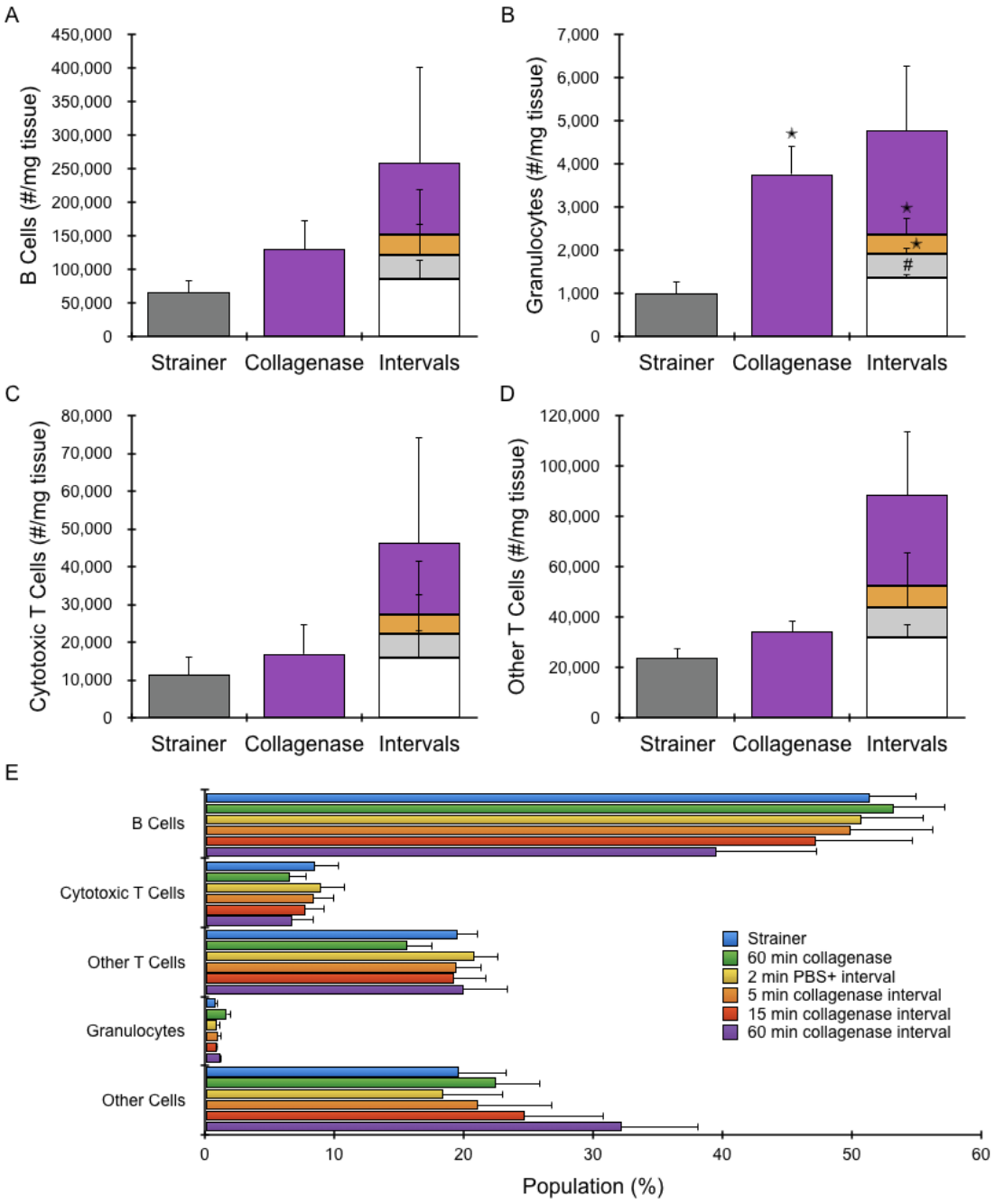

Figure 4.6: Final protocol characterization using secondary flow cytometry panel. In sum, device processing with a combination of both enzymatic and nonenzymatic intervals yielded greater numbers of (A) B cells, (B) granulocytes, (C) cytotoxic T cells, and (D) other T cells than both strainer and collagenase controls. (E) Population percentages for each cell type that were liberated under the different processing conditions. B cell, cytotoxic T cell, and other T cell population percentages generally decreased with longer collagenase interval digestions. Error bars represent standard errors from at least three independent experiments. * indicates $p < 0.05$ and ** indicates $p < .01$ relative to strainer control. # indicates $p < .05$ and ## indicates $p < .01$ relative to collagenase control.

yielded 46,000 cells/mg tissue, representing about 3- and 4-fold more cells than the strainer and collagenase controls, respectively (Fig. 4.6C). The recovery of other T cells, which we would expect to be predominantly helper T cells, very closely mirrored cytotoxic T cell recovery. The 2 min buffer interval again generated as many cells as the collagenase control (~35,000 cells/mg tissue), and the interval sum produced 90,000 cells/mg tissue, nearly 3- and 4-fold more than the strainer and collagenase controls, respectively (Fig. 4.6D).

Comparing relative population percentages in the device intervals, B cells, cytotoxic T cells, and other T cells are at their highest relative population percentage in the 2 min buffer interval and generally decrease in population percentage as device processing time increases (Fig. 4.6E). As these cell types are generally nonadherent and housed in the white pulp, they may be more likely to be mechanically dissociated in the buffer interval or early in the collagenase intervals. This is supported by the fact that the strainer control results tend to more closely match the collagenase control for these cell types; this similarity suggests that collagenase digestion does not particularly help with dissociating these populations.

Viability for all device intervals was >90%, while viability for strainer and collagenase controls were generally lower (Fig. 4.7). For strainer controls, this reduced viability was most noticeable for granulocyte (77%) and other T cell (80%) populations. Collagenase controls had the most apparent decreases in viability for cytotoxic T cells (68%) and other T cells (80%). Taken together with the cell recovery data, these results suggest that both strainer and control methods are less efficient at liberating a variety of immune cell types in the spleen, and sometimes adversely impact cell viability.

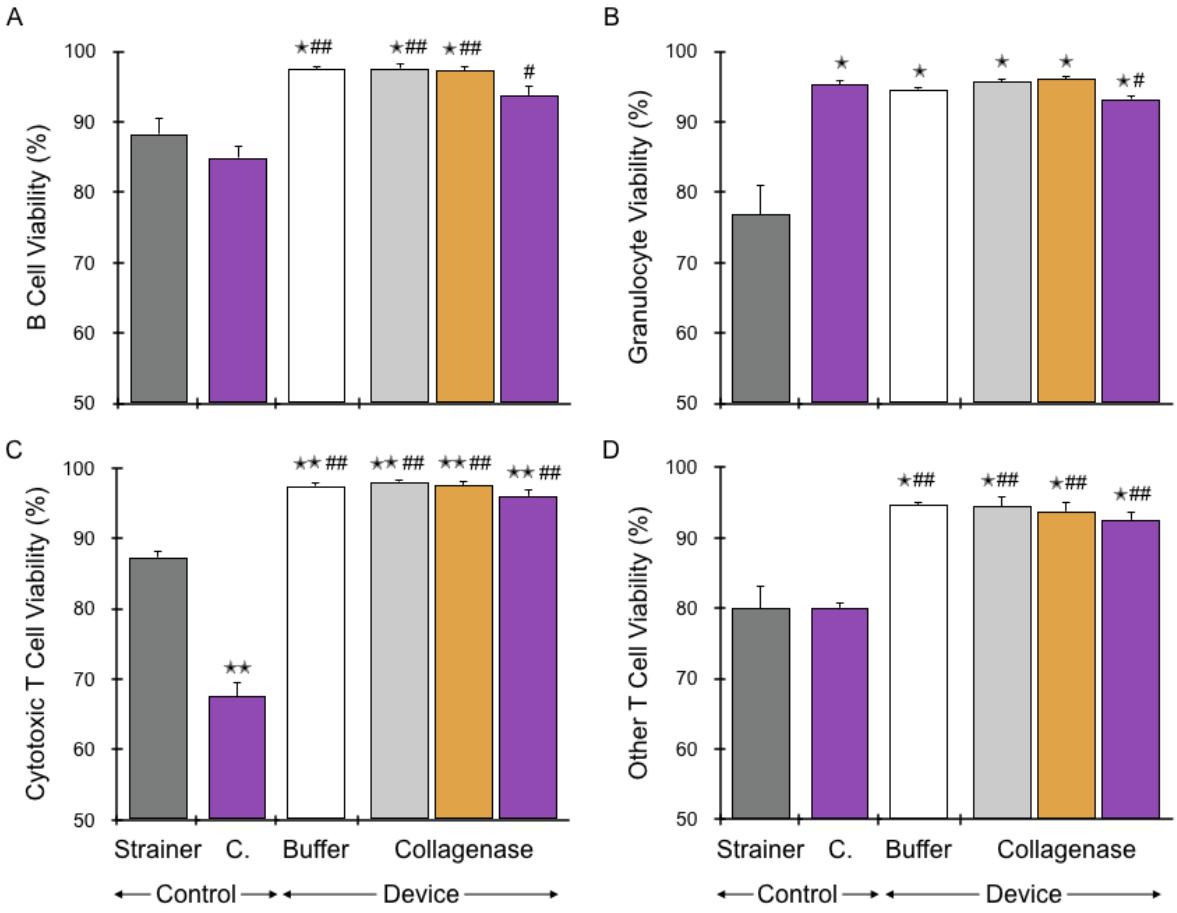

Figure 4.7: Cell viabilities from secondary flow cytometry panel. Viability for (A) B cells, (B) granulocytes, (C) cytotoxic T cells, and (D) other T cells was >90% for all device intervals which matched or exceeded viability of the strainer and collagenase controls. * indicates $p < 0.05$ and ** indicates $p < .01$ relative to strainer control. # indicates $p < .05$ and ## indicates $p < .01$ relative to collagenase control.

4.3 Materials & Methods

4.3.1 Device Operation

Device operation closely follows methods previously described (REF PLATFORM). Briefly, minced digestion devices were prepared by affixing 0.05" ID tubing (Saint-Gobain, Malvern, PA) to the device inlet and outlet hose barbs. 0.05" ID tubing was then connected to an Ismatec peristaltic pump (Cole-Parmer, Werheim, Germany) with 2.62 mm ID tubing (Saint-Gobern, Malvern, PA). Prior to experiments, devices and tubing were incubated with SuperBlock (PBS) blocking buffer (Thermo Fisher Scientific, Waltham, MA) at room

temperature for 15 min to reduce non-specific binding of cells to channel walls and washed with PBS+. Minced pieces of murine spleen tissue were loaded into the device tissue chamber through the luer inlet port. Devices and all tubing were then primed with 0.25% collagenase type I solution (Stemcell Technologies, Vancouver, BC), and the luer port was closed off using a stopcock. The experimental setup consisting of the device, tubing, and peristaltic pump were then placed inside an incubator at 37 °C in order to maintain optimal enzymatic activity. The collagenase solution was recirculated through the device and tubing using the peristaltic pump at a flow rate of 10 or 20 mL/min for the specified time.

4.3.2. Murine Spleen Model

Tissue preparation closely follows methods previously described.[39] Briefly, spleens were resected from freshly sacrificed wildtype C57B/6 or BALB/c mice (Jackson Laboratory, Bar Harbor, ME) that were determined to be waste from a research study approved by the University of California, Irvine's Institutional Animal Care and Use Committee (courtesy of Dr. Angela G. Fleischman). Spleens were then uniformly minced with a scalpel to ~1 mm^3 pieces and weighed. Device samples were then processed using the minced digestion device with a peristaltic pump recirculating either PBS+1% BSA (PBS+) buffer solution or 0.25% type I collagenase solution through the devices. For strainer controls, minced pieces of spleen were placed on a standard 100 μm cell strainer atop a 50 mL conical. The end of a 10 mL syringe plunger was then used to massage the tissue through the strainer. PBS+ was repeatedly flushed through the strainer to wash through and cells remaining on the strainer membrane. For collagenase controls, minced pieces of spleen were place in microcentrifuge tubes, digested at 37°C in a shaking incubator under gentle agitation for 60 min, and mechanically disaggregated by repeated pipetting and vortexing. 0.25% collagenase type I

was used for both control and device-processed conditions. Finally, all cell suspensions were treated with 100 Units of DNase I (Roche, Indianapolis, IN) for 10 min at 37°C and washed by centrifugation into PBS+. Cell suspensions were then ready for flow cytometry staining and analysis.

4.3.3 Flow Cytometry

Cell suspensions were aliquoted into representative samples and analyzed using the tissue-specific flow cytometry panels shown in Tables 4.1 & 4.2. For initial studies, cell suspensions were first treated with 10 ug/mL TruStain FcX (anti-mouse CD16/32 clone 93) Antibody (BioLegend, San Diego, CA) on ice for 10 min to block FC receptors and prevent nonspecific cell staining. Cell suspensions were then stained, without washing, concurrently with 5 μg/mL anti-mouse CD45-AF488 (clone 30-F11, BioLegend, San Diego, CA) and 5 μg/mL TER119-AF647 (clone TER-119, BioLegend, San Diego, CA) monoclonal antibodies for 30 minutes at 4°C in the dark. In later experiments, cellular suspensions were also stained with 10 ug/mL F4/80-PE (clone BM8), 2.5 ug/mL CD11c-FITC (clone N418), and 2.5 ug/mL MHC class II-APC/Cy7 (clone M5/114.15.2) (all from BioLegend, San Diego, CA). For the secondary panel, a representative aliquot was instead stained concurrently with 2.5 ug/mL CD3-BV421 (clone 17A2), 5 ug/mL Ly6G-BV510 (clone 1A8), 2.5 ug/mL CD8a-AF488 (clone 53-6.7), 2.5 ug/mL CD19-PE (clone 6D5), 5 μg/mL TER119-AF647 (clone TER-119), 2.5 ug/mL CD11b-APY/Cy7 101226 (clone M1/70) (all from BioLegend, San Diego, CA). For all panels, samples were then washed using PBS+ by centrifugation (500 x g, 5 min), stained with 3.33 μg/mL viability dye 7-AAD (BD Biosciences, San Jose, CA) on ice for at least 10 minutes, and analyzed on a Novocyte 3000 Flow Cytometer (ACEA Biosciences, San Diego, CA). Flow cytometry data was compensated using single stained cell samples or

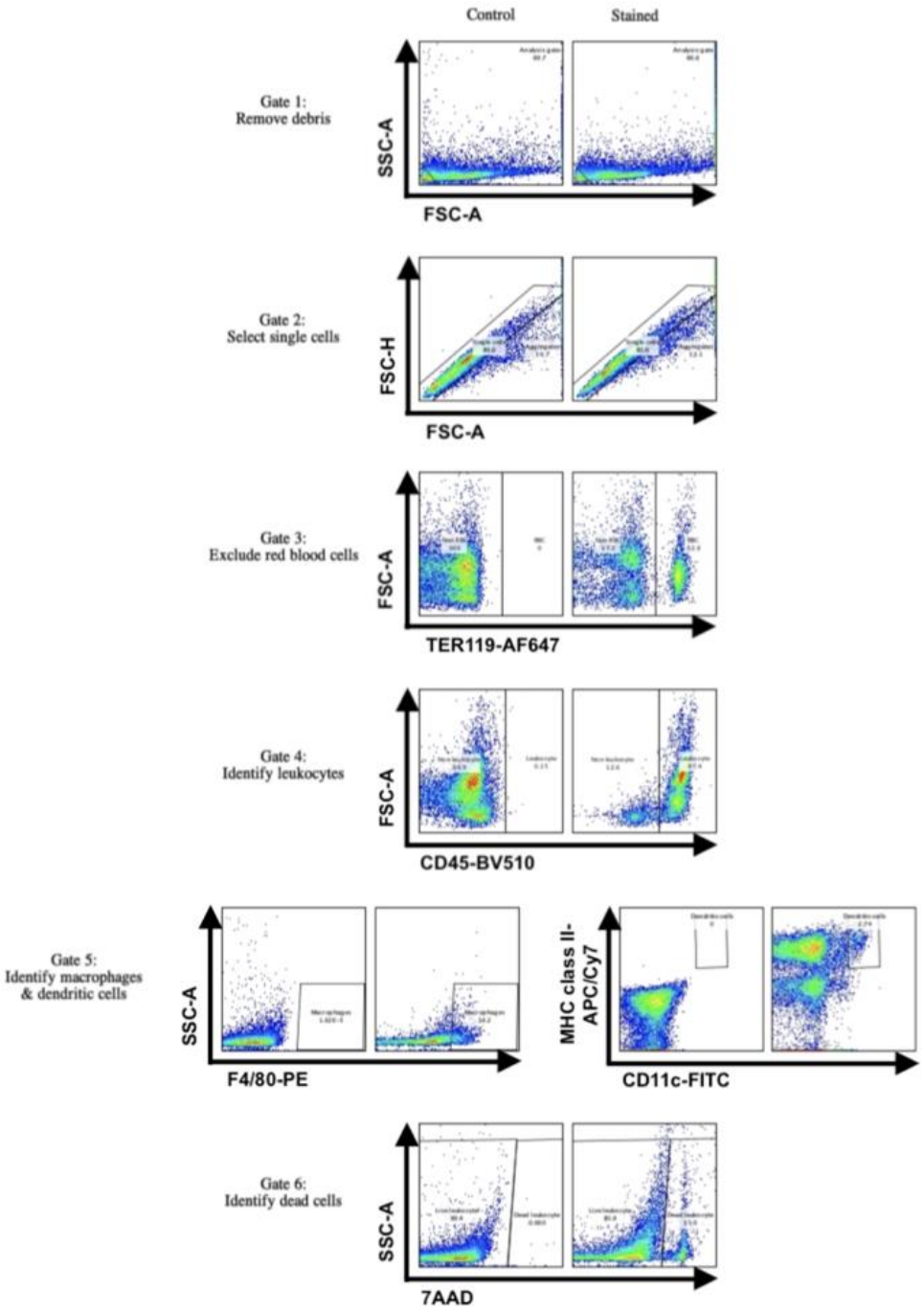

Figure 4.8: Primary flow cytometry panel gating scheme. Cell suspensions obtained from dissociated spleen samples were stained with the fluorescent probes listed in Table 4.1 and analyzed using flow cytometry. Acquired data was compensated and assessed using a sequential gating scheme. Gate 1, based on FSC-A vs. SSC-A, was used to exclude debris near the origin. Gate 2 was was used to select single cells based on FSC-A vs. FSC-H. Gate 3 identified and excluded red blood cells based TER119-AF647 positive signal. Gate 4 identified leukocytes based on CD45-BV510 positive signal. Gate 5 was applied to the TER119-,CD45+ cell subset to identify macrophages based on positive F4/80-PE signal, and to identify dendritic cells based on positive MHC class II-APC/Cy7 and CD11c-FITC signals. Finally, gate 6 was used to identify live cells in leukocyte, macrophage, and dendritic cell subsets based on negative 7-AAD signal. Appropriate isotype controls were initially used to assess nonspecific background staining, and appropriate fluorescence minus one (FMO) controls were used to determine positivity and set gates. Control samples were left unstained.

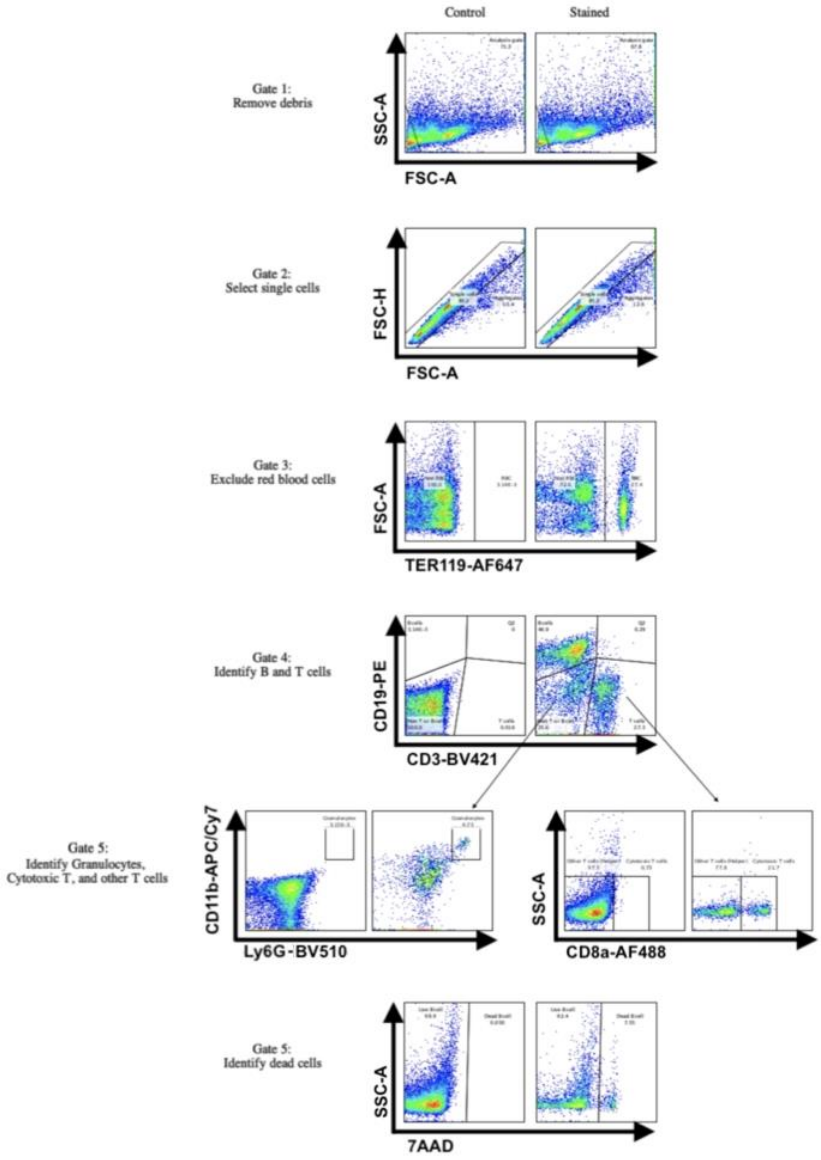

Figure 4.9: Secondary flow cytometry panel gating scheme. Cell suspensions obtained from dissociated spleen samples were stained with the fluorescent probes listed in Table 4.1 and analyzed using flow cytometry. Acquired data was compensated and assessed using a sequential gating scheme. Gate 1, based on FSC-A vs. SSC-A, was used to exclude debris near the origin. Gate 2 was was used to select single cells based on FSC-A vs. FSC-H. Gate 3 identified and excluded red blood cells based TER119-AF647 positive signal. Gate 4 was applied to the TER119- cell subset to identify B cells based on positive CD19-PE signal and negative CD3-BV421, and to identify T cells based on positive CD3-BV421 signal and negative CD19-PE signal. Gate 5 was applied to the CD3-,CD19- cell subset to identify granulocytes based on positive Ly6G-BV510 and CD11b-APC/Cy7 signals, and was applied to the CD3+, CD19- cell subset to identify cytotoxic T cells based on positive CD8a-AF488 signal. Finally, gate 6 was used to identify live cells in B cells, granulocytes, and T cell subsets based on negative 7-AAD signal. Appropriate isotype controls were initially used to assess nonspecific background staining, and appropriate fluorescence minus one (FMO) controls were used to determine positivity and set gates. Control samples were left unstained.

compensation beads (Invitrogen, Waltham, MA). Gates encompassing the positive and negative subpopulations within each compensation sample were inputted into FlowJo (FlowJo, Ashland, OR) to automatically calculate the compensation matrix. A sequential gating scheme was used to identify live and dead single immune cells from red blood cells, non-cellular debris, and cellular aggregates (Figs. 4.8 & 4.9). Signal positivity was determined using appropriate Fluorescence Minus One (FMO) controls. Control samples were left unstained.

4.4 Conclusion

In this work, we have demonstrated that a simple, microfluidic digestion device is capable of dissociating all major spleen populations more effectively than traditional dissociation methods. We first demonstrated that the device can be operated under high flow rates to improve spleen dissociation without adversely affecting cell viability for all investigated cell types. We show the device can be operated under static or interval formats, and similar results are achieved with either format. We demonstrate that the device can also be operated under either enzymatic or nonenzymatic conditions, or even used sequentially if desired. Under nonenzymatic conditions, which can be employed to preserve cell surface markers, the device matches or exceeds cell yields of a commonly used strainer control method. Device operation under enzymatic conditions greatly increases cell yields compared to nonenzymatic conditions. Using interval operation, we show that samples can also be easily sub-fractionated based on digestion time, with certain cell types, like dendritic cells preferentially dissociated when longer collagenase digestions are utilized. As such, this device could be employed as a method to crudely select one cell population over another. Finally, we develop an operational protocol employing both nonenzymatic and enzymatic

intervals. Using this protocol, we show that device processing results in higher cell yields of leukocytes overall, as well as higher numbers of dendritic cells, macrophages and monocytes, B cells, granulocytes, and T cell populations compared to both enzymatic and nonenzymatic control methods. Viability for device-processed samples matched or exceeded controls for all cell types. In future work, we will explore dissociating other lymphoid tissues, such as the thymus and lymph nodes, on-chip, and also seek to integrate downstream technologies to enable on-chip immune cell sorting and single cell analysis.

CHAPTER 5: Fluidic Device Platform to Standardize and Improve Mechanical Processing of Lipoaspirate for Autologous Therapeutics

5.1 Introduction

Interest is rapidly growing to utilize adipose tissue as a potent, easily accessible source of regenerative cells. Adipose-derived stem cells (ADSCs) are a subset of mesenchymal stem cells with adipogenic, osteogenic, and chondrogenic differentiation potential.[143,144] Since discovery in 2001,[18] ADSCs have been shown to improve regeneration in bone,[145] cartilage,[146] cardiac tissue,[147] and other organs.[148] Moreover, ADSCs have exhibited potential for treating immune-mediated diseases including rheumatoid arthritis and Crohn's disease.[149,150] Adipose tissue is typically obtained via tumescent liposuction, which fragments the sample into smaller pieces of tissue depending on the dimensions of the cannula. The lipoaspirate (LA) is then digested with a proteolytic enzyme such as collagenase to release cells from tissue and adipocytes are removed via density difference, resulting in a sample that is called the stromal vascular fraction (SVF). Finally, ADSCs are isolated from SVF based on adherence to tissue culture flasks. Recently, attention has shifted to directly utilizing SVF to avoid significant drawbacks associated with tissue culture, which include time, cost, introduction of foreign components in the media, and potential phenotypic changes from 2D culture on plastic. SVF comprises a diverse population including mature cells such as fibroblasts, endothelial cells, pericytes, and macrophages, regenerative cells such as MSCs and endothelial progenitor cells (EPCs), and contaminating blood cells. Importantly, SVF has been shown to exhibit comparable regenerative capabilities as ADSCs, including improved healing of burns,[19] scars, and ischemic wounds in diabetes.[20,21] SVF has also demonstrated therapeutic potential in models of multiple sclerosis, Crohn's disease, and

diabetic foot ulcers.[22,23,151,152] These regenerative properties have been attributed to the secretion of cytokines and growth factors that promote wound healing and angiogenesis, modulate the immune response, and reduce inflammation.[24,25,148]

For clinical applications, another concern is that enzymatic digestion of adipose tissue using collagenase does not meet the Food and Drug Administrations (FDAs) guidelines for "minimal manipulation," and thus is classified as an experimental drug.[153] This has led to the development of mechanical methods to liberate SVF from lipoaspirate without the use of enzymes. A common method involves repeatedly passing lipoaspirate back and forth between two syringes connected by a luer fitting, resulting in an emulsion termed nanofat.[29] After a filtration step, nanofat has been injected through small-bore needles and shown to be effective in correcting superficial rhytides, scars, and discoloration, as well as improving neovascularization and fat graft survival.[29,30,154] We recently characterized the cellular composition of nanofat, and demonstrated that stem and progenitor cell populations were enriched by mechanical stress in comparison to unprocessed lipoaspirate.[31] Specifically, we observed an increase in the percentage of MSCs, EPCs, and a subset of MSCs called multilineage differentiating stress-enduring (MUSE) cells, which exhibit pluripotency.[155–157] Other mechanical methods have been developed, including centrifuging, shaking, and vortexing,[158] as well as commercial methods such as Lipogems,[159] Revolve,[160] and Puregraft.[161,162] For each of these methods, however, multiple manual processing steps are required that could result in poor standardization and repeatability.

In previous work, we developed a suite of microfluidic device technologies that work in concert to dissociate tissue, specifically into single cells, in an automatable, standardized fashion. Each tissue processing technology operates at a different size scale, from cm x mm-

scale tissue specimens down through aggregates and finally single cells. The digestion device reduces tissue samples into large aggregates using the combination of hydrodynamic fluid shear and proteolytic enzymes.[37] Next, our dissociation device uses a network of branching channels with repeated expansion and constriction regions to generate shear forces to break down large cellular aggregates into smaller cell clusters and single cells.[38,39] Finally, our filtration device uses nylon membranes to eliminate remaining aggregates by means of both capture and dissociation mechanisms.[97] With appropriate design modifications, these technologies are poised to tackle the unique challenges posed by mechanical processing of human lipoaspirate samples.

In this work, we present a novel, integrated fluidic device platform for mechanically processing adipose tissue into an injectable therapeutic (Fig. 5.1). This will help standardize hydrodynamic processing of LA by producing predictable and consistent shear forces and enabling automation in clinical settings. Moreover, progressive processing through multiple devices will enable optimal recovery of regenerative cells while preventing clogging. First, we develop the emulsification device to replace the inter-syringe method used to produce nanofat. We show that SVF generated by the emulsification device matches or exceeds nanofat in terms of total cell numbers, as well as key stem and progenitor cell populations including DPP4+/CD55+ cells which are known to improve wound healing.[163] Next, we adapt our microfluidic filtration device concept to accommodate emulsified lipoaspirate. This includes increasing size in terms of device volume and filter membrane surface area to process larger samples. Pore size was also increased to 1 mm so that only the largest tissue pieces would be removed. We found that passing emulsified sample through the filter device generally maintains total cell numbers and relative cell numbers for progenitor/stem

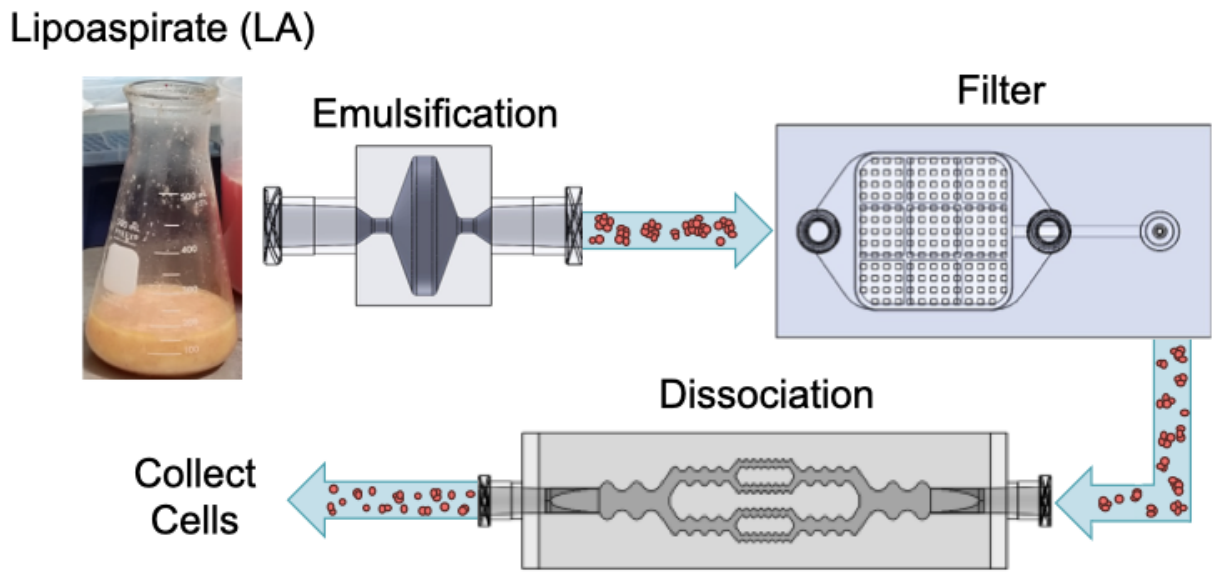

Figure 5.1: Integrated device processing platform for adipose tissue. Lipoaspirate (LA) is first broken down into smaller tissue aggregates using the emulsification device. Sample is then passed through the LA filter device to remove the largest tissue pieces, which would clog injection needles or downstream device channels. Finally, the smaller tissue fragments will be passed through the LA dissociation device, where higher levels of shear force will be applied to further break down tissue and optimally activate resident stem and progenitor cell populations. Following processing with these three devices, the final cellular suspension could be injected directly into a patient for wound healing or other regenerative therapies.

populations. Conversely, passing nanofat through a standard 1 mm mesh cloth resulted >2-fold reduction of total cells recovered, as well as a decrease in the relative number of MSCs and EPCs. We then adapt our microfluidic dissociation device technology to further shear tissue aggregates remaining after the filtration device. The dissociation device did not significantly affect total cell recovery, but did provide for an enrichment of CD34+ cells and EPCs that was dose dependent with flow rate. Interestingly, MUSE cells decrease in a dose-dependent manner. Finally, we assayed the expression of wound healing-related genes by real-time quantitative polymerase chain reaction (RT-qPCR) to investigate the effects of mechanical processing with our devices. We find that mechanical processing of lipoaspirate significantly activates unique transcriptional programs linked to improved wound healing and that our new fluidic device platform elicited responses that were at least comparable to

nanofat. Most promisingly, for expression of proangiogenic biomolecules, device processing often elicited responses substantially stronger than seen in nanofat. In future work, we will assess transcriptional changes at single cell resolution to delineate the extent to which our results can be correlated to differential enrichment of cell subtypes and induction of new transcriptional programs via mechanical activation. We will also explore whether device processing translates to similar wound healing dynamics and therapeutically relevant effects using various *in vivo* models.

5.2 Results and Discussion

5.2.1 Device Design Concepts

Human lipoaspirate presents unique processing challenges because it is a mixture of nonuniform-sized tissue fragments, cells, and fatty oils that requires both micronization and emulsification. While nanofat processing has been shown to be effective, the method suffers from the fact that nanofat is a manual method subject to user variability, which presents a challenge to generating consistent and reproducible flow rates, shear forces, and quality of the final cell suspension. Furthermore, a separate filtration step is required prior to injection. To standardize and automate the processing of lipoaspirate for clinical settings, we have developed three new device technologies that can be integrated into a single platform and produce a final cell suspicion that can be directly injected.

The emulsification device (ED) was designed to micronize and emulsify lipoaspirate in a manner similar to nanofat processing using the inter-syringe method.[29] As shown in Figure 5.2A, the emulsification device features two 1.5 mm diameter constriction regions that are separated by an abrupt expansion. The constrictions generate shear forces that break down tissue into smaller units. Based on the high viscosity of lipoaspirate, we expect

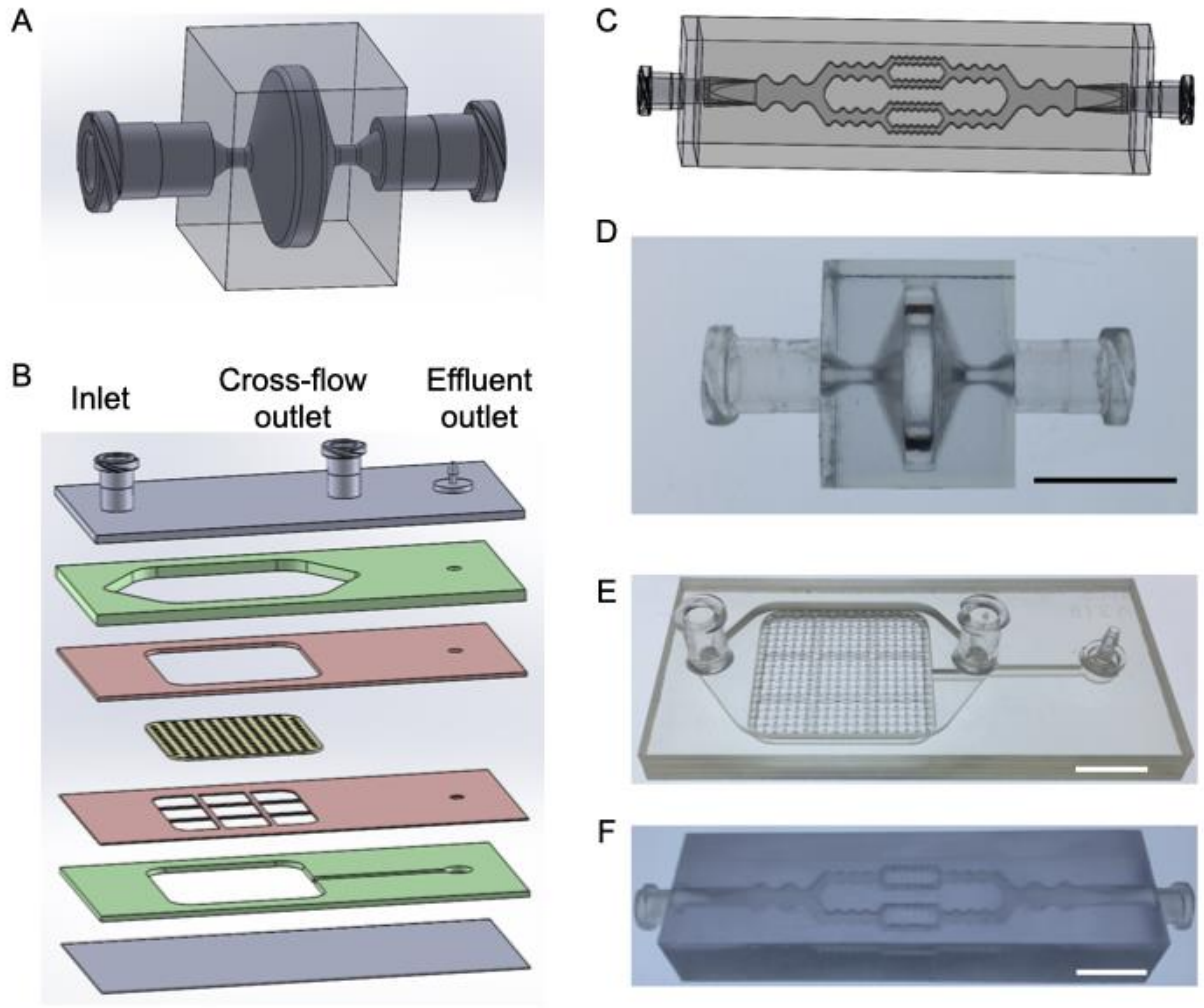

Figure 5.2: Device concepts and designs. (A,D) Emulsification device for breaking down LA into smaller tissue fragments. (A) Computer-aided design and (D) fabricated device produced by 3D printing. (B,E) LA filter device for removing large tissue fragments leftover from the emulsification device. (B) Exploded view showing six hard plastic layers, including two channel layers (green), filter spacer and support grid layers (red), an embedded nylon filter, and two layers sealing the top and bottom of the device. (E) Top and side views of fabricated device with 1000 μm pore nylon filters. (C,F) LA dissociation device for further break down of tissue fragments and activation of regenerative cells. (C) Computer-aided design and (F) fabricated device produced by 3D printing. Scale bars are 1 cm.

laminar flow within the constrictions, which will provide consistent and reliable shear forces for micronization. The rapid expansion is designed to achieve turbulent mixing that will emulsify the fatty oil layer. The emulsification device was fabricated by 3D printing using a biocompatible resin, with luer inlet and outlet ports printed on the sides of each constriction region. 3D printing was chosen over other fabrication methods due to the ability to produce a single monolithic part that could withstand high flow rates and pressures required for

lipoaspirate processing, in which device clogging is commonly experienced. A fabricated emulsification device is shown in Fig. 5.2D.

Next, the filtration device (FD) will capture large, mm-scale pieces of adipose tissue that remain after processing with the emulsification device. These large pieces of tissue could clog downstream operations such as further device processing or injection of the cellular therapeutic through small-bore needles. This would replace the standard syringe filters used for nanofat. The filtration device utilizes a multi-layer design that that includes fluidic channels and an embedded nylon mesh membrane (Fig. 5.2B), similar to our previous work focused on single cell filtration.[97] We again utilized single layer, woven nylon mesh membranes, but pore size was now increased to either 0.5 or 1 mm. This is similar to the pore sizes used to filter nanofat prior to injection.[29] Due to the large volume of lipoaspirate samples, we increased the surface area of the membrane by >10-fold, and added a grid support structure underneath to prevent collapse. Devices were fabricated by ALine, Inc. using a commercial laminate approach, where fluidic channels and openings for membranes, lures, and hose barbs were micro-machined into acrylic layers using a CO_2 laser. Nylon mesh membranes with 500 and 1000 μm pore sizes were laser cut to appropriate size. Device layers, nylon mesh membranes, luers, and hose barbs were then assembled, bonded using adhesive, and pressure laminated to form a single monolithic device. A fabricated filtration device is shown in Fig. 5.2E.

Finally, the dissociation device (DD, Fig. 5.2C) will further break down tissue fragments and enhance stem/progenitor cell activity. Reducing tissue size will prevent needle clogging during injection of the final cellular therapeutic, as well as to help increase survival without being vascularized. This device will also enhance mechanical fluid shear,

which has been shown to impact gene expression and secretion of many key biomolecules involved in wound healing and angiogenesis.[164–169] The dissociation device design was modified from previous work, in which the goal was to generate single cells from solid tissue samples.[38,39] Since attaining single cells is not necessarily required here for therapeutic applications of SVF, the dimensions of the channel features were increased in terms of width and height. Specifically, the dimensions of the dissociation device are 3000, 1500, and 750 μm in width for the 3 different stages. The height was 750 μm in each stage. Dissociation devices were 3D printed using a biocompatible resin. The branching network of channels in this device, as well as the luer inlet and outlet ports, were printed as a single unit in order to withstand the high flow rates and pressures experienced during device operation. A fabricated device is shown in Fig. 5.2F. For all devices in this study, a syringe pump was used to pass LA back and forth between the device using syringes connected to each side via inlet and outlet.

5.2.2 Emulsification Device Optimization

Performance of the emulsification device was evaluated using human LA samples obtained both healthy and diabetic patients using standard tumescent, vacuum-assisted liposuction. LA was washed with phosphate-buffered saline (PBS) and sub-divided into separate portions. One portion was not mechanically processed, termed macrofat (MF). Another portion was processed into nanofat by manually passing 30 times between two connected syringes, as originally described by Tonnard *et. al*.[29] Remaining samples were processed with the emulsification device for 10, 20, or 30 passes using a syringe pump set to a flowrate of 20 mL/s, approximately the same flowrate used to manually produce nanofat. All samples were then digested with collagenase to isolate SVF, as previously described.[28]

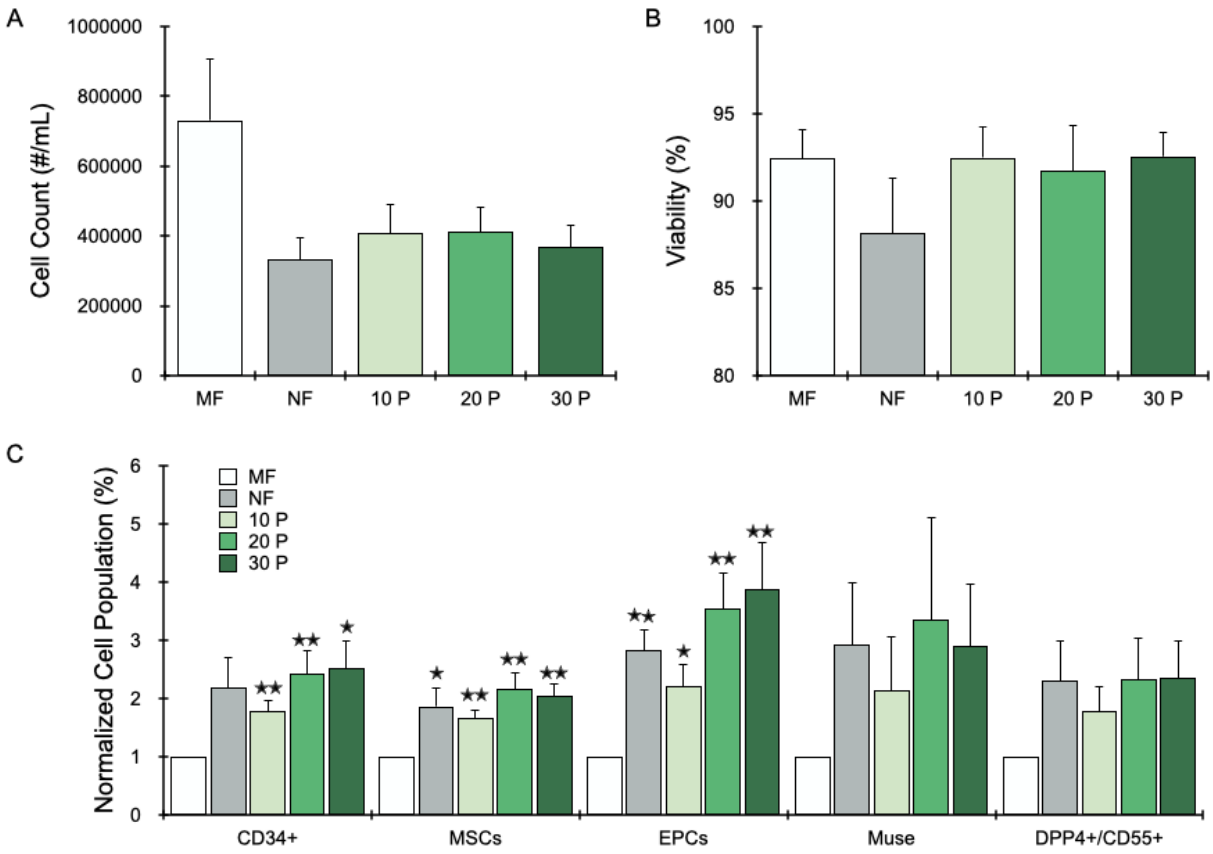

Figure 5.3: Emulsification device results. Healthy human LA (N = 5) was mechanically processed using 2 syringes (nanofat, NF) or the emulsification device for 10, 20, or 30 passes. Unprocessed LA is indicated as macrofat (MF). All samples were digested with collagenase prior to cell analysis. (A) Nucleated cell counts decreased by ~half for nonfat and all device-processed conditions. (B) Nucleated cell viability remained at ~90% for all conditions. (C) Mechanical processing enriched all cell types of interest, often by 2- to 3-fold compared to MF, with the emulsification device providing similar or improved results compared to NF. Error bars represent standard errors from at least three independent experiments. * indicates $p < 0.05$ and ** indicates $p < 0.01$ relative to MF.

Nucleated cell counts and viability were determined using an automated, dual-fluorescence cell counter. For healthy patients (N = 5), macrofat samples yielded the highest cell counts at approximately 700,000 cells/mL LA (Fig. 5.3A). Nanofat and all emulsification device conditions had lower cell counts by nearly half. Decreased cell counts were likely due to destruction of fragile cells by shear forces, which has previously been observed for adipocytes during nanofat processing.[29] However, viability was found to be similar at ~90% for all conditions (Fig. 5.3B). This suggests that the cells that were lost during nanofat or

device processing were reduced to debris and removed during subsequent washing steps or could not be recognized as a cell by automated cell counter.

Table 5.1: Flow cytometry probe panel

Assay	Probe
CD34	Anti-CD34 Ab (clone 561)-BV421
CD45	Anti-CD45 Ab (clone 2D1)-BV510
SSEA-3	Anti-SSEA-3 Ab (clone MC-631)-FITC
CD26	Anti-CD26 Ab (clone BA5b)-PE
CD31	Anti-CD31 Ab (clone WM59)-PE/Cy7
CD55	Anti-CD55 Ab (clone JS11)-APC
CD13	Anti-CD13 Ab (clone WM15)-APC/Cy7
Viability	7-AAD

Next, we used flow cytometry and the fluorescent probe panel listed in Table 5.1 to identify the stem and progenitor cell subsets listed in Table 5.2. The sequential gating scheme used for flow cytometry analysis is described in Figure 5.4. CD34 is of interest because it is a known stem cell marker,[170] and higher percentages of CD34+ cells in SVF has been linked to improved fat graft survival.[171] MSCs are essential in wound healing due to their differentiation potential, anti-inflammation characteristics, and paracrine and immunomodulatory functions,[76] while endothelial progenitor cells have been implicated as a key cell type in revascularization due to angiogenic and paracrine effects.[172] Muse and DPP4+/CD55+ cells are both subtypes of MSCs that are of particular interest in regenerative

medicine. Muse cells are known to be pluripotent, nontumorogenic, and extremely stress tolerant stem cells.[155,156] Both Muse and DPP4+/CD55+ cells have also been shown to improve wound healing in diabetic murine models.[157,163]

Table 5.2: Stem and progenitor cell types of interest

Cell type	Markers	Significance
CD34+	CD34+	Common marker for multipotentiality
Mesenchymal Stem Cells (MSCs)	CD45-, CD31-, CD34+	Key in regenerative wound healing
Endothelial Progenitor Cells (EPCs)	CD45-, CD31+, CD34+	Vascularization of healing tissues
Multilineage Differentiating Stress-Enduring (Muse)	CD45-, CD31-, CD34+, SSEA-3+, CD13+	Nontumorigenic, pluripotent, stress tolerant stem cells
DPP4+/CD55+	CD45-, CD31-, CD34+, CD26+, CD55+	Improved wound healing in diabetic models

The various stem/progenitor populations measured for healthy patients are shown in Fig. 5.3C. Results were normalized to macrofat, as relative numbers within SVF have been shown to vary widely across different patients and anatomical locations of adipose tissue harvest.[171,173] Nanofat processing enriched all cell populations by 2- to 3-fold, as shown previously for all but the DPP4+/CD55+ case.[31] Emulsification device processing also enriched all cell populations, which increased between 10 and 20 passes, however, 30 passes did not provide significant increases. Overall, nanofat and emulsification device processing provided comparable enrichment of CD34+ cells (~2.5-fold), MSCs (~2-fold), Muse cells (~3-fold), and DPP4+/CD55+ cells (~2.5-fold). EPCs were slightly higher for the emulsification device (~4-fold) relative to nanofat (~3-fold), but this difference was not statistically significant.

For a cohort of diabetic patients (N = 4), similar trends in cell count, viability, and stem/progenitor cell enrichment were observed for nanofat and emulsification device

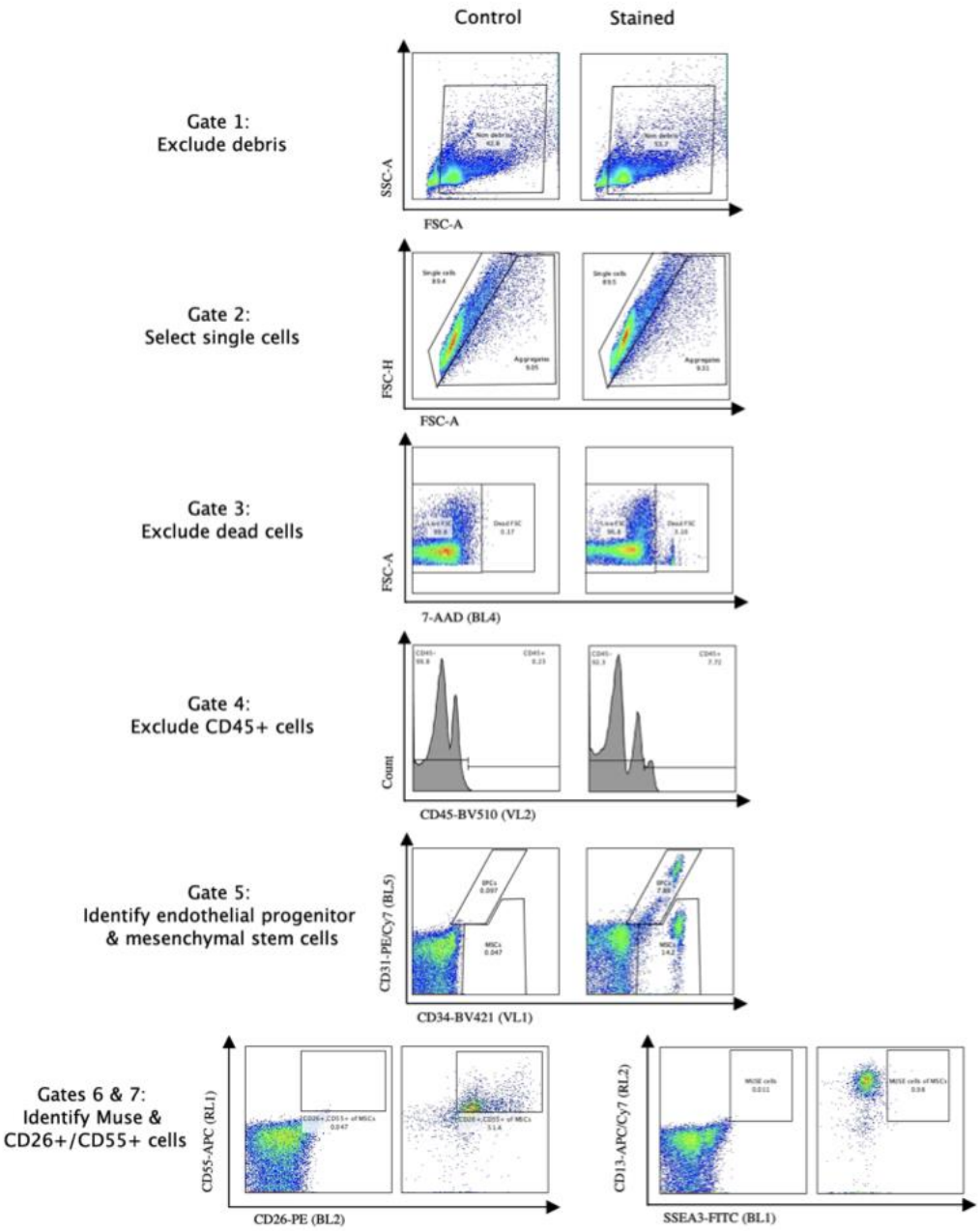

Figure 5.4: Flow cytometry gating scheme. Following collagenase digestion, cell suspensions were stained with fluorescent probes listed in Table 5.1 and analyzed using flow cytometry. Acquired data was compensated and assessed using a sequential gating scheme. Gate 1, based on FSC-A vs. SSC-A, was used to exclude debris near the origin. Gate 2 was then used to select single cells based on FSC-A vs. FSC-H. Gate 3 was used to exclude dead cells based on positive 7-AAD signal. Gate 4 was applied to the live cell subset to exclude hematopoietic cells based on positive CD45-BV510 signal. Gate 5 was applied to the CD45- cell subset to identify endothelial progenitor cells based on positive CD34-BV421 and CD31-PE/Cy7 signals, and to identify mesenchymal stem cells (MSCs) based on positive CD34-BV421 and negative CD31-PE/Cy7 signals. Gate 6 was applied to the CD34+, CD31- MSC subset to identify CD26+/CD55+ cells based on positive CD26-PE and CD55-APC signals. Gate 7 was applied to the CD34+, CD31- MSC subset as well, in order to identify multilineage differentiating stress enduring (Muse) cells based on positive SSEA3-FITC and CD13-APC/Cy7 signals. Appropriate isotype controls were used to assess nonspecific background staining, and appropriate fluorescence minus one (FMO) controls were used to determine positivity and set gates.

processing conditions (Figs. 5.5A - C). Specifically, EPCs were again higher for the emulsification device in comparison to nanofat, but still not significant. Enrichment of these stem/progenitor populations is particularly encouraging in the context of diabetes, as wound healing and neovascularization are well known to be significantly impaired.[174] For adipose tissue specifically, diabetes has been shown to deplete key subpopulations of ADSCs, resulting in impaired angiogenic potential.[175] This could ultimately limit their usefulness in autologous therapies for diabetics, highlighting the need for methods that can successful enhance these depleted populations in an effort to improve efficacy.[176]

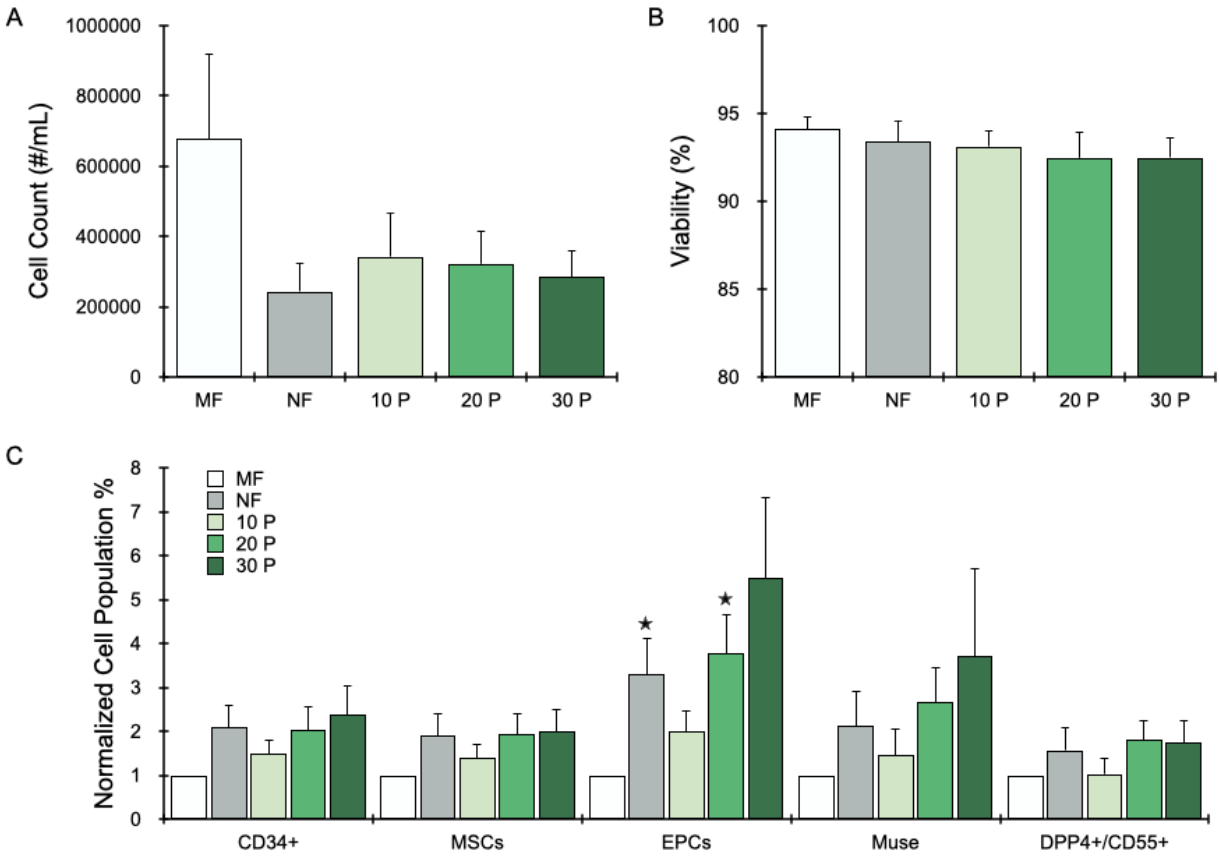

Figure 5.5: Emulsification device results for diabetic patients. Diabetic human LA (N = 4) was mechanically processed using 2 syringes (nanofat, NF) or the emulsification device for 10, 20, or 30 passes. Unprocessed LA is indicated as macrofat (MF). All samples were digested with collagenase prior to cell analysis. Results for (A) nucleated cell counts, (B) viability. and (C) normalized cell populations closely followed trends shown in Fig. 5.3 for healthy LA samples. Error bars represent standard errors from at least three independent experiments. * indicates $p < 0.05$ relative to MF.

5.2.3 Filter Device Optimization

Next, filter devices were tested on lipoaspirate that was first processed using the emulsification device for 30 passes. This is intended to replace the manually filtering step that is needed prior to injection of nanofat. We evaluated filter devices containing either 500 or 1000 μm nylon mesh membranes. For comparison, we also tested nanofat after passing through a 1000 μm mesh cloth. After processing, samples were digested with collagenase and tested for cell count, viability, and stem/progenitor content as in the previous section.

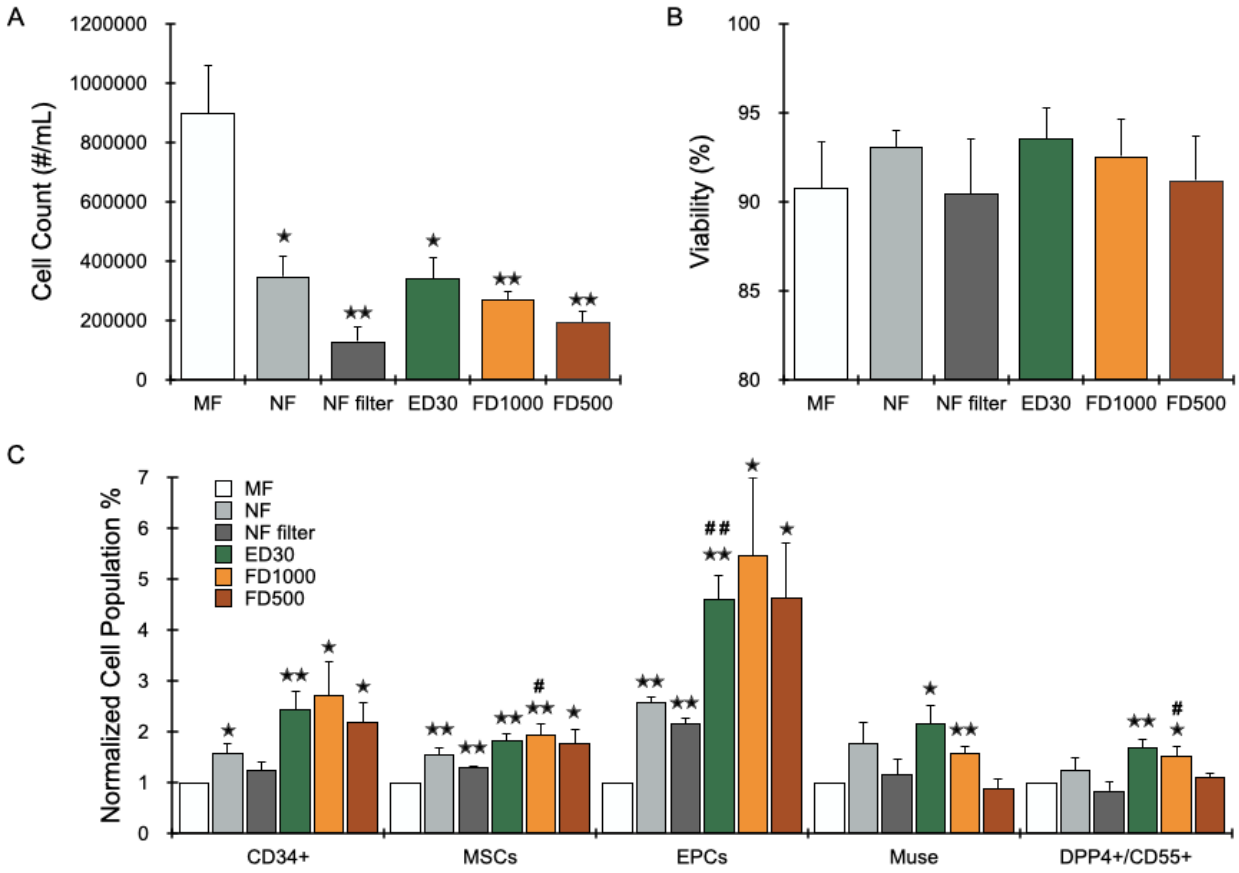

Figure 5.6: LA filter device results. Healthy human LA (N = 4) was mechanically processed using 2 syringes (nanofat, NF) or the emulsification device for 30 passes (ED30). NF was also manually filtered using a 1000 μm mesh cloth, while ED30 samples were filtered using the LA filter device (FD) with 1000 or 500 μm pores. Unprocessed LA is indicated as macrofat (MF). All samples were digested with collagenase prior to cell analysis. (A) Nucleated cell counts decreased by over half for NF and ED30 processed samples, and further decreased with filtering, most notably for the NF mesh filtered condition. (B) Nucleated cell viability remained >90% for all conditions. (C) ED30 followed by LA filter device enriched all cell types of interest, with improved results compared to MF and NF filtered conditions. Error bars represent standard errors from at least three independent experiments. * indicates $p < 0.05$ and ** indicates $p < 0.01$ relative to MF. # indicates $p < 0.05$ relative to NF filter. ## indicates $p < 0.01$ relative to NF.

Since normal and diabetic samples responded similarly to nanofat and emulsification device processing, only healthy fat was evaluated for these tests (N = 4). Total cells counts for macrofat, nanofat, and emulsification device conditions were similar to the tests. Total cell number was 9.0 x 10^5 cells/mL for macrofat, and decreased to ~3.5 x 10^5 cells/mL for both nanofat and the emulsification device (Fig. 5.6A), consistent with the initial experiments (Fig. 5.3A). Manually filtering nanofat drastically reduced cell count to 1.3 x 10^5 cells/mL. This indicates that most of the nanofat sample would be lost during filtering and not ultimately be used as an injectable therapeutic. The filter device better preserved cell recovery in the emulsification device sample, resulting in recovery of 2.7 and 2.0 x 10^5 cells/mL for the 1000 and 500 μm mesh membranes, respectively. The 500 μm membrane likely removed larger tissue fragments in a similar manner to the manual mesh filter. It is notable that the filter device with 1000 μm membrane utilized the same pore size as the manual filter, but allowed 2-fold more cells to pass through. It is unclear whether this was related entirely to the filter step, or whether differences in upstream processing, emulsification device versus nanofat, were also at play. We believe that the filter device was at least primarily responsible for improved performance, which could have resulted from a larger membrane surface area or smaller device hold-up volume. Moreover, the filter device may have promoted extrusion, or even direct dissociation, of most of the large tissue fragments, as we have previously observed for this filter device design using smaller tissue aggregates.[97] Thus, it is possible that similar results could be obtained for nanofat. This was not tested because our ultimate plan is to integrate the various devices for automated lipoaspirate processing. Cell viability remained high, in excess of 90%, for all conditions (Fig. 5.6B).

Flow cytometry analysis was then performed to determine whether filtering mm-scale aggregates that were more difficult to dissociate would have an adverse effect on the recovery of stem or progenitor cell populations. For this patient cohort, the emulsification device produced a substantially higher proportion of CD34+ cells and EPCs compared to nanofat (Fig. 5.6C). Specifically, there were ~1.5-fold more CD34+ cells and >2-fold more EPCs, with the EPC difference being significant. After manually filtering nanofat, we observed a decrease in all stem/progenitor populations (Fig. 5.6C). In fact, population percentages for filtered nanofat were reduced back to macrofat levels for all but MSCs and EPCs. We note that the lower relative number of stem/progenitor cells obtained upon manual filtering of nanofat exacerbates the loss to total cells in Fig. 5.6A, resulting in a net loss ranging from 3- to 4-fold for all stem/progenitor populations. Conversely, the filter device generally retained similar relative numbers of CD34+ cells, MSCs, and EPCs compared to the emulsification device without filtering. This was true for both 500 and 1000 μm pore sizes. Muse and DPP4+/CD55+ cell populations, however, were reduced by the filter device, in a dose-dependent manner with pore size. This finding suggests that a significant portion of the Muse and DPP4+/CD55+ cell populations reside within the largest tissue fragments that remain after nanofat or emulsification device processing. Compared to NF filtered samples, device filtered samples yielded ~2-fold more CD34+ cells, ~1.5-fold more MSCs, and 2 to 2.5-fold more EPCs. These results suggest that the LA filter devices are more effective at dissociating cell aggregates containing these stem/progenitor populations to a degree that they are able to pass through the filters and be recovered. The 1000 μm pore LA filter device yielded higher Muse and DPP4+/CD55+ populations than both the 500 μm pore device and NF filtered conditions. Based on this preliminary data, the 1000μm filter device generally

outperforms the 500 μm device, maintains the stem/progenitor populations most similar to a comparable unfiltered counterpart, and thus will be used for integration with the dissociation device.

5.2.4 Dissociation Device Optimization

Next, the dissociation device was tested using lipoaspirate from healthy patients (N = 4) that was first processed using the emulsification device for 30 passes followed by the 1000 μm LA filter device. Samples were then processed using 20 passes through the emulsification device at a flow rate of 100, 300, or 900 mL/min. This was intended to further break down aggregates and enrich key stem and progenitor cell populations. After processing, samples were digested with collagenase and quantified for cell count, viability, and stem/progenitor content as in the previous section. Total cell counts for macrofat were 9.3 x 10^5 cells/mL, and decreased by a factor of ~2 for all device conditions (Fig. 5.7A), similar to previous experiments (Fig. 5.3A and 5.6A) . All dissociation device conditions generated comparable total cell numbers, and cell viability remained at greater than 90% for all conditions (Fig. 5.7B), suggesting that the majority of cells can withstand the enhanced shear forces generated during dissociation.

Flow cytometry analysis was then performed to determine the effect of dissociation device processing has on key stem and progenitor cell populations. Dissociation device processing resulted in a dose dependent increase in CD34+ cells with flow rate (Fig. 5.7C), from ~3.3-fold higher than macro fat without dissociation to ~4-fold higher than macrofat for the 900 mL/min condition. However, the differences amongst device conditions were not significant. The MSC population was not affected by dissociation device treatment, remaining at 3-fold higher than macrofat. EPCs, however, increased in a dose dependent manner from

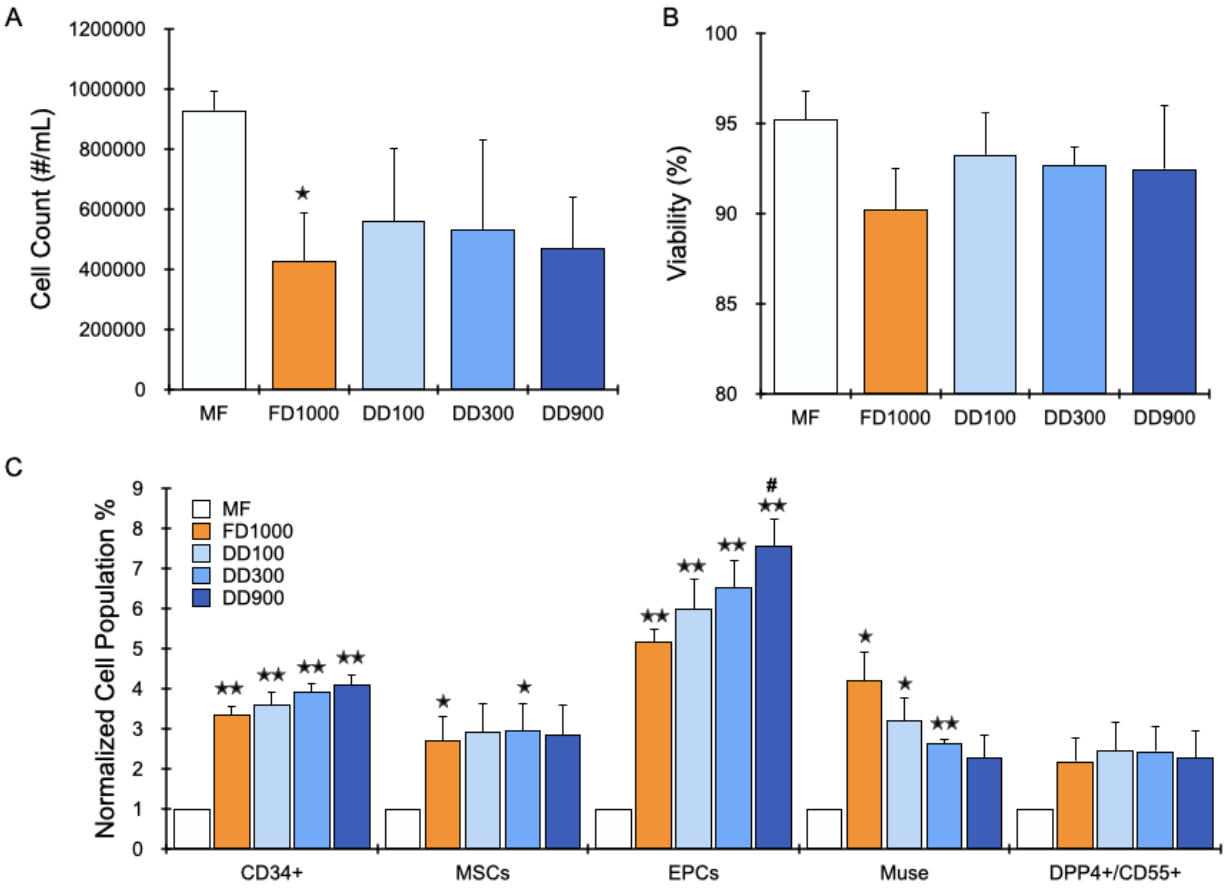

Figure 5.7: LA dissociation device results. Healthy human LA (N = 3) was mechanically processed using the emulsification device for 30 passes and the LA filter device with 1000 μm membrane (FD1000). Samples were then processed using the LA dissociation device (DD) for 20 passes at 100, 300, or 900 mL/min flow rate. Unprocessed LA is indicated as macrofat (MF). All samples were digested with collagenase prior to cell analysis. (A) Nucleated cell counts decreased by ~half for all device processed samples compared to unprocessed MF (B) Nucleated cell viability remained at ~90% for all conditions. (C) Enrichment device processing increased CD34+ and EPC populations modestly in a dose-dependent manner, while MSC and DPP4+/CD55+ populations were unaffected and Muse cells decreased with flow rate. Error bars represent standard errors from at least three independent experiments. * indicates $p < 0.05$ and ** indicates $p < 0.01$ relative to MF. # indicates $p < 0.05$ relative to FD1000.

~5-fold for FD1000 to over 7.5-fold for the 900 mL/min condition (DD900). Interestingly, Muse cells decreased as dissociation processing increased, suggesting that Muse cells may be susceptible to damage from high mechanical shear forces. The most aggressive mechanical 900 mL/min dissociation device treatment still yielded over 2-fold increase in Muse population compared to macrofat, however. DPP4+/CD55+ cell populations were unaffected by dissociation device processing, remaining at ~2.5-fold higher than macrofat.

5.2.5 Transcriptomic Analysis of Wound Healing Response

Mechanical forces have been shown to enhance cutaneous tissue growth and repair, influencing both the rate and quality of wound healing.[177] Mechanical fluid shear in particular has been shown to increase gene expression or secretion of various targets related to wound healing and angiogenesis,[164,165,167–169] including ADSCs.[166] To investigate the effect of mechanical processing with our devices, we assayed the expression of wound healing-related genes by real-time quantitative polymerase chain reaction (RT-qPCR). Specifically, we tested MF, NF with filtering, ED at 30 passes plus FD with 1000 μm filter (ED/FD), and ED/FD plus dissociation device at 900 mL/min (DD). Samples were processed and bulk RNA was harvested either immediately to serve as a baseline (0 hour) or after being cultured for 24 hours at 37°C in order to allow time for transcriptional changes to occur. After the 24 hour incubation, cell count, viability, and sub-population numbers determined by flow cytometry (Fig. 5.8) followed similar trends as the initial results in Figs. 5.6 and 5.7. However, we did observe lower total cell numbers and generally higher variability amongst subpopulation percentages. RT-qPCR results each gene in the panel were normalized to the housekeeping gene RPLP0. The NF filter and device samples were then normalized to MF at the same time point.

Gene expression immediately after processing for the entire wound healing panel are displayed as a heat map in Fig. 5.9A. Genes in which at least one of the mechanical processing conditions was significantly different than MF are shown in Figs. 5.9B-F. Differences in expression were modest, with significant results generally between 3-fold up- or down-regulated. We expect that these differences would reflect changes in cellular composition, since there was not sufficient time for transcriptional responses. Although it was rare for

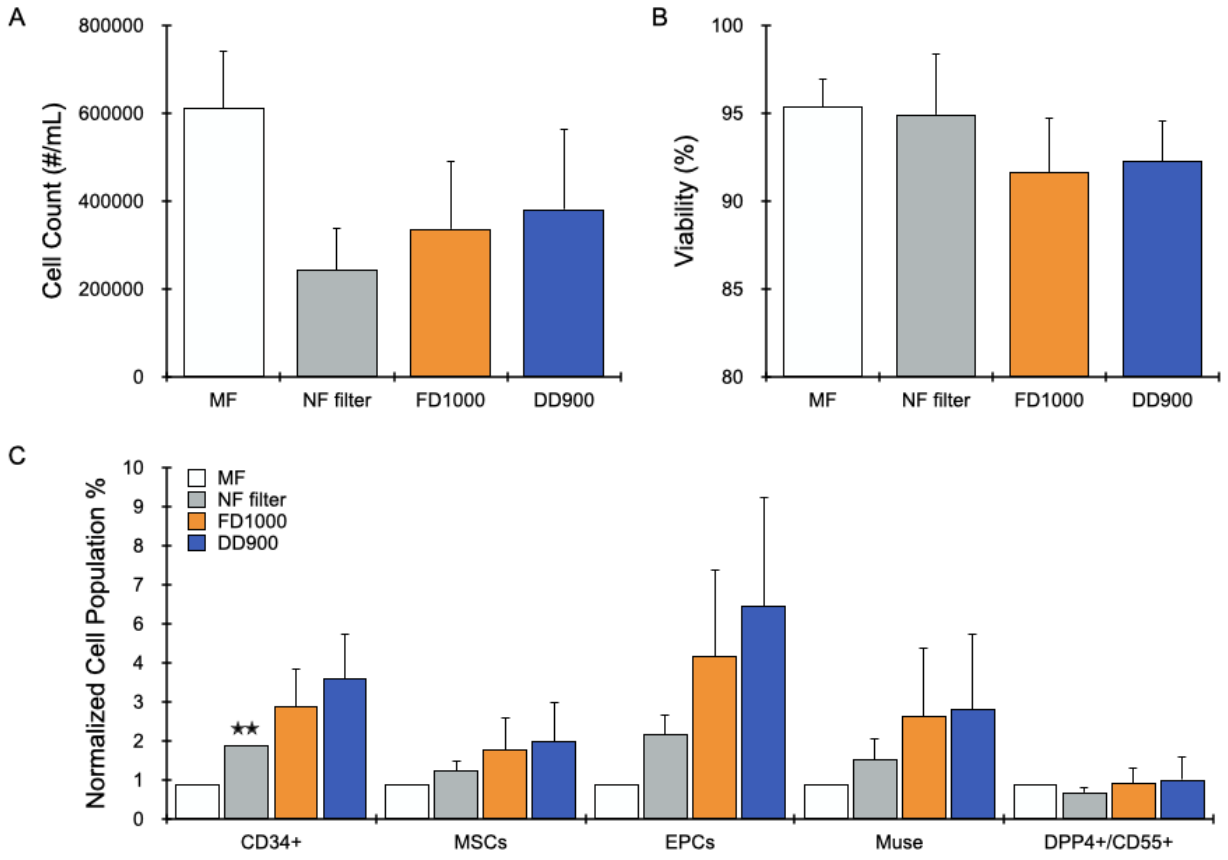

Figure 5.8: 24 hour incubation results. Healthy human LA (N = 3) was mechanically processed using the emulsification device for 30 passes followed by the LA filter device with 1000 μm membrane (FD1000). Some samples were then additionally processed using the LA dissociation device (DD) for 20 passes at 900 mL/min flow rate. Unprocessed LA is indicated as macrofat (MF). All samples were then transferred in media to incubator for 24 hours at 37°C. All samples were digested with collagenase prior to cell analysis. Results for (A) nucleated cell counts, (B) viability, and (C) normalized cell populations followed trends shown in Figs. 4 & 5 for 0 hour samples. Error bars represent standard errors from at least three independent experiments. ** indicates $p < 0.01$ relative to MF.

nanofat, ED/FD, and DD conditions to all be significantly different, they generally exhibited the same trend. Gene expression results after 24 hour are analogously presented in Fig. 5.10. Mechanical processing now elicited much stronger changes in expression, particularly for genes related to inflammation, matrix remodeling, and angiogenesis (Fig. 5.10A). The chemokines CXCL1 and CXCL2 (MIP2-α), as well as the cytokines IL-1β, IL-6, CSF2 (GM-CSF), and CSF3 (G-CSF), were all upregulated by >10-fold for the ED/FD and DD cases (Fig. 5.10B). While these genes were also significantly upregulated for NF (except IL-1β and CSF2), expression was consistently 4- to 10-fold lower than ED/FD and DD, and differences

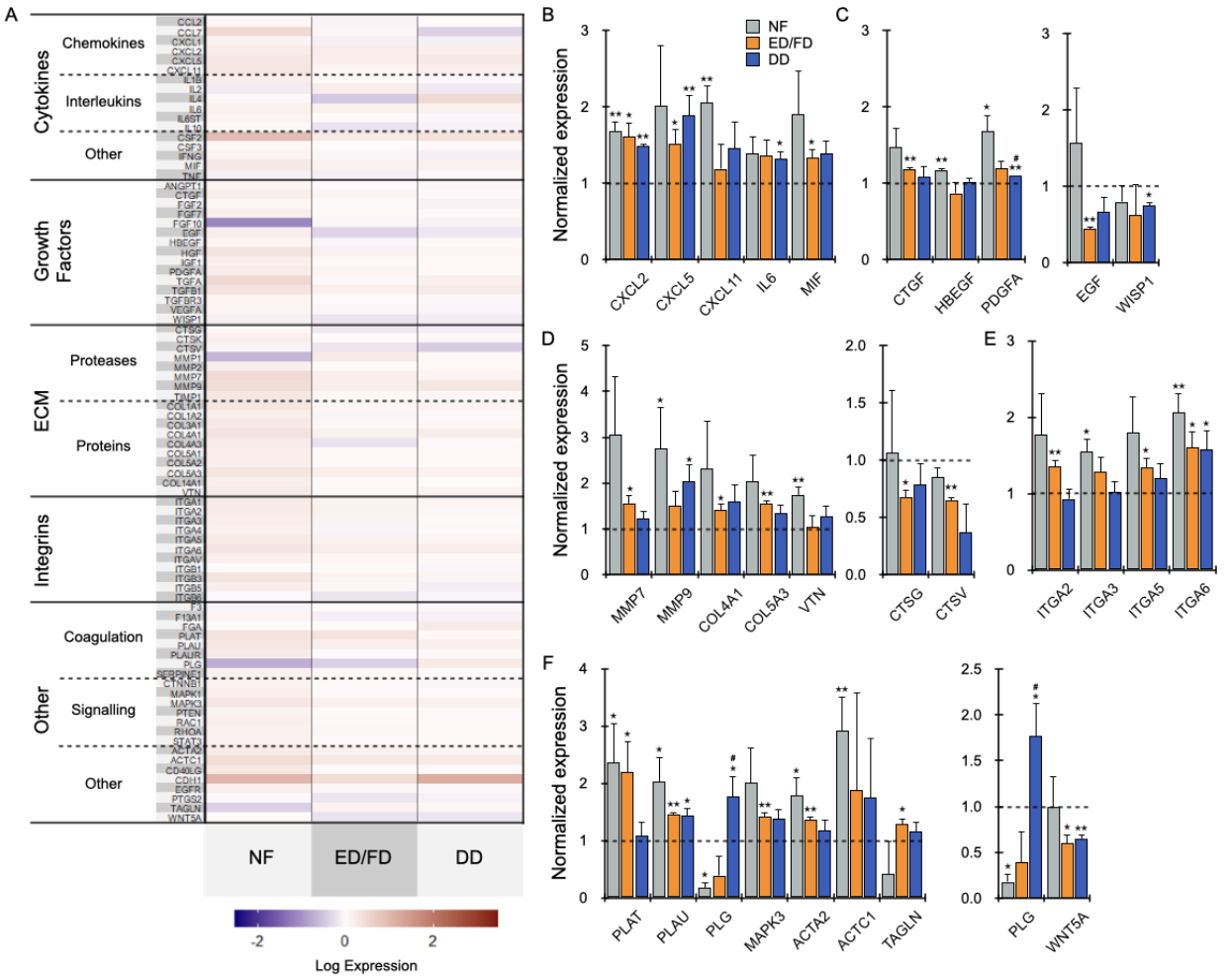

Figure 5.9: 0 hour RT-qPCR results. (A) Heat map of wound healing related genes. (B-F) Genes significantly up- or down-regulated relative to MF in at least one processed condition, grouped by (B) cytokines, (C) growth factors, (D) ECM, (E) integrins, and (F) other. Error bars represent standard errors from at least three independent experiments. * indicates $p < 0.05$ and ** indicates $p < 0.01$ relative to 0 hour MF. # indicates $p < 0.05$ relative to NF filter.

between processing methods were often significant. Other members of the CXCL family (5 and 11) also increased for ED/FD and DD treatment, but not NF. IL-2 was consistently downregulated. The growth factors FGF2 (basic FGF or bFGF), HBEGF (heparin-binding EGF-like growth factor or HB-EGF), and PDGFA were upregulated, although at a more modest level of ~2- to 4-fold for each processing conditions (Fig. 5.10C). FGF10 and HGF were downregulated. Members of the MMP family including 1, 2, and 9 were enhanced, while genes related collagen synthesis decreased (Fig. 5.10D). Integrin subunits α2, α5, αV, and β6

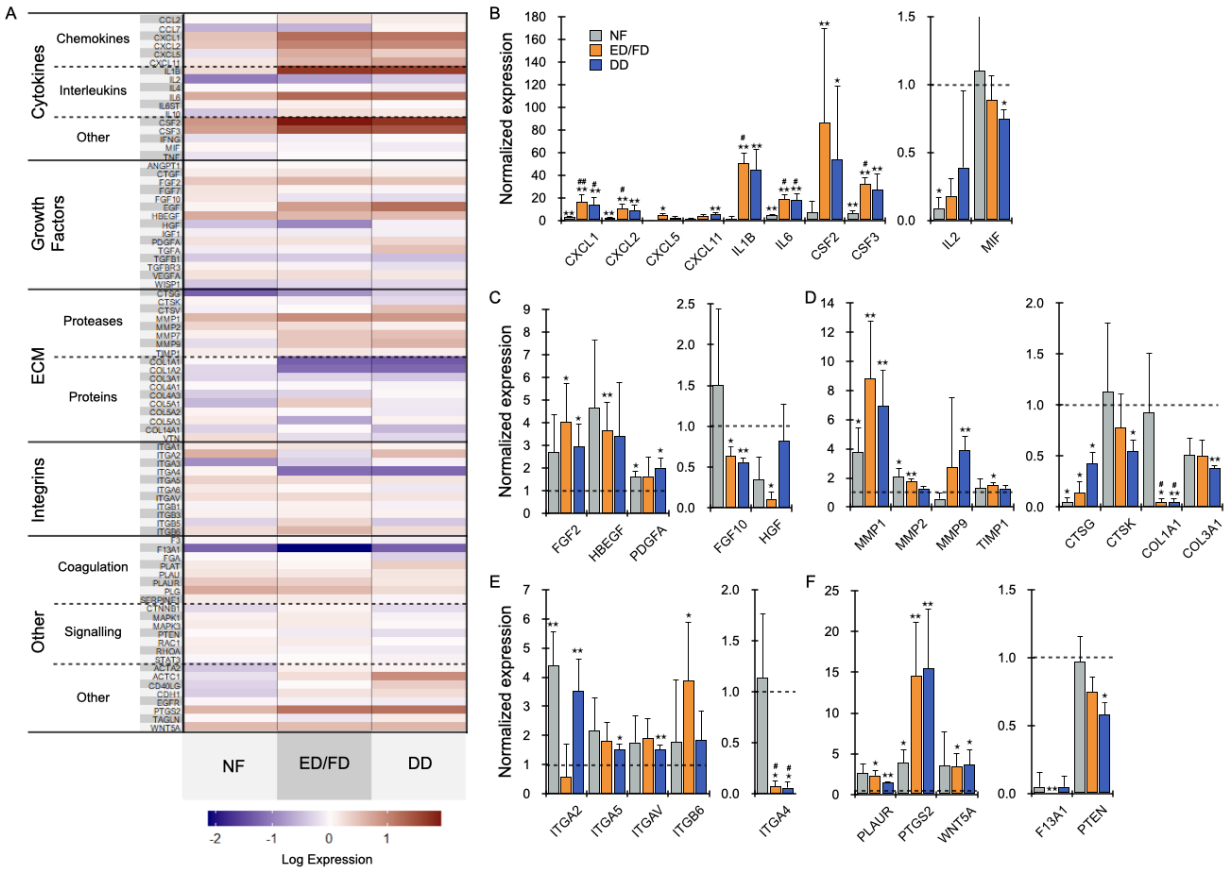

Figure 5.10: 24 hour RT-qPCR results. (A) Heat map of wound healing related genes. (B-F) Genes significantly up- or down-regulated relative to MF in at least one processed condition, grouped by (B) cytokines, (C) growth factors, (D) ECM, (E) integrins, and (F) other. Error bars represent standard errors from at least three independent experiments. * indicates $p < 0.05$ and ** indicates $p < 0.01$ relative to 0 hour MF. # indicates $p < 0.05$ and ## indicates $p < .01$ relative to NF filter.

were clearly upregulated, while only α4 was downregulated (Fig. 5.10E). Finally, PTGS2 (COX-2) expression increased substantially after ED/FD and DD treatments, by >10-fold, but a more modest increase was observed for NF (Fig. 5.10F).

Based on these results, we conclude that mechanical treatment with hydrodynamic shear stress elicits a pro-inflammatory environment. Members of the CXCL family (1, 2, 5, 11), IL-1β, IL-6, CSF2, CSF3, and PTGS2 are all inflammatory mediators that were upregulated by mechanical processing. Inflammation is invariably associated with the early stages of healing, to clear away damaged and dead tissue, and can also influence the

immunomodulatory, regenerative, angiogenic, and anti-poptotic potential of MSCs.[178,179] "Priming" MSCs with inflammatory challenges like IL-1β have been shown to push these cells to an anti-inflammatory, pro-regenerative phenotype and also to increase rates of tissue remodeling and angiogenesis.[180] Further, MSCs spheroids have been shown to induce IL-1β expression which initiates an "auto-priming" effect.[181,182] Thus, stimulating inflammation has been postulated as a means to enhance wound healing.[178,179] However, the balance between inflammation and wound healing is delicate and care must be given to avoid degenerating into chronic wound scenarios. In our case, priming is initially mechanical in nature, not chemical, although both approaches do converge on IL-1β. At this time, it remains unclear which cell subtypes within the complex SVF milieu may be responding to mechanical stimuli and/or secreting the inflammatory factors. We did observe that CXCL2, CXCL5, CXCL11, and IL-6 were all modestly elevated prior to culture (Fig. 5.9B), suggesting that differential enrichment of certain cell types may have played a role. However, we believe that cell activation also played a key role, as mechanical fluid shear has been linked to elevated gene expression and/or secretion of IL-1β,[164,183] IL-6,[183] CSF2,[184] CSF3,[166] CXCL1,[169] CXCL2,[169,185] and PTGS2.[164] Interestingly, the inflammatory genes exhibited the most consistent and dramatic differences between NF and ED/FD conditions, but DD treatment did not augment further. ED/FD processing prior to DD treatment may have generated sufficient shear stress to mechanically activate the cells. We do not believe the above results were caused by an immune response stemming from device materials or microbial contamination, since classic mediators such as TNF-α, CCL2 (MCP-1), and CCL7 (MCP-3) were not affected by device treatment. Instead, we contend that processing with the ED and FD devices produced higher shear stresses that enriched key subtypes, as seen for MSCs in Figure 5.3 and Figures 5.5-5.7,

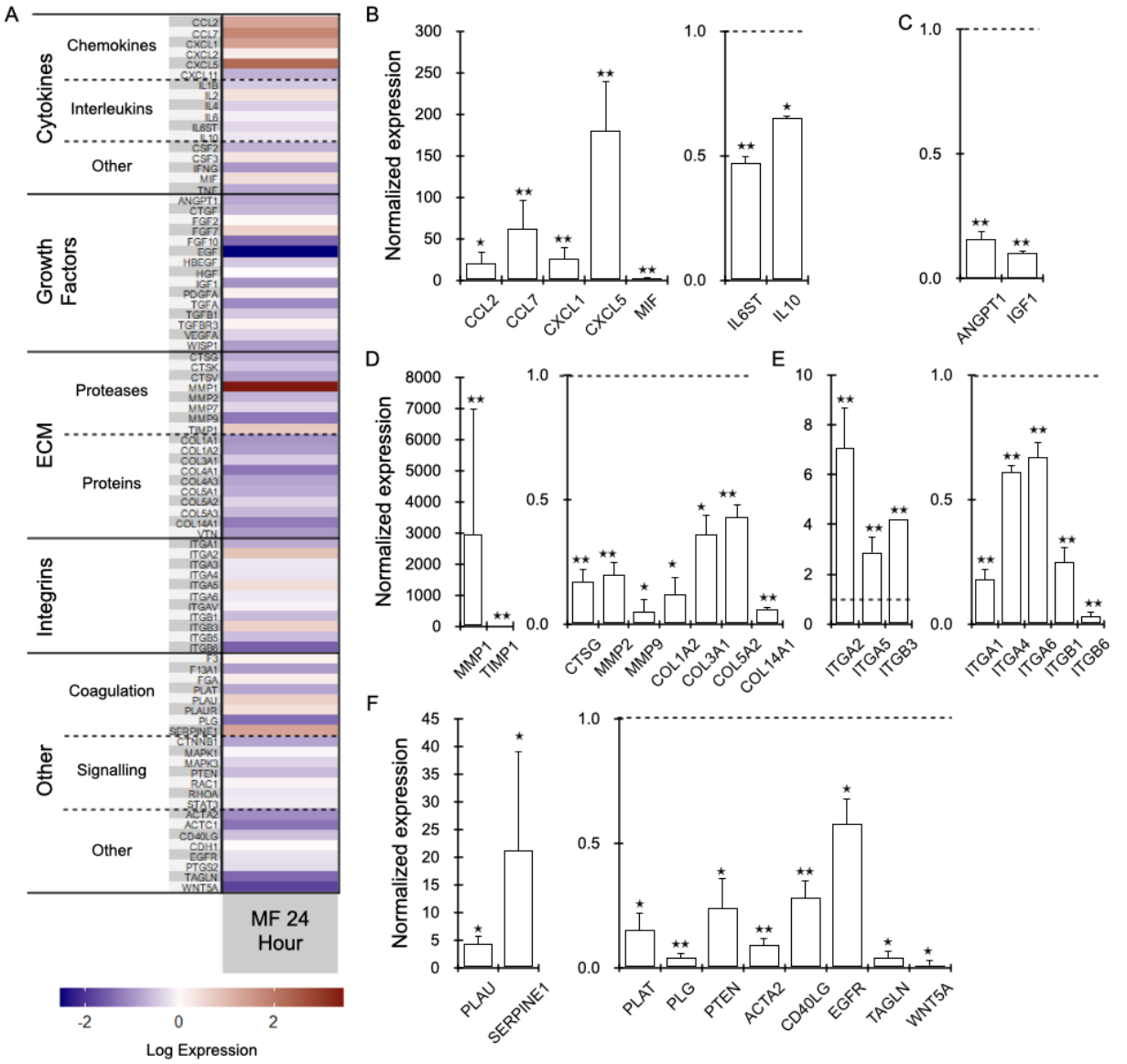

Figure 5.11: 24 hour MF normalized to 0 hour MF RT-qPCR results. (A) Heat map of wound healing related genes. (B-F) Genes significantly up- or down-regulated relative to MF in at least one processed condition, grouped by (B) cytokines, (C) growth factors, (D) ECM, (E) integrins, and (F) other. Error bars represent standard errors from at least three independent experiments. * indicates $p < 0.05$ and ** indicates $p < 0.01$ relative to 0 hour MF. # indicates $p < 0.05$ relative to NF filter.

and enhanced mechanical activation. We note that transcriptional changes did take place in MF between the initial time point and after 24 hour culture (Fig. 5.11), including increases in CXCL1 and CXCL5. Thus, mechanical shear further enhanced these mediators. We also observed an increase in CCL2 and CC7 expression after culture, but these genes appeared to be mechanically insensitive.

Mechanical processing of SVF may also stimulate epithelial growth and matrix remodeling. HBEGF has been shown to accelerate re-epithelization in cutaneous wounds.[186,187] HBEGF expression increased for each mechanical processing condition after 24 hour culture, but only ED/FD was significant. Moreover, the MMP family is known to play a pivotal role in re-epithelialization in both acute and chronic wounds.[188,189] MMPs 1, 2, and 9 were all upregulated, with 1 and 9 substantially higher for ED/FD and DD than NF. Both HBEGF and MMP1 were elevated prior to culture (Figs. 5.9C and D), again indicating that cell enrichment was involved, but mechanical activation likely played a role as well, as has been observed for both MMP1[190] and HBEGF.[191] We also observed that MMP1 increased in MF between the initial time point and after 24 hour culture Fig. 5.11), which indicates that mechanical shear enhanced these responses. MM2 and MMP9 decreased in MF with time, which was counter-acted by mechanical processing.

We believe that the strongest and most straightforward effect of mechanical processing under shear stress was to promote angiogenesis. Most genes already discussed have been shown to increase cell recruitment, proliferation, tube formation, and induction of pro-angiogenic factors. This includes MMPs 1,[192] 2,[188,193] and 9,[188,193] as well as the inflammatory mediators CXCL1 and CXCL2,[194,195] CSF3,[196] IL-1β,[197], PTGS2,[198,199] Additionally, FGF2 and PDGFA expression increased for all mechanical treatments, and strongly promote angiogenesis through increased cell recruitment and proliferation.[200] We found that PDGFA was elevated prior to culture (Fig. 5.9C). Both FGF2[167] and PDGFA[166] secretion have been shown to increase with mechanical fluid shear, specifically in ADSCs for PDGFA. We did observe a decrease in the angiogenic factor, HGF, but only for the ED/FD condition. The enhanced expression of these pro-angiogenic mediators and enrichment of

the EPC sub-population measured by flow cytometry (Figs. 5.3, 5.5-5.6), taken together, suggest that mechanically processed lipoaspirate may enhance neovascularization of wounds.

5.3 Material and Methods

5.3.1 Emulsification Device Fabrication

Devices were 3D printed by Dinsmore Inc. (Irvine, CA) using an SLA 3D printer. Devices were printed using biocompatible Somos BioClear resin from Royal DSM(Elgin, Illinois). Expansion and constriction regions, as well as the luer inlet and outlet ports were printed as a single part.

5.3.2 Emulsification Device Operation

Lipoaspirate (LA) was obtained from the abdomen and flanks of patients using standard vacuum-assisted liposuction. LA was combined with sterile phosphate-buffered saline (PBS) and washed repeatedly until golden in color. 10 mL of washed LA was loaded into a syringe and connected to the luer inlet of the emulsification device. A collection syringe was connected to the luer outlet of the device. LA was passed back and forth through the device 10, 20, or 30 times using a syringe pump set to 20 mL/s. Samples were then prepared for SVF isolation, cell counts, and flow cytometry staining and analysis.

5.3.3. Stromal Vascular Fraction Isolation

All samples were processed for SVF isolation following a method previously described in literature.[153] Briefly, 0.1% type I collagenase (Sigma-Aldrich Co., St. Louis, MO) was prepared in PBS, sterilized using a 0.22 μm vacuum filter (Millipore Corp., Billerica, MA), mixed with LA at a 1:1 ratio, and incubated at 37°C for 30 min in a hot water bath, swirling intermittently. Control media (DMEM supplemented with 10% fetal bovine serum, 500 IU

penicillin and 500 μg streptomycin) was then added in an equal volume to neutralize enzymatic activity. Mixture was allowed to separate for 10 minutes, and the infranatant layer that contains the SVF was collected and filtered through a 100 μm cell strainer. Samples were centrifuged at 500 x g for 7 min and pellets were resuspended in control media.

5.3.4 Analysis of Single Cells using Flow Cytometry

Collagenase digested cell suspensions were evenly divided into FACS tubes and resuspended in FACS Buffer (1× PBS, without Ca and Mg cations) supplemented with 1% BSA (PBS+). Cell suspensions were stained simultaneously with 5 μL (1 test) of each of the following monoclonal mouse anti-human antibodies in 100 uL total volume: CD34-BV421 (clone 561), CD45-BV510 (clone 2D1), SSEA-3-FITC (clone MC-631), CD26-PE (clone BA5b), CD31-PE/Cy7 (clone WM59), CD55-APC (clone JS11), CD13-APC/Cy7 (clone WM15) for 20 minutes at 4°C and washed once with FACS Buffer by centrifugation. All antibodies were purchased from BioLegend, San Diego, CA. Cells were then resuspended in PBS+ supplemented with 7-AAD (BD Biosciences, San Jose, CA) and maintained on ice for at least 15 minutes prior to analysis on a Novocyte 3000 Flow Cytometer (ACEA Biosciences, San Diego, CA). Compensation was determined using single antibody stained samples of compensation beads (Invitrogen, Waltham, MA) and a live and dead (heat-killed at 55°C for 15 min) cell sample stained with 7-AAD. Gates encompassing the positive and negative subpopulations within each compensation sample were inputted into FlowJo to automatically calculate the compensation matrix. Compensated data was then analyzed using FlowJo software (FlowJo, Ashland, OR). Signal positivity was determined using appropriate Fluorescence Minus One (FMO) controls. A sequential gating scheme (Fig. 5.4)

was used to identify cell populations of interest from non-cellular debris and cellular aggregates.

5.3.5 Lipoaspirate Filter Device Fabrication

Filter devices were fabricated by ALine, Inc. (Rancho Dominguez, CA), as previously described.[97] Briefly, fluidic channels, openings for membranes, luers, and hosebarbs, and vias were micro-machined into acrylic layers using a CO_2 laser. Nylon mesh membranes with 500 and 1000 μm pore sizes were purchased from Amazon Small Parts (Seattle, WA) as large sheets and were cut to appropriate size using a CO_2 laser. Device layers, nylon mesh membranes, luers, and hose barbs were then assembled, bonded using adhesive, and pressure laminated to form a single monolithic device.

5.3.6 Lipoaspirate Filter Device Operation

Prior to introduction to the lipoaspirate (LA) filter devices, LA was processed using the Emulsification device for 30 passes, as previously described. A syringe loaded with this processed sample was then connected to the luer inlet of the filter device. Sample was passed through the device using a syringe pump at 10 mL/min, comparable to the flowrate used in earlier microfluidic filtration device studies.[97] LA filter devices were operated under direct filtration with the cross-flow outlet closed, in order to maximize sample recovery and processing speed. For device operation, the cross-flow outlet was closed off using a stop cock, and sample passed from the device inlet, through the membrane, and exited the effluent outlet. Filtered samples were collected from the effluent outlet, and prepared for SVF isolation, cell counts and flow cytometry staining and analysis

5.3.7 Dissociation Device Fabrication and Operation

Devices were 3D printed by 3D Systems (Rock Hill, SC), using their biocompatible Accura ClearVue resin. The branching network of channels in this device, as well as the luer inlet and outlet ports were printed as a single part. Channel height was constant at 750 μm throughout the branching network of channels. With each channel bifurcation, the minimum channel width halved, from 3 mm to 1.5 mm to 750 μm. For dissociation device testing, LA samples will be mechanically processed using 30 passes through the emulsification device passes and then filtered using the 1000 μm pore LA filter device. Sample effluent from the LA filter device was then be further processed using 100, 300, or 900 mL/min flow rates and 20 passes. Samples were collected and analyzed for cell counts, viability, stem/progenitor cell content, and population size using image analysis.

5.3.8 Transcriptional analysis via RT-qPCR

SVR was processed using MF, NF filtered, ED30+FD1000 (ED/FG), or ED30+FD1000+DD 900mL/min (DD) conditions and RNA was extracted immediately (0 hr) or after 24 hours in culture (24 hr). To separate tissue from lipids, blood, and local anesthetic, all samples were centrifuged (300xg, 3 min), and tissue was taken from the middle, fatty tissue layer either for immediate (0 hour) RNA extraction or for culture. Culture involved combining processed samples with media (DMEM+1% P/S) at a 1:1 ratio, plating in a petri dish, and incubating at 37°C and 5% CO2 to allow time for transcriptional changes to take place. To separate tissue from culture media after 24 hours, cultured samples were centrifuged (300xg, 3 min), and tissue was taken from the fatty tissue layer for RNA extraction. TRIzol reagent (Invitrogen, Carlsbad, CA, USA) was then added at a 1:1 ratio in Lysing Matrix D tubes with ceramic beads (MP Biomedicals, Irvine, CA, USA). A FastPrep-24

instrument (MP Biomedicals, Irvine, CA, USA) was then used to homogenize the sample for 40 seconds at 6 m/s. Samples were then snap frozen in liquid nitrogen. For analysis, samples were thawed on ice and TRIzol/tissue was transferred to a clean Eppendorf tube. Samples were centrifuged at 12,000 x g for 15 min and at 4°C. The red organic layer was transferred to another clean Eppendorf tube, 200 µL chloroform was added, and the tube was repeatedly inverted. The sample was then centrifuged at 12,000 x g for 15 min and at 4°C. The aqueous supernatant was transferred to a clean tube, chilled isopropanol was added at a 1:1 ratio, and the tube will be repeatedly inverted and vortexed. The sample was stored at -80°C for 30 min to precipitate, thawed on ice, centrifuged at 12000 x g for 15 min, and the supernatant was discarded. Next, 1 mL of 75% EtOH was added, the sample was vortexed and centrifuged again at 12000 x g for 15 min, and supernatant was discarded. EtOH wash steps were repeated a second time. On the final wash, all EtOH was removed from the tube and the sample was air dried for 10 min. RNA was then resuspended in RNase-free water and purified using a RNeasy mini kit with on-column DNase digestion (Qiagen, Germantown, MD, USA). RNA quality and concentration was assessed based on 260/280 and 260/230 absorbance ratios using a NanoDrop ND-1000 (Thermo Fisher, Waltham, MA, USA). RNA integrity number (RIN) was also assessed using an Agilent 2100 Bioanalyzer instrument (Agilent Technologies, Santa Clara, CA, USA). Extracted RNA was reverse transcribed into cDNA using a RT2 First Strand kit (Qiagen, Germantown, MD, USA) and analyzed using qPCR with a human wound healing RT2 Profiler PCR Array (Qiagen, Germantown, MD, USA) on a Mx3005P qPCR system (Agilent Technologies, Santa Clara, CA, USA) following manufacturer instructions. Gene expression results for each sample were normalized to expression of the reference gene RPLP0. Fold change in gene expression was then calculated for NF, ED/FD,

and DD conditions relative to MF at the same time point. Additionally, MF was normalized between the 0 and 24 hour time points.

5.4 Conclusion

In this work, we presented an integrated fluidic device platform that mechanically processes human lipoaspirate into an injectable therapeutic. This platform produces predictable and consistent shear forces to standardize lipoaspirate processing and will also enable automation in a clinical setting. First, we developed an emulsification device to replace the inter-syringe method used to produce nanofat, and SVF generated by this device matched or exceeded nanofat in terms of total cell numbers, cell viability, and key stem and progenitor cell populations. Next, we adapted our microfluidic filtration device by increasing filter membrane pore size and surface area in order to accommodate clinically-relevant volumes of emulsified lipoaspirate. We found that device filtering better maintains total cell numbers and stem/progenitor populations better than manually filtering nanofat through a standard mesh cloth. We then adapted our microfluidic dissociation device technology to further shear tissue aggregates. Total cell recovery was not significantly affected by processing with the dissociation device, but CD34+ cell and EPCs were enriched in a dose-dependent manner. Finally, we quantified relative gene expression of wound healing-related targets by real-time quantitative polymerase chain reaction (RT-qPCR) to investigate the effects of mechanical processing with our devices. We found that mechanical processing of lipoaspirate significantly activated several transcriptional programs linked to improved wound healing and that our new fluidic device platform elicited responses that were at least comparable to nanofat. Promisingly, for gene expression of pro-angiogenic mediators, device processing often elicited responses substantially stronger than seen in nanofat. It remains to

be seen whether this translates to similar wound healing dynamics and quality *in vivo*, which will be tested in using various models in future work. We will also seek to assess gene transcription changes at single cell resolution to delineate the extent to which our results can be correlated to differential enrichment of cell subtypes and induction of new transcriptional programs via mechanical activation. Finally, we will investigate cell responses over longer periods of time, both *in vitro* and *in vivo,* to monitor the transition from inflammation to healing and assess indictors of matrix remodeling and angiogenesis.

CHAPTER 6: Summary and Future Directions

Tissues are composed of highly heterogeneous mixtures of cell populations that vary significantly in terms of gene expression and function. Interrogating this cellular heterogeneity is proving crucial for understanding tissue and organ development, normal function, and disease pathogenesis. To achieve this, high-throughput single-cell analysis methods must be employed, but these efforts are greatly limited by the need to first break down tissues into single cell suspensions. Conventional tissue dissociation protocols are inefficient, time-consuming, manual intensive, and produce highly variable results. However, advances in microfabricated technologies hold exciting potential in their ability to carry out standard laboratory procedures, such as tissue dissociation, on-chip by offering high throughput, precise sample manipulation.

In Chapter 2, we presented a simple and inexpensive microfluidic device that filters large tissue fragments and dissociates smaller aggregates into single cells. The device produced cell suspensions with improved single cell yields and purity compared to conventional dissociation methods. The device incorporated two nylon mesh membranes with well-defined, micron-sized pores that operate on aggregates of different size scales. Using cancer cell lines, we demonstrated that aggregates were effectively dissociated using high flow rates and pore sizes that were smaller than a single cell. However, pore sizes that were less than half the cell size caused significant damage. We then improved results by passing the sample through two filter devices in series, with single cell yield and purity predominantly determined by the pore size of the second membrane. Next, we optimized performance using minced and digested murine kidney tissue samples, and determined that the combination of 50 and 15 μm membranes was optimal. Finally, we integrated these two

membranes into a single filter device and performed validation experiments using minced and digested murine kidney, liver, and mammary tumor tissue samples. The dual membrane microfluidic filter device increased single cell numbers by at least 3-fold for each tissue type, and in some cases by more than 10-fold. These results were obtained in minutes without affecting cell viability, and additional filtering would not be required prior to downstream applications. In Chapter 3, this dual membrane microfluidic filter device was integrated with additional upstream tissue processing technologies to create a complete tissue processing platform.

In Chapter 3, we presented a microfluidic platform consisting of 3 tissue processing technologies that rapidly process minced tissue specimens into single cell suspensions. First, we developed a novel microfluidic device for digesting minced tissue specimens. This device is easily loaded with mm-scale tissue and quickly breaks it down into smaller aggregates and even single cells. Next, we incorporated downstream dissociation and filtration technologies into a single, integrated microfluidic chip. After microfluidic digestion, tissue samples were processed with this integrated device to further enhance single cell yields and obviate the need for off-chip cell straining prior to single cell analysis. For kidney and tumor tissue processing, we found that 15 min using the platform processing produced similar single cell yields compared to a standard 1-hour manual dissociation protocol. Single cell RNA sequencing of kidney and tumor samples revealed that cellular stress responses are similar between device-processed and standard protocols, and can even be reduced in some instances. We also found that more difficult to dissociate cell types like endothelial cells are preferentially liberated with longer processing. We introduced a novel platform operation method, termed interval operation, where dissociated sample is periodically removed, and

yet-digested tissue continues to be processed. For liver and heart tissues, processing time could be reduced to 5 min, and even as short as 1 minute. Interestingly, recovery of the sample under interval operation produced substantially more hepatocytes and cardiomyocytes, most likely by preventing over processing. All results were achieved without compromising cell viability or requiring cell straining prior to single cell analyses. In future work, we will explore processing other tissue types, with a focus on human tissues for clinical applications, and also envision incorporating cell sorting and single cell analysis capabilities on-chip, to facilitate point-of-care single cell diagnostics.

In Chapter 4, we demonstrated that our microfluidic digestion device dissociates splenocyte populations from minced spleen specimens more effectively than traditional dissociation methods. We showed that the device can be operated under high flow rates to improve splenocyte recovery without adversely affecting cell viability. When operated under nonenzymatic conditions, the device matched or exceeded splenocyte cell yields of a commonly used strainer dissociation method. Under enzymatic conditions, splenocyte cell yields increased greatly and device operation produced results superior to a conventional enzymatic digestion protocol. Using an interval operation scheme, we showed that spleen samples could be easily sub-fractionated based on digestion time, with certain leukocyte populations preferentially dissociated when longer collagenase digestions are utilized. As a result, this device could be employed to crudely select certain splenocyte populations over others. Finally, we developed an operational protocol employing both nonenzymatic and enzymatic device intervals. Device processing with this protocol yielded higher numbers of all leukocyte populations investigated, again without compromising cell viability. In future work, we will explore dissociating other lymphoid tissues, such as the thymus and lymph

nodes, on-chip, and also seek to integrate downstream technologies to enable on-chip immune cell sorting and single cell analysis.

Chapter 5, we adapted our microfluidic tissue processing technologies to standardize and improve mechanical processing of human lipoaspirate for autologous therapeutics. First, we developed an emulsification device to replace the inter-syringe method used to produce nanofat. Both nanofat and device processing reduced total cell numbers by ~half compared to unprocessed macrofat, likely due to destruction of adipocyte and other mature cell populations. With the emulsification device, key stem and progenitor populations were concentrated by 2- to 4-fold relative to macrofat, with results matching or exceeding those seen in nanofat. Next, we adapted our microfluidic filtration device technology to remove large pieces of tissue in lipoaspirate. Design changes included increasing both filter membrane surface area and pore sizes to accommodate large volumes of emulsified lipoaspirate. A filter device pore size of 1 mm was found to be optimal for maintaining overall cell counts and stem/progenitor cell populations, and demonstrated results exceeding those produced by nanofat manually filtered through a 1 mm mesh cloth. We then adapted our microfluidic dissociation device to further break down tissue aggregates remaining after the filtration device. 3D printing was utilized to fabricate devices in order to withstand processing with high flow rates. The dissociation device minimally affected total cell recover but enriched CD34+ and EPCs in a flow rate dependent manner. Finally, we investigated the effect of mechanical processing of lipoaspirate on the expression of wound healing-related genes by real-time quantitative polymerase chain reaction. We collected samples immediately after processing to serve as a baseline, as well as after being cultured for 24 hours to allow for transcriptional changes to occur. Transcriptional changes were generally

modest immediately after processing. At 24 hours, many genes linked to improved wound healing and angiogenesis were significantly upregulated in mechanically processed samples, with the fluidic device platform eliciting responses that generally matched or exceeded nanofat. The most highly upregulated genes have been previously shown to increase in gene expression or secretion due to mechanical fluid shear, suggesting a possible mechanotransduction mechanism. In future work, we will further investigate transcriptional changes in device-processed lipoaspirate samples at greater resolution using single cell RNA sequencing to delineate the extent to which our results can be correlated to differential enrichment of cell subtypes and induction of new transcriptional programs via mechanical activation. We will also explore therapeutic effects of device-processing using *in vitro* angiogenesis models and animal models for wound healing.

REFERENCES

1. Bendall, S. C. & Nolan, G. P. From single cells to deep phenotypes in cancer. *Nat. Biotechnol.* **30**, 639–647 (2012).
2. Burrell, R. A., McGranahan, N., Bartek, J. & Swanton, C. The causes and consequences of genetic heterogeneity in cancer evolution. *Nature* **501**, 338–345 (2013).
3. Hanahan, D. & Weinberg, R. A. Hallmarks of cancer: The next generation. *Cell* (2011) doi:10.1016/j.cell.2011.02.013.
4. Rozenblatt-Rosen, O., Stubbington, M. J. T., Regev, A. & Teichmann, S. A. The Human Cell Atlas: From vision to reality. *Nature* (2017) doi:10.1038/550451a.
5. Tirosh, I. *et al.* Dissecting the multicellular ecosystem of metastatic melanoma by single-cell RNA-seq. *Science (80-.).* **352**, 189–196 (2016).
6. Regev, A. *et al.* The human cell atlas. *Elife* (2017) doi:10.7554/eLife.27041.
7. Gawad, C., Koh, W. & Quake, S. R. Single-cell genome sequencing: Current state of the science. *Nature Reviews Genetics* (2016) doi:10.1038/nrg.2015.16.
8. Kolodziejczyk, A. A., Kim, J. K., Svensson, V., Marioni, J. C. & Teichmann, S. A. The Technology and Biology of Single-Cell RNA Sequencing. *Mol. Cell* **58**, 610–620 (2015).
9. Stubbington, M. J. T., Rozenblatt-Rosen, O., Regev, A. & Teichmann, S. A. Single-cell transcriptomics to explore the immune system in health and disease. *Science (80-.).* **358**, 58–63 (2017).
10. Chattopadhyay, P. K., Winters, A. F., Lomas III, W. E., Laino, A. S. & Woods, D. M. High-Parameter Single-Cell Analysis. *Annu. Rev. Anal. Chem.* **12**, annurev-anchem-061417-125927 (2019).
11. Spitzer, M. H. & Nolan, G. P. Mass Cytometry: Single Cells, Many Features. *Cell* (2016) doi:10.1016/j.cell.2016.04.019.
12. Mistry, A. M., Greenplate, A. R., Ihrie, R. A. & Irish, J. M. Beyond the message: advantages of snapshot proteomics with single-cell mass cytometry in solid tumors. *FEBS Journal* (2019) doi:10.1111/febs.14730.

13. Papalexi, E. & Satija, R. Single-cell RNA sequencing to explore immune cell heterogeneity. *Nat. Rev. Immunol.* **18**, 35–45 (2018).

14. Villani, A.-C. *et al.* Single-cell RNA-seq reveals new types of human blood dendritic cells, monocytes, and progenitors. *Science (80-.).* **356**, eaah4573 (2017).

15. Nguyen, Q. H., Pervolarakis, N., Nee, K. & Kessenbrock, K. Experimental Considerations for Single-Cell RNA Sequencing Approaches. *Front. Cell Dev. Biol.* **6**, 1–7 (2018).

16. Autengruber, A., Gereke, M., Hansen, G., Hennig, C. & Bruder, D. Impact of enzymatic tissue disintegration on the level of surface molecule expression and immune cell function. *Eur. J. Microbiol. Immunol.* (2012) doi:10.1556/EuJMI.2.2012.2.3.

17. Adam, M., Potter, A. S. & Potter, S. S. Psychrophilic proteases dramatically reduce single cell RNA-seq artifacts: A molecular atlas of kidney development. *Development* **1**, dev.151142 (2017).

18. Zuk, P. A. *et al.* Multilineage Cells from Human Adipose Tissue: Implications for Cell-Based Therapies. *Tissue Eng.* (2001) doi:10.1089/107632701300062859.

19. Atalay, S., Coruh, A. & Deniz, K. Stromal vascular fraction improves deep partial thickness burn wound healing. *Burns* (2014) doi:10.1016/j.burns.2014.01.023.

20. Lee, H. C. *et al.* Safety and Effect of Adipose Tissue-Derived Stem Cell Implantation in Patients With Critical Limb Ischemia. *Circ. J.* (2012) doi:10.1253/circj.CJ-11-1135.

21. Cianfarani, F. *et al.* Diabetes impairs adipose tissue-derived stem cell function and efficiency in promoting wound healing. *Wound Repair Regen.* **21**, 545–553 (2013).

22. Nguyen, A. *et al.* Stromal vascular fraction: A regenerative reality? Part 1: Current concepts and review of the literature. *J. Plast. Reconstr. Aesthetic Surg.* **69**, 170–179 (2016).

23. Guo, J. *et al.* Stromal vascular fraction: A regenerative reality? Part 2: Mechanisms of regenerative action. *J. Plast. Reconstr. Aesthetic Surg.* **69**, 180–188 (2016).

24. Rehman, J. *et al.* Secretion of Angiogenic and Antiapoptotic Factors by

Human Adipose Stromal Cells. *Circulation* **109**, 1292–1298 (2004).

25. Wang, M. Human progenitor cells from bone marrow or adipose tissue produce VEGF, HGF, and IGF-I in response to TNF by a p38 MAPK-dependent mechanism. *AJP Regul. Integr. Comp. Physiol.* **291**, R880–R884 (2006).

26. Ebrahimian, T. G. *et al.* Cell therapy based on adipose tissue-derived stromal cells promotes physiological and pathological wound healing. *Arterioscler. Thromb. Vasc. Biol.* **29**, 503–510 (2009).

27. U.S. Food and Drug Administration, CFR - Code of Federal Regulations Title 21, Part 1271: Human Cells, Tissues, and Cellular and Tissue-Based Products. https://www.accessdata.fda.gov/scripts/cdrh/cfdocs/cfcfr/CFRSearch.cfm.

28. Banyard, D. A., Salibian, A. A., Widgerow, A. D. & Evans, G. R. D. Implications for human adipose-derived stem cells in plastic surgery. *J. Cell. Mol. Med.* **19**, 21–30 (2015).

29. Tonnard, P. *et al.* Nanofat grafting: Basic research and clinical applications. *Plast. Reconstr. Surg.* **132**, 1017–1026 (2013).

30. Yu, Q. *et al.* Co-Transplantation of Nanofat Enhances Neovascularization and Fat Graft Survival in Nude Mice. *Aesthetic Surg. J.* (2018) doi:10.1093/asj/sjx211.

31. Banyard, D. A. *et al.* Phenotypic analysis of stromal vascular fraction after mechanical shear reveals stress-induced progenitor populations. in *Plastic and Reconstructive Surgery* (2016). doi:10.1097/PRS.0000000000002356.

32. Whitesides, G. M. The origins and the future of microfluidics. *Nature* (2006) doi:10.1038/nature05058.

33. Wyatt Shields Iv, C., Reyes, C. D. & López, G. P. Microfluidic cell sorting: A review of the advances in the separation of cells from debulking to rare cell isolation. *Lab on a Chip* (2015) doi:10.1039/c4lc01246a.

34. Hattersley, S. M., Dyer, C. E., Greenman, J. & Haswell, S. J. Development of a microfluidic device for the maintenance and interrogation of viable tissue biopsies. *Lab Chip* **8**, 1842–1846 (2008).

35. Wallman, L. *et al.* Biogrid-a microfluidic device for large-scale enzyme-

free dissociation of stem cell aggregates. *Lab Chip* **11**, 3241–3248 (2011).

36. Lin, C. H., Lee, D. C., Chang, H. C., Chiu, I. M. & Hsu, C. H. Single-cell enzyme-free dissociation of neurospheres using a microfluidic chip. *Anal. Chem.* **85**, 11920–11928 (2013).

37. Qiu, X. *et al.* Microfluidic device for rapid digestion of tissues into cellular suspensions. *Lab Chip* **17**, 3300–3309 (2017).

38. Qiu, X., De Jesus, J., Pennell, M., Troiani, M. & Haun, J. B. Microfluidic device for mechanical dissociation of cancer cell aggregates into single cells. *Lab Chip* (2015) doi:10.1039/C4LC01126K.

39. Qiu, X. *et al.* Microfluidic channel optimization to improve hydrodynamic dissociation of cell aggregates and tissue. *Nat. Sci. Reports* **8**, 2774 (2018).

40. Li, X. J., Ling, V. & Li, P. C. H. Same-single-cell analysis for the study of drug efflux modulation of multidrug resistant cells using a microfluidic chip. *Anal. Chem.* (2008) doi:10.1021/ac800231k.

41. Li, X., Chen, Y. & Li, P. C. H. A simple and fast microfluidic approach of same-single-cell analysis (SASCA) for the study of multidrug resistance modulation in cancer cells. *Lab Chip* (2011) doi:10.1039/c0lc00626b.

42. Patel, A. P. *et al.* Single-cell RNA-seq highlights intratumoral heterogeneity in primary glioblastoma. *Science (80-.).* (2014) doi:10.1126/science.1254257.

43. Lawson, D. A. *et al.* Single-cell analysis reveals a stem-cell program in human metastatic breast cancer cells. *Nature* (2015) doi:10.1038/nature15260.

44. Li, H. *et al.* Reference component analysis of single-cell transcriptomes elucidates cellular heterogeneity in human colorectal tumors. *Nat. Genet.* (2017) doi:10.1038/ng.3818.

45. Venteicher, A. S. *et al.* Decoupling genetics, lineages, and microenvironment in IDH-mutant gliomas by single-cell RNA-seq. *Science (80-.).* (2017) doi:10.1126/science.aai8478.

46. Krebs, M. G. *et al.* Analysis of circulating tumor cells in patients with non-small cell lung cancer using epithelial marker-dependent and -independent approaches. *J. Thorac. Oncol.* **7**, 306–315 (2012).

47. Coumans, F. A. W., van Dalum, G., Beck, M. & Terstappen, L. W. M. M. Filtration Parameters Influencing Circulating Tumor Cell Enrichment from Whole Blood. *PLoS One* **8**, (2013).

48. Vona, G. *et al.* Isolation by Size of Epithelial Tumor Cells. *Am. J. Pathol.* (2000) doi:10.1016/S0002-9440(10)64706-2.

49. Zheng, S. *et al.* Membrane microfilter device for selective capture, electrolysis and genomic analysis of human circulating tumor cells. *J. Chromatogr. A* **1162**, 154–161 (2007).

50. Didar, T. F., Li, K., Veres, T. & Tabrizian, M. Separation of rare oligodendrocyte progenitor cells from brain using a high-throughput multilayer thermoplastic-based microfluidic device. *Biomaterials* **34**, 5588–5593 (2013).

51. Zhou, M. Da *et al.* Separable bilayer microfiltration device for viable label-free enrichment of circulating tumour cells. *Sci. Rep.* **4**, 1–11 (2014).

52. Fan, X. *et al.* A microfluidic chip integrated with a high-density PDMS-based microfiltration membrane for rapid isolation and detection of circulating tumor cells. *Biosens. Bioelectron.* **71**, 380–386 (2015).

53. Kang, Y. T., Doh, I., Byun, J., Chang, H. J. & Cho, Y. H. Label-free rapid viable enrichment of circulating tumor Cell by photosensitive polymer-based microfilter device. *Theranostics* **7**, 3179–3191 (2017).

54. Sarioglu, A. F. *et al.* A microfluidic device for label-free, physical capture of circulating tumor cell clusters. *Nat. Methods* **12**, 685–691 (2015).

55. Hou, J. M. *et al.* Clinical significance and molecular characteristics of circulating tumor cells and circulating tumor microemboli in patients with small-cell lung cancer. *J. Clin. Oncol.* **30**, 525–532 (2012).

56. Aceto, N. *et al.* Circulating tumor cell clusters are oligoclonal precursors of breast cancer metastasis. *Cell* (2014) doi:10.1016/j.cell.2014.07.013.

57. Kim, M. Y., Li, D. J., Pham, L. K., Wong, B. G. & Hui, E. E. Microfabrication of high-resolution porous membranes for cell culture. *J. Memb. Sci.* (2014) doi:10.1016/j.memsci.2013.11.034.

58. Palakkan, A. A., Hay, D. C., Pr, A. K., Tv, K. & Ross, J. A. Liver tissue engineering and cell sources: Issues and challenges. *Liver International* (2013) doi:10.1111/liv.12134.

59. Paszek, M. J. & Weaver, V. M. The tension mounts: Mechanics meets morphogenesis and malignancy. *Journal of Mammary Gland Biology and Neoplasia* (2004) doi:10.1007/s10911-004-1404-x.

60. Liu, J. F., Yadavali, S., Tsourkas, A. & Issadore, D. Microfluidic diafiltration-on-chip using an integrated magnetic peristaltic micropump. *Lab Chip* (2017) doi:10.1039/c7lc00954b.

61. Altschuler, S. J. & Wu, L. F. Cellular Heterogeneity: Do Differences Make a Difference? *Cell* (2010) doi:10.1016/j.cell.2010.04.033.

62. Nguyen, Q. H. *et al.* Profiling human breast epithelial cells using single cell RNA sequencing identifies cell diversity. *Nat. Commun.* (2018) doi:10.1038/s41467-018-04334-1.

63. Park, J. *et al.* Single-cell transcriptomics of the mouse kidney reveals potential cellular targets of kidney disease. *Science (80-.).* **763**, eaar2131 (2018).

64. MacParland, S. A. *et al.* Single cell RNA sequencing of human liver reveals distinct intrahepatic macrophage populations. *Nat. Commun.* (2018) doi:10.1038/s41467-018-06318-7.

65. Gladka, M. M. *et al.* Single-Cell Sequencing of the Healthy and Diseased Heart Reveals Cytoskeleton-Associated Protein 4 as a New Modulator of Fibroblasts Activation. *Circulation* (2018) doi:10.1161/CIRCULATIONAHA.117.030742.

66. Reyfman, P. A. *et al.* Single-cell transcriptomic analysis of human lung provides insights into the pathobiology of pulmonary fibrosis. *Am. J. Respir. Crit. Care Med.* (2019) doi:10.1164/rccm.201712-2410OC.

67. Zeisel, A. *et al.* Cell types in the mouse cortex and hippocampus revealed by single-cell RNA-seq. *Science (80-.).* (2015) doi:10.1126/science.aaa1934.

68. Muraro, M. J. *et al.* A Single-Cell Transcriptome Atlas of the Human Pancreas. *Cell Syst.* (2016) doi:10.1016/j.cels.2016.09.002.

69. Hinohara, K. & Polyak, K. Intratumoral Heterogeneity: More Than Just Mutations. *Trends in Cell Biology* (2019) doi:10.1016/j.tcb.2019.03.003.

70. Karaayvaz, M. *et al.* Unravelling subclonal heterogeneity and aggressive disease states in TNBC through single-cell RNA-seq. *Nat. Commun.* (2018) doi:10.1038/s41467-018-06052-0.

71. Wang, Y. & Navin, N. E. Advances and Applications of Single-Cell Sequencing Technologies. *Molecular Cell* (2015) doi:10.1016/j.molcel.2015.05.005.

72. Shekhar, K. *et al.* Comprehensive Classification of Retinal Bipolar Neurons by Single-Cell Transcriptomics. *Cell* (2016) doi:10.1016/j.cell.2016.07.054.

73. Treutlein, B. *et al.* Reconstructing lineage hierarchies of the distal lung epithelium using single-cell RNA-seq. *Nature* (2014) doi:10.1038/nature13173.

74. Beckwitt, C. H. *et al.* Liver 'organ on a chip'. *Experimental Cell Research* (2018) doi:10.1016/j.yexcr.2017.12.023.

75. Howard, D., Buttery, L. D., Shakesheff, K. M. & Roberts, S. J. Tissue engineering: Strategies, stem cells and scaffolds. *Journal of Anatomy* (2008) doi:10.1111/j.1469-7580.2008.00878.x.

76. Murphy, M. B., Moncivais, K. & Caplan, A. I. Mesenchymal stem cells: Environmentally responsive therapeutics for regenerative medicine. *Experimental and Molecular Medicine* (2013) doi:10.1038/emm.2013.94.

77. Mahla, R. S. Stem cells applications in regenerative medicine and disease therapeutics. *International Journal of Cell Biology* (2016) doi:10.1155/2016/6940283.

78. Low, L. A. & Tagle, D. A. Tissue chips-innovative tools for drug development and disease modeling. *Lab on a Chip* (2017) doi:10.1039/c7lc00462a.

79. Esch, E. W., Bahinski, A. & Huh, D. Organs-on-chips at the frontiers of drug discovery. *Nature Reviews Drug Discovery* (2015) doi:10.1038/nrd4539.

80. Aref, A. R. *et al.* 3D microfluidic: Ex vivo culture of organotypic tumor spheroids to model immune checkpoint blockade. *Lab Chip* (2018) doi:10.1039/c8lc00322j.

81. Portillo-Lara, R. & Annabi, N. Microengineered cancer-on-a-chip platforms to study the metastatic microenvironment. *Lab Chip* (2016) doi:10.1039/c6lc00718j.

82. Ribas, J. *et al.* Cardiovascular Organ-on-a-Chip Platforms for Drug Discovery and Development. *Appl. Vitr. Toxicol.* (2016)

doi:10.1089/aivt.2016.0002.

83. Smalley, I. *et al.* Leveraging transcriptional dynamics to improve BRAF inhibitor responses in melanoma. *EBioMedicine* (2019) doi:10.1016/j.ebiom.2019.09.023.

84. Wu, H., Kirita, Y., Donnelly, E. L. & Humphreys, B. D. Advantages of Single-Nucleus over Single-Cell RNA Sequencing of Adult Kidney: Rare Cell Types and Novel Cell States Revealed in Fibrosis. *J. Am. Soc. Nephrol.* ASN.2018090912 (2018) doi:10.1681/ASN.2018090912.

85. Sonna, L. A., Fujita, J., Gaffin, S. L. & Lilly, C. M. Invited review: Effects of heat and cold stress on mammalian gene expression. *Journal of Applied Physiology* (2002) doi:10.1152/japplphysiol.01143.2001.

86. O'Donnell, A., Odrowaz, Z. & Sharrocks, A. D. Immediate-early gene activation by the MAPK pathways: What do and don't we know? *Biochemical Society Transactions* (2012) doi:10.1042/BST20110636.

87. O'Flanagan, C. H. *et al.* Dissociation of solid tumor tissues with cold active protease for single-cell RNA-seq minimizes conserved collagenase-associated stress responses. *Genome Biol.* (2019) doi:10.1186/s13059-019-1830-0.

88. Van Den Brink, S. C. *et al.* Single-cell sequencing reveals dissociation-induced gene expression in tissue subpopulations. *Nature Methods* (2017) doi:10.1038/nmeth.4437.

89. Contreras-Naranjo, J. C., Wu, H. J. & Ugaz, V. M. Microfluidics for exosome isolation and analysis: Enabling liquid biopsy for personalized medicine. *Lab on a Chip* (2017) doi:10.1039/c7lc00592j.

90. Mashaghi, S., Abbaspourrad, A., Weitz, D. A. & van Oijen, A. M. Droplet microfluidics: A tool for biology, chemistry and nanotechnology. *TrAC - Trends in Analytical Chemistry* (2016) doi:10.1016/j.trac.2016.05.019.

91. Duncombe, T. A., Tentori, A. M. & Herr, A. E. Microfluidics: Reframing biological enquiry. *Nature Reviews Molecular Cell Biology* (2015) doi:10.1038/nrm4041.

92. El-Ali, J., Sorger, P. K. & Jensen, K. F. Cells on chips. *Nature* (2006) doi:10.1038/nature05063.

93. Yeo, L. Y., Chang, H. C., Chan, P. P. Y. & Friend, J. R. Microfluidic devices for bioapplications. *Small* (2011) doi:10.1002/smll.201000946.

94. Shen, Y., Yalikun, Y. & Tanaka, Y. Recent advances in microfluidic cell sorting systems. *Sensors and Actuators, B: Chemical* (2019) doi:10.1016/j.snb.2018.11.025.

95. Lenshof, A. & Laurell, T. Continuous separation of cells and particles in microfluidic systems. *Chem. Soc. Rev.* (2010) doi:10.1039/b915999c.

96. Gossett, D. R. *et al.* Label-free cell separation and sorting in microfluidic systems. *Analytical and Bioanalytical Chemistry* (2010) doi:10.1007/s00216-010-3721-9.

97. Qiu, X. *et al.* Microfluidic filter device with nylon mesh membranes efficiently dissociates cell aggregates and digested tissue into single cells. *Lab Chip* **18**, 2776–2786 (2018).

98. Wu, H. & Humphreys, B. D. The promise of single-cell RNA sequencing for kidney disease investigation. *Kidney International* (2017) doi:10.1016/j.kint.2017.06.033.

99. Liao, J. *et al.* Single-cell RNA sequencing of human kidney. *Sci. Data* (2020) doi:10.1038/s41597-019-0351-8.

100. Schaum, N. *et al.* Single-cell transcriptomics of 20 mouse organs creates a Tabula Muris. *Nature* (2018) doi:10.1038/s41586-018-0590-4.

101. Pisco, A. O. *et al.* A Single Cell Transcriptomic Atlas Characterizes Aging Tissues in the Mouse. *bioRxiv* (2019) doi:https://doi.org/10.1101/661728.

102. Han, X. *et al.* Mapping the Mouse Cell Atlas by Microwell-Seq. *Cell* (2018) doi:10.1016/j.cell.2018.02.001.

103. Seligson, D. B. *et al.* Epithelial Cell Adhesion Molecule (KSA) Expression: Pathobiology and Its Role As An Independent Predictor of Survival in Renal Cell Carcinoma. *Clin. Cancer Res.* (2004) doi:10.1158/1078-0432.CCR-1132-03.

104. Denisenko, E. *et al.* Systematic assessment of tissue dissociation and storage biases in single-cell and single-nucleus RNA-seq workflows. *Genome Biol.* (2020) doi:10.1186/s13059-020-02048-6.

105. Chung, W. *et al.* Single-cell RNA-seq enables comprehensive tumour and immune cell profiling in primary breast cancer. *Nat. Commun.* **8**, 1–12 (2017).

106. Haque, A., Engel, J., Teichmann, S. A. & Lönnberg, T. A practical guide to single-cell RNA-sequencing for biomedical research and clinical applications. *Genome Med.* **9**, 1–12 (2017).

107. Insua-Rodríguez, J. *et al.* Stress signaling in breast cancer cells induces matrix components that promote chemoresistant metastasis. *EMBO Mol. Med.* **10**, 1–21 (2018).

108. Ramsdale, R. *et al.* The transcription cofactor c-JUN mediates phenotype switching and BRAF inhibitor resistance in melanoma. *Sci. Signal.* **8**, ra82 (2015).

109. Fan, F. *et al.* The AP-1 transcription factor JunB is essential for multiple myeloma cell proliferation and drug resistance in the bone marrow microenvironment. *Leukemia* (2017) doi:10.1038/leu.2016.358.

110. Brown, G. E. & Khetani, S. R. Microfabrication of liver and heart tissues for drug development. *Philos. Trans. R. Soc. B Biol. Sci.* **373**, (2018).

111. Zhang, B. & Radisic, M. Organ-on-A-chip devices advance to market. *Lab on a Chip* (2017) doi:10.1039/c6lc01554a.

112. Van Den Berg, A., Mummery, C. L., Passier, R. & Van der Meer, A. D. Personalised organs-on-chips: functional testing for precision medicine. *Lab Chip* (2019) doi:10.1039/c8lc00827b.

113. Poisson, J. *et al.* Liver sinusoidal endothelial cells: Physiology and role in liver diseases. *Journal of Hepatology* (2017) doi:10.1016/j.jhep.2016.07.009.

114. Brown, G. E. & Khetani, S. R. Microfabrication of liver and heart tissues for drug development. *Philosophical Transactions of the Royal Society B: Biological Sciences* (2018) doi:10.1098/rstb.2017.0225.

115. Underhill, G. H. & Khetani, S. R. Advances in engineered human liver platforms for drug metabolism studies. *Drug Metab. Dispos.* **46**, 1626–1637 (2018).

116. Ware, B. R., Durham, M. J., Monckton, C. P. & Khetani, S. R. A Cell Culture Platform to Maintain Long-term Phenotype of Primary Human Hepatocytes and Endothelial Cells. *CMGH* (2018) doi:10.1016/j.jcmgh.2017.11.007.

117. Li, F., Cao, L., Parikh, S. & Zuo, R. Three-Dimensional Spheroids With Primary Human Liver Cells and Differential Roles of Kupffer Cells in

Drug-Induced Liver Injury. *J. Pharm. Sci.* (2020) doi:10.1016/j.xphs.2020.02.021.

118. Agarwal, A., Goss, J. A., Cho, A., McCain, M. L. & Parker, K. K. Microfluidic heart on a chip for higher throughput pharmacological studies. *Lab Chip* **13**, 3599–3608 (2013).

119. Conant, G. *et al.* High-Content Assessment of Cardiac Function Using Heart-on-a-Chip Devices as Drug Screening Model. *Stem Cell Rev. Reports* **13**, 335–346 (2017).

120. Ackers-Johnson, M. *et al.* A Simplified, Langendorff-Free Method for Concomitant Isolation of Viable Cardiac Myocytes and Nonmyocytes from the Adult Mouse Heart. *Circ. Res.* (2016) doi:10.1161/CIRCRESAHA.116.309202.

121. Judd, J., Lovas, J. & Huang, G. N. Isolation, culture and transduction of adult mouse cardiomyocytes. *J. Vis. Exp.* (2016) doi:10.3791/54012.

122. Ackers-Johnson, M., Tan, W. L. W. & Foo, R. S. Y. Following hearts, one cell at a time: recent applications of single-cell RNA sequencing to the understanding of heart disease. *Nature Communications* (2018) doi:10.1038/s41467-018-06894-8.

123. Ilicic, T. *et al.* Classification of low quality cells from single-cell RNA-seq data. *Genome Biol.* (2016) doi:10.1186/s13059-016-0888-1.

124. Macosko, E. Z. *et al.* Highly parallel genome-wide expression profiling of individual cells using nanoliter droplets. *Cell* **161**, 1202–1214 (2015).

125. Karaiskos, N. *et al.* A single-cell transcriptome atlas of the mouse glomerulus. *J. Am. Soc. Nephrol.* (2018) doi:10.1681/ASN.2018030238.

126. Bronte, V. & Pittet, M. J. The spleen in local and systemic regulation of immunity. *Immunity* (2013) doi:10.1016/j.immuni.2013.10.010.

127. Mebius, R. E. & Kraal, G. Structure and function of the spleen. *Nat. Rev. Immunol.* **5**, 606–616 (2005).

128. Jaitin, D. A. *et al.* Massively Parallel Single-Cell RNA-Seq for Marker-Free Decomposition of Tissues into Cell Types. *Science (80-.).* **343**, 776–779 (2014).

129. Chen, H., Ye, F. & Guo, G. Revolutionizing immunology with single-cell RNA sequencing. *Cell. Mol. Immunol.* **16**, 242–249 (2019).

130. Inaba, K. *et al.* Isolation of dendritic cells. *Current Protocols in Immunology* (2009) doi:10.1002/0471142735.im0307s86.

131. Fujiyama, S. *et al.* Identification and isolation of splenic tissue-resident macrophage sub-populations by flow cytometry. *Int. Immunol.* (2018) doi:10.1093/intimm/dxy064.

132. Steinman, R. M. & Cohn, Z. A. Identification of a novel cell type in peripheral lymphoid organs of mice: I. Morphology, quantitation, tissue distribution. *J. Exp. Med.* (1973) doi:10.1084/jem.137.5.1142.

133. Inaba, K. *et al.* Granulocytes, macrophages, and dendritic cells arise from a common major histocompatibility complex class II-negative progenitor in mouse bone marrow. *Proc. Natl. Acad. Sci. U. S. A.* **90**, 3038–3042 (1993).

134. Metlay, J. P. *et al.* The distinct leukocyte integrins of mouse spleen dendritic cells as identified with new hamster monoclonal antibodies. *J. Exp. Med.* (1990) doi:10.1084/jem.171.5.1753.

135. Merad, M., Sathe, P., Helft, J., Miller, J. & Mortha, A. The Dendritic Cell Lineage: Ontogeny and Function of Dendritic Cells and Their Subsets in the Steady State and the Inflamed Setting. *Annu. Rev. Immunol.* (2013) doi:10.1146/annurev-immunol-020711-074950.

136. Steinman, R. M., Kaplan, G., Witmer, M. D. & Cohn, Z. A. Identification of a novel cell type in peripheral lymphoid organs of mice: V. Purification of spleen dendritic cells, new surface markers, and maintenance in vitro*. *J. Exp. Med.* (1979) doi:10.1084/jem.149.1.1.

137. Austyn, J. M. & Gordon, S. F4/80, a monoclonal antibody directed specifically against the mouse macrophage. *Eur. J. Immunol.* **11**, 805–815 (1981).

138. Lai, L., Alaverdi, N., Maltais, L. & Morse, H. C. Mouse cell surface antigens: nomenclature and immunophenotyping. *J. Immunol.* **160**, 3861–8 (1998).

139. Pinchuk, L. M. & Filipov, N. M. Differential effects of age on circulating and splenic leukocyte populations in C57BL/6 and BALB/c male mice. *Immun. Ageing* **5**, 1–12 (2008).

140. Hensel, J. A., Khattar, V., Ashton, R. & Ponnazhagan, S. Characterization of immune cell subtypes in three commonly used mouse strains reveals

gender and strain-specific variations. *Lab. Investig.* **99**, 93–106 (2019).

141. Pittet, M. J. & Weissleder, R. Intravital imaging. *Cell* (2011) doi:10.1016/j.cell.2011.11.004.

142. Colovai, A. I. *et al.* Flow cytometric analysis of normal and reactive spleen. *Mod. Pathol.* (2004) doi:10.1038/modpathol.3800141.

143. Gimble, J. M., Katz, A. J. & Bunnell, B. A. Adipose Derived Stem Cells for Regenerative Medicine. *Circ Res* **100**, 12491260 (2007).

144. Bunnell, B. A., Flaat, M., Gagliardi, C., Patel, B. & Ripoll, C. Adipose-derived stem cells: Isolation, expansion and differentiation. *Methods* (2008) doi:10.1016/j.ymeth.2008.03.006.

145. Godoy Zanicotti, D., Coates, D. E. & Duncan, W. J. In vivo bone regeneration on titanium devices using serum-free grown adipose-derived stem cells, in a sheep femur model. *Clin. Oral Implants Res.* (2017) doi:10.1111/clr.12761.

146. Latief, N. *et al.* Adipose stem cells differentiated chondrocytes regenerate damaged cartilage in rat model of osteoarthritis. *Cell Biol. Int.* (2016) doi:10.1002/cbin.10596.

147. Valina, C. *et al.* Intracoronary administration of autologous adipose tissue-derived stem cells improves left ventricular function, perfusion, and remodelling after acute myocardial infarction. *Eur. Heart J.* (2007) doi:10.1093/eurheartj/ehm426.

148. Frese, L., Dijkman, P. E. & Hoerstrup, S. P. Adipose Tissue-Derived Stem Cells in Regenerative Medicine. *Transfus. Med. Hemotherapy* **43**, 268–274 (2016).

149. Garimella, M. G. *et al.* Adipose-Derived Mesenchymal Stem Cells Prevent Systemic Bone Loss in Collagen-Induced Arthritis. *J. Immunol.* (2015) doi:10.4049/jimmunol.1500332.

150. Lee, W. Y. *et al.* Autologous adipose tissue-derived stem cells treatment demonstrated favorable and sustainable therapeutic effect for crohn's fistula. *Stem Cells* (2013) doi:10.1002/stem.1357.

151. Semon, J. A. *et al.* Administration of Murine Stromal Vascular Fraction Ameliorates Chronic Experimental Autoimmune Encephalomyelitis. *Stem Cells Transl. Med.* (2013) doi:10.5966/sctm.2013-0032.

152. Han, S., Kim, H. & Kim, W. The treatment of diabetic foot ulcers with uncultured, processed lipoaspirate cells: a pilot study. *Wound Repair Regen.* (2010) doi:10.1111/j.1524-475X.2010.00593.x.

153. Banyard, D. A., Salibian, A. A., Widgerow, A. D. & Evans, G. R. D. Implications for human adipose-derived stem cells in plastic surgery. *J. Cell. Mol. Med.* (2015) doi:10.1111/jcmm.12425.

154. Uyulmaz, S., Sanchez Macedo, N., Rezaeian, F., Giovanoli, P. & Lindenblatt, N. Nanofat Grafting for Scar Treatment and Skin Quality Improvement. *Aesthetic Surg. J.* (2018) doi:10.1093/asj/sjx183.

155. Heneidi, S. *et al.* Awakened by Cellular Stress: Isolation and Characterization of a Novel Population of Pluripotent Stem Cells Derived from Human Adipose Tissue. *PLoS One* **8**, (2013).

156. Ogura, F. *et al.* Human Adipose Tissue Possesses a Unique Population of Pluripotent Stem Cells with Nontumorigenic and Low Telomerase Activities: Potential Implications in Regenerative Medicine. *Stem Cells Dev.* **23**, 717–728 (2014).

157. Kinoshita, K. *et al.* Therapeutic Potential of Adipose-Derived SSEA-3-Positive Muse Cells for Treating Diabetic Skin Ulcers. *Stem Cells Transl. Med.* **4**, 146–155 (2015).

158. Aronowitz, J. A., Lockhart, R. A. & Hakakian, C. S. Mechanical versus enzymatic isolation of stromal vascular fraction cells from adipose tissue. *Springerplus* **4**, 1–9 (2015).

159. Tremolada, C., Colombo, V. & Ventura, C. Adipose Tissue and Mesenchymal Stem Cells: State of the Art and Lipogems® Technology Development. *Current Stem Cell Reports* (2016) doi:10.1007/s40778-016-0053-5.

160. Ansorge, H. *et al.* Autologous fat processing via the revolve system: Quality and quantity of fat retention evaluated in an animal model. *Aesthetic Surg. J.* (2014) doi:10.1177/1090820X14524416.

161. Zhu, M. *et al.* Comparison of three different fat graft preparation methods: Gravity separation, centrifugation, and simultaneous washing with filtration in a closed system. *Plast. Reconstr. Surg.* (2013) doi:10.1097/PRS.0b013e31828276e9.

162. Oberbauer, E. *et al.* Enzymatic and non-enzymatic isolation systems for

adipose tissue-derived cells: Current state of the art. *Cell Regen.* **4**, 4:7 (2015).

163. Rennert, R. C. *et al.* Microfluidic single-cell transcriptional analysis rationally identifies novel surface marker profiles to enhance cell-based therapies. *Nat. Commun.* **7**, 1–9 (2016).

164. Glossop, J. R. & Cartmell, S. H. Effect of fluid flow-induced shear stress on human mesenchymal stem cells: Differential gene expression of IL1B and MAP3K8 in MAPK signaling. *Gene Expr. Patterns* (2009) doi:10.1016/j.gep.2009.01.001.

165. Russell-Puleri, S. *et al.* Fluid shear stress induces upregulation of COX-2 and PGI2 release in endothelial cells via a pathway involving PECAM-1, PI3K, FAK, and p38. *Am. J. Physiol. - Hear. Circ. Physiol.* (2017) doi:10.1152/ajpheart.00035.2016.

166. Bravo, B. *et al.* Opposite Effects of Mechanical Action of Fluid Flow on Proangiogenic Factor Secretion From Human Adipose-Derived Stem Cells With and Without Oxidative Stress. *J. Cell. Physiol.* (2017) doi:10.1002/jcp.25712.

167. Hennig, T., Mogensen, C., Kirsch, J., Pohl, U. & Gloe, T. Shear stress induces the release of an endothelial elastase: Role in integrin α vβ 3-mediated FGF-2 release. *J. Vasc. Res.* (2011) doi:10.1159/000327009.

168. Zheng, L. *et al.* Fluid shear stress regulates metalloproteinase-1 and 2 in human periodontal ligament cells: Involvement of extracellular signal-regulated kinase (ERK) and P38 signaling pathways. *J. Biomech.* (2012) doi:10.1016/j.jbiomech.2012.07.013.

169. Shaik, S. S. *et al.* Low intensity shear stress increases endothelial ELR+ CXC chemokine production via a focal adhesion kinase-p38β MAPK-NF-κB pathway. *J. Biol. Chem.* (2009) doi:10.1074/jbc.M807205200.

170. Sidney, L. E., Branch, M. J., Dunphy, S. E., Dua, H. S. & Hopkinson, A. Concise review: Evidence for CD34 as a common marker for diverse progenitors. *Stem Cells* (2014) doi:10.1002/stem.1661.

171. Philips, B. J. *et al.* Prevalence of endogenous CD34+ adipose stem cells predicts human fat graft retention in a xenograft model. *Plast. Reconstr. Surg.* (2013) doi:10.1097/PRS.0b013e31829fe5b1.

172. Chong, M. S. K., Ng, W. K. & Chan, J. K. Y. Concise Review: Endothelial

Progenitor Cells in Regenerative Medicine: Applications and Challenges. *Stem Cells Transl. Med.* (2016) doi:10.5966/sctm.2015-0227.

173. Jurgens, W. J. F. M. *et al.* Effect of tissue-harvesting site on yield of stem cells derived from adipose tissue: Implications for cell-based therapies. *Cell Tissue Res.* **332**, 415–426 (2008).

174. Brem, H. & Tomic-Canic, M. Cellular and molecular basis of wound healing in diabetes. *J. Clin. Invest.* (2007) doi:10.1172/jci32169.

175. Rennert, R. C. *et al.* Diabetes impairs the angiogenic potential of adipose-derived stem cells by selectively depleting cellular subpopulations. *Stem Cell Res. Ther.* (2014) doi:10.1186/scrt468.

176. Thomas, S. *et al.* Adipose Derived Stem Cells and Wound Healing in Patients with Diabetes : a Promising Therapeutic Modality. **2**, (2014).

177. Agha, R., Ogawa, R., Pietramaggiori, G. & Orgill, D. P. A review of the role of mechanical forces in cutaneous wound healing. *Journal of Surgical Research* (2011) doi:10.1016/j.jss.2011.07.007.

178. Najar, M. *et al.* Insights into inflammatory priming of mesenchymal stromal cells: functional biological impacts. *Inflammation Research* (2018) doi:10.1007/s00011-018-1131-1.

179. Noronha Nc, N. D. C. *et al.* Priming approaches to improve the efficacy of mesenchymal stromal cell-based therapies. *Stem Cell Research and Therapy* (2019) doi:10.1186/s13287-019-1224-y.

180. Redondo-Castro, E. *et al.* Interleukin-1 primes human mesenchymal stem cells towards an anti-inflammatory and pro-trophic phenotype in vitro. *Stem Cell Res. Ther.* (2017) doi:10.1186/s13287-017-0531-4.

181. Kouroupis, D., Sanjurjo-Rodriguez, C., Jones, E. & Correa, D. Mesenchymal Stem Cell Functionalization for Enhanced Therapeutic Applications. *Tissue Engineering - Part B: Reviews* (2019) doi:10.1089/ten.teb.2018.0118.

182. Bartosh, T. J. *et al.* Aggregation of human mesenchymal stromal cells (MSCs) into 3D spheroids enhances their antiinflammatory properties. *Proc. Natl. Acad. Sci. U. S. A.* (2010) doi:10.1073/pnas.1008117107.

183. Glossop, J. R., Hidalgo-Bastida, L. A. & Cartmell, S. H. Fluid shear stress induces differential gene expression of leukemia inhibitory factor in human mesenchymal stem cells. *J. Biomater. Tissue Eng.* (2011)

doi:10.1166/jbt.2011.1013.

184. Kosaki, K., Ando, J., Korenaga, R., Kurokawa, T. & Kamiya, A. Fluid shear stress increases the production of granulocyte-macrophage colony-stimulating factor by endothelial cells via mRNA stabilization. *Circ. Res.* (1998) doi:10.1161/01.RES.82.7.794.

185. Henn, D. *et al.* MicroRNA-regulated pathways of flow-stimulated angiogenesis and vascular remodeling in vivo. *J. Transl. Med.* (2019) doi:10.1186/s12967-019-1767-9.

186. Johnson, N. R. & Wang, Y. Controlled delivery of heparin-binding EGF-like growth factor yields fast and comprehensive wound healing. *J. Control. Release* (2013) doi:10.1016/j.jconrel.2012.11.004.

187. Shirakata, Y. *et al.* Heparin-binding EGF-like growth factor accelerates keratinocyte migration and skin wound healing. *J. Cell Sci.* (2005) doi:10.1242/jcs.02346.

188. Caley, M. P., Martins, V. L. C. & O'Toole, E. A. Metalloproteinases and Wound Healing. *Adv. Wound Care* (2015) doi:10.1089/wound.2014.0581.

189. Mazini, L., Rochette, L., Admou, B., Amal, S. & Malka, G. Hopes and limits of adipose-derived stem cells (ADSCs) and mesenchymal stem cells (MSCs) in wound healing. *International Journal of Molecular Sciences* (2020) doi:10.3390/ijms21041306.

190. Galie, P. A. *et al.* Fluid shear stress threshold regulates angiogenic sprouting. *Proc. Natl. Acad. Sci. U. S. A.* (2014) doi:10.1073/pnas.1310842111.

191. Morita, T. *et al.* Shear stress increases heparin-binding epidermal growth factor-like growth factor mrna levels in human vascular endothelial cells. *Biochem. Biophys. Res. Commun.* (1993) doi:10.1006/bbrc.1993.2469.

192. Blackburn, J. S. & Brinckerhoff, C. E. Matrix metalloproteinase-1 and thrombin differentially activate gene expression in endothelial cells via PAR-1 and promote angiogenesis. *Am. J. Pathol.* (2008) doi:10.2353/ajpath.2008.080512.

193. Rundhaug, J. E. Matrix metalloproteinases, angiogenesis, and cancer: Commentary re: A. C. Lockhart et al., Reduction of wound angiogenesis in patients treated with BMS-275291, a broad spectrum matrix

metalloproteinase inhibitor. Clin. Cancer Res., 9: 00-00, 2003. *Clinical Cancer Research* (2003).

194. Ridiandries, A., Tan, J. T. M. & Bursill, C. A. The role of chemokines in wound healing. *International Journal of Molecular Sciences* (2018) doi:10.3390/ijms19103217.

195. Mehrad, B., Keane, M. P. & Strieter, R. M. Chemokines as mediators of angiogenesis. *Thrombosis and Haemostasis* (2007) doi:10.1160/TH07-01-0040.

196. Lopes, L. *et al.* Stem cell therapy for diabetic foot ulcers: A review of preclinical and clinical research. *Stem Cell Research and Therapy* (2018) doi:10.1186/s13287-018-0938-6.

197. Fahey, E. & Doyle, S. L. IL-1 family cytokine regulation of vascular permeability and angiogenesis. *Frontiers in Immunology* (2019) doi:10.3389/fimmu.2019.01426.

198. Zhi, Y. H. *et al.* Cyclooxygenase-2 promotes angiogenesis by increasing vascular endothelial growth factor and predicts prognosis in gallbladder carcinoma. *World J. Gastroenterol.* (2005) doi:10.3748/wjg.v11.i24.3724.

199. Iñiguez, M. A., Rodríguez, A., Volpert, O. V., Fresno, M. & Redondo, J. M. Cyclooxygenase-2: A therapeutic target in angiogenesis. *Trends in Molecular Medicine* (2003) doi:10.1016/S1471-4914(02)00011-4.

200. Li, P. & Guo, X. A review: therapeutic potential of adipose-derived stem cells in cutaneous wound healing and regeneration. *Stem Cell Res. Ther.* (2018) doi:10.1186/s13287-018-1044-5.